4-11-2018

Nanostructured Materials Derived from Metal-Organic Frameworks for Energy and Environmental Applications

Zhiqiang Xie
Louisiana State University and Agricultural and Mechanical College

NANOSTRUCTURED MATERIALS DERIVED FROM METAL-ORGANIC FRAMEWORKS FOR ENERGY AND ENVIRONMENTAL APPLICATIONS

A Dissertation

Submitted to the Graduate Faculty of the
Louisiana State University and
Agricultural and Mechanical College
in partial fulfillment of the
requirements for the degree of
Doctor of Philosophy

in

The Department of Mechanical & Industrial Engineering

by
Zhiqiang Xie
B.S., Kunming University of Science and Technology, 2011
M.S., University of Dayton, 2013
May 2018

ACKNOWLEDGMENTS

I am grateful to my advisor, Prof. Ying Wang, whose consistent guidance, encouragement, advice and generous support made it possible for me to work on a research topic that was of great interest to me. It is a great opportunity for me to join her research group and work under her supervision and instruction. I also would like to sincerely thank Prof. Wenjin Meng, Prof. Dorel Moldovan and Prof. Leszek Czarnecki for being willing to serve on my doctoral committee.

I am very thankful to my collaborators, Dr. Jianqing Zhao at Soochow University in China; Hilary Eikhuemelo, Wangwang Xu, Xiaodan Cui and Sarah Ellis at Louisiana State University (LSU); Ziyang He at Iowa State University; Zheng Liu at Nanyang Technological University; Xuhui Feng, Prof. Moises A Carreon at Colorado School of Mines; Chengmin Jiang, Prof. Angel A. Martí at Rice University; Jiuhong Zhang at Kent State University; Dr. Yujie Zhang, Prof. Aiguo Wu at Ningbo Institute of Industrial Technology, Chinese Academy of Sciences.

I would like to acknowledge all the financial support from Research Enhancement Award (REA) and the Research Awards Program (RAP) sponsored by LaSPACE, Graduate Student Travel Award (LSU), LSU Economic Development Assistantship, ECS Travel Grant Award from the Battery Division in The Electrochemical Society

Last but not least, I really appreciate my parents, old brother and young sister in China for their great support and love. I also would like to sincerely thank all my friends at LSU for their support and understanding in dealing with the challenges I have faced.

TABLE OF CONTENTS

LIST OF FIGURES

ABSTRACT

Nowadays, energy and environmental issues have become the top priority among a series of global issues. Fossil fuels as the dominant source are depleted fast and usually lead to some environmental problems. Heavy metal pollution has posed a severe threat to environment and public health. Metal-organic frameworks (MOFs), as a very promising category of porous materials, have attracted more and more interest in research communities due to their extremely high surface areas, diverse nanostructures and unique properties. To meet the ever-increasing energy demand and tackle the heavy metal pollution in water, MOFs can function as ideal templates to prepare various nanostructured materials for energy and environmental cleaning applications. The aim of this dissertation is to design and synthesize metal-organic frameworks (MOFs) derived nanomaterials with desirable structures, morphologies and compositions for energy applications in Li-ion batteries (LIBs), dye-sensitized solar cells (DSSCs) and electrocatalytic water splitting and environmental application in removal of heavy metal from aqueous systems. Their performances are mainly dependent on the characteristics of nanostructured materials. Briefly, the first two projects are focused on synthesis of ZIF-8 derived N-doped porous carbon and ZIF-67 derived ultrafine Co_3O_4 nanoparticles/carbon nanotube composites as high-performance anode materials for Li-ion batteries. The third project concentrates on synthesis of CoNi alloy embedded carbon nanocages derived from bimetallic organic frameworks for DSSCs. In addition, MOFs-derived CoNi and CoN_x@Co/N-doped carbon tubes are synthesized and evaluated as low-cost electrocatalysts for efficient oxygen evolution reaction (OER). The last project is focused on study of ZIF-8 as an efficient absorbent for removal of copper ions from wastewater.

CHAPTER 1. INTRODUCTION

1.1 Current Energy and Environmental Issues

Energy and environmental issues have become the top priority among a series of global issues for the next 50 years. Nowadays, fossil fuels are the dominant source to satisfy the energy needs of humanity, however, these resources are depleted fast and usually lead to some environmental problems, such as air pollution and global warming owing to the emissions of nitrous oxide, methane, carbon dioxide and other gases containing volatile organic compounds [1,2]. Furthermore, the ever-increasing market of electrical vehicles and various portable electronics motivates the development of high-energy and high-power energy storage devices as new power sources [3-5]. In this regard, great efforts have been made to overcome the above-mentioned challenges by developing new energy storage and conversion technologies, including rechargeable Li-ion batteries (LIBs), dye-sensitized solar cells (DSSCs), fuel cells, and so forth.

With the rapid increase of industrial and human activities, dwindling freshwater caused by severe pollution from industrial wastewater is considered as one of the most critical global environmental issues. In particular, heavy metal pollution has posed a severe threat to environment and public health since heavy metals are not biodegradable and prone to accumulate in the environment. In addition, most of heavy metal ions even with low concentrations are dangerous and extremely toxic to human health. For example, high concentration of Cu^{2+} in public drinking water systems will result in serious diseases such as cramps, diarrhea, gastrointestinal catarrh and damage of liver and kidney [2]. According to Environmental Protection Agency (EPA) guidelines and World Health Organization (WHO), the permissible limits of Cu^{2+} for drinking water quality is 1.3 and 2.0 mg L^{-1}, respectively. Therefore, it is crucial to develop suitable methods to efficiently remove trace-level heavy metal ions from aqueous systems.

1.1.1 Rechargeable Li-ion Batteries (LIBs)*

LIBs have become popular power supplies not only for various portable electronic devices, but also for EVs, due to their unique advantages such as high energy and high power density, environmental benignity, long lifetime, as well as no memory effects [6, 7]. Metallic lithium was initially used as anode for LIBs, owing to its very high theoretical capacity of ~ 3840 mAh g^{-1} and low reduction potential [8]. However, the growth of dendrites during the repeated charge/discharge processes will lead to a short circuit within the LIBs, thereby resulting in some safety issues. As such, graphite replaced metallic lithium as anode for commercial LIBs, thanks to its low cost and better safety, although it possesses a much lower capacity of 372 mAh g^{-1} [9]. The graphite anode can store charges via an insertion mechanism, in which lithium ions are reversibly inserted into graphite. Nevertheless, practical capacity and cycle life of graphite anode are usually compromised due to an unavoidable blockage of insertion sites in the graphite. Figure 1.1 shows the schematic illustration of a rechargeable lithium ion battery [10]. As we can see that there are three main components in a lithium ion battery cell: cathode, anode and electrolyte. The cathode and anode are separated by an electronic insulator but Li^{+} conducting electrolyte. When the battery is powering an electronic, it undergoes the discharging process, in which the lithium

* Reprinted with permission from Zhiqiang Xie, Wangwang Xu, Xiaodan Cui, and Ying Wang, Recent progress in metal-organic frameworks and their derived nanostructures for energy and environmental applications" ChemSusChem, 2017, 10, 1645-1663.

ions are extracted out of the anode material (graphite) and inserted into the cathode material (cathode) and vice versa in the charging process. The energy density and power density of a lithium ion battery are mainly dependent on electrochemical properties of electrode materials [11, 12].

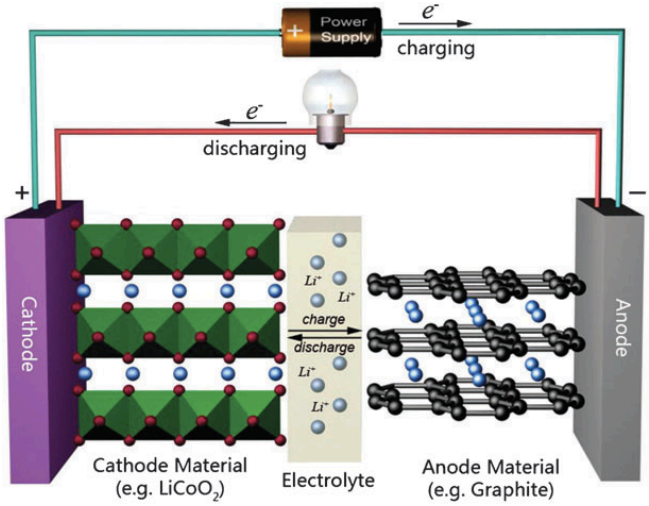

Figure 1.1 Schematic illustration of the working principal of a lithium-ion battery [10].

Generally speaking, the electrode materials should possess the following characteristics to achieve the goal of high-energy and high-power lithium ion batteries: (*i*) a high theoretical capacity; (*ii*) an excellent electrical conductivity, which can ensure the fast charge transport within the electrodes and thus can enhance the rate capability of a lithium ion battery; (*iii*) a superior structural stability during repeated charge/discharge processes, which plays a key in role in cycling performance; (*iv*) highly reversible electrochemical reactions at electrodes, which can maintain the specific capacity for long-term charge/discharge cycles; (*v*) a high cell voltage, which is determined by the standard redox potential of the cathode and anode during the respective electrode redox reactions.

Unfortunately, synthesis processes of these electrode materials usually require multi-step, complicated procedures and/or very expensive equipment, which are not practical for potential commercialization in industry. Furthermore, the current electrode materials of lithium ion batteries still cannot satisfy all the above-mentioned requirements and thus suffer from unsatisfactory cycling stability and intrinsically poor rate capability [13-18]. Thus, it is highly desirable to develop low-cost synthesis strategies to fabricate high-performance electrode materials with a high specific capacity, superior rate capability and excellent cycling stability over hundreds or even thousands of charge/discharge cycles.

1.1.2 Dye-Sensitized Solar Cells (DSSCs)

To fulfill the increasing energy demands, the exploration of renewable and sustainable energy sources is becoming more and more urgent. Among various forms of energy, solar energy stands out as an ideal candidate owing to its unlimited supply and clean nature. As a leading technology in the third-generation solar cells, DSSCs have received tremendous interest owing to their easy-fabrication, ecological-green and low-cost nature [2, 19]. As shown in Figure 1.2, a typical DSSC is composed of three main parts: a dye-sensitized photoanode, a liquid electrolyte and a counter electrode [20]. When sunlight passes through the transparent electrode, the photosensitizers accept incident photon and electrons are excited to flow into the photoanode. Then electrons are collected and transferred to the counter electrode via external circuit. Meanwhile, photosensitizer is regenerated by oxidizing

the electrolyte ions, which are reduced back by accepting electrons from the counter electrode.

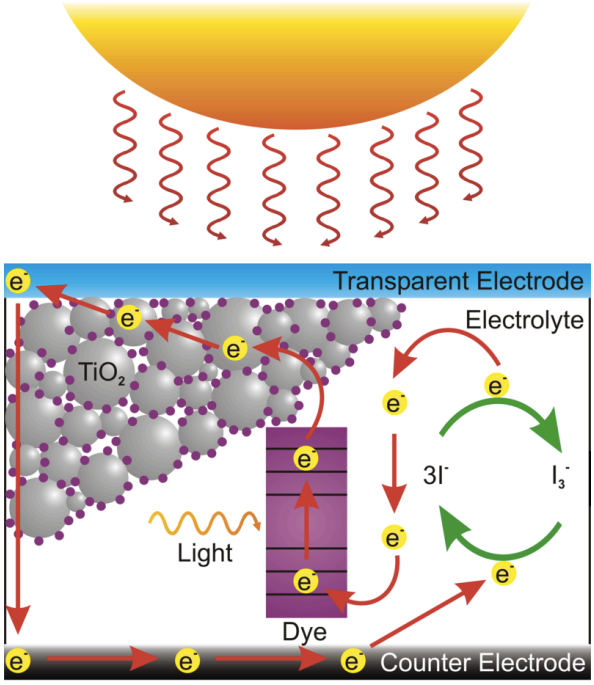

Figure 1.2 Schematic illustrating working principal of DSSCs [20].

In DSSCs, the photoanode is both skeleton matrix for dye adsorption and photocatalyst for charge generation and transportation, which makes it the most critical component of DSSCs. Therefore, the surface area to volume ratio, the optical property and electronic property determine the ultimate performance of a photoanode. Among various semiconductors, TiO_2 receives the most attention due to its high conduction band edge and good dye loading affinity. Nowadays, other metal oxides start attracting researchers' attention, especially ZnO, also a wide bandgap semiconductor but with a much higher electron mobility. Recently, more and more efforts are devoted to developing nanostructured TiO_2 and ZnO with different morphologies such as nanoparticles, nanosheets, nanotubes and hybrid nanostructures [21, 22].

The functions of counter electrode in a DSSC include catalyzing redox couples in the electrolyte at the electrode/electrolyte interface, accepting from the external circuit and conducting electrons to the electrolyte. Therefore, a functional counter electrode must possess an excellent electrocatalyst activity toward electrolyte redox couples (typically, I_3^-/I^-) and high electrical conductivity. In addition, a good chemical stability, eco-friendly nature and low-cost are also crucial for an ideal counter electrode. Platinum (Pt) coated on transparent conductive substrate is the traditional counter electrode for DSSCs. At current stage, exploration of affordable, durable and efficient counter electrode material is a crucial task for DSSC development.

1.1.3 Electrocatalytic Water Splitting

Hydrogen has attracted wide attention as en efficient energy storage carrier thanks to its abundant and sustainable nature [23, 24]. In the present, electrocatalytic water splitting is considered as the most efficient ways to produce high-purity hydrogen at low cost [25-27]. As shown in Figure 1.3, the splitting of water involves two half reactions of hydrogen

evolution reaction (HER) at cathode and oxygen evolution reaction (OER) at anode in acidic, alkaline or neutral solutions [28].

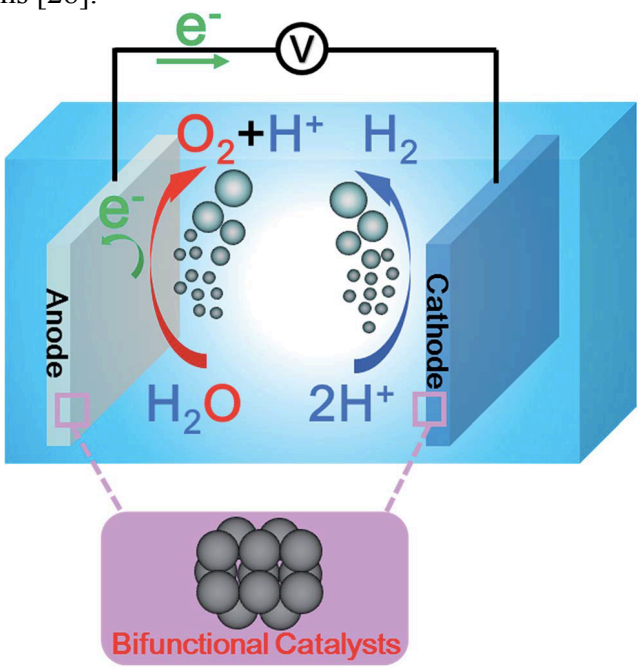

Figure 1.3 Schematic showing the working principal of electrocatalytic water splitting in acidic aqueous solution based on the oxygen evolution and hydrogen reactions by using bifunctional catalysts [28].

In acidic solution,

Cathode: $2H^+ + 2e^- \rightarrow H_2$ (1)

Anode: $H_2O \rightarrow 2H^+ + 1/2O_2 + 2e^-$ (2)

In alkaline or neutral solution,

Cathode: $2H_2O + 2e^- \rightarrow H_2 + 2OH^-$ (3)

Anode: $2OH^- \rightarrow H_2O + 1/2O_2 + 2e^-$ (4)

Total reaction: $H_2O \rightarrow H_2 + 1/2O_2$ (5)

The major challenge of water splitting is the sluggish kinetics of OER as compared to HER, which usually requires a large overpotential for multi-step transfer of four electrons. Up to date, noble metal oxides such as ruthenium oxides (RuO_2) and iridium oxides (IrO_2) are efficient electrocatalysts for OER. Nevertheless, their large-scale applications are severely hindered by the high cost and scarcity of the noble metals. In addition, these noble metal oxides exhibit poor chemical stability in alkaline solution. To date, various noble metal-free electrocatalysts such as transition metal oxides [29], hydroxides [30], nitrides [31], sulfides [32] and phosphides [33], have been widely reported. Unfortunately, most of these materials are either limited by their low electrical conductivities or poor electrocatalytic activities, resulting in much higher overpotential at a current density of 10 mA cm^{-2} compared to RuO_2 (410 mV) [33]. To overcome the aforementioned challenges, it is always desirable to explore new alternatives to replace noble metal oxides as low-cost and efficient electrocatalysts for OER.

1.1.4 Heavy Metal Removal for Wastewater Treatment

Heavy metals are metallic chemical elements that have a density larger than 5 g cm^{-3} [2]. Typically, heavy metals include arsenic (As), lead (Pb), mercury (Hg), aluminum (Al), iron (Fe), cadmium (Cd), cobalt (Co), copper (Cu), manganese (Mn), chromium (Cr), nickel (Ni), zinc (Zn), and etc. Some heavy metal ions such as Fe and Zn are essential nutrients for human health at very low concentrations. They function either as catalyzers in metalloprotein or as cofactor/activators of enzyme-involved reaction. These metal nutrients play pivotal roles in human physiology such as redox reactions, electron transfer, and nucleic acid metabolisms [2, 37]. Currently, heavy metal ion pollutions have become a serious environmental issue owing to the rapid development of modern industry. There are many types of heavy metal ion pollutions in industrial wastewaters from battery manufacturing, smelting, tanneries, metal plating, and so forth. The heavy metals are not biodegradable and tend to be accumulated in foods such as aquatic products, vegetables, and land animals. More importantly, heavy metals can be ingested in human body via food intake and thus cause various serious diseases. For example, excessive intake of copper can cause vomiting, convulsions and even death. Thus, it is extremely important to develop efficient methods for removal of the heavy metal pollutions in environments such as wastewater.

Up to date, various approaches, such as chemical precipitation, ion exchange, membrane filtration, and adsorption, have been reported for heavy metal wastewater treatment [2, 37]. Among them, adsorption has been considered as an economic and effective approach for heavy metal wastewater treatment benefiting from its flexibility and simplicity of design, low operation cost and good adsorption capability. Furthermore, adsorption is partially reversible, and thus adsorbents sometimes can be recovered by proper desorption process. Among the available adsorbents, activated carbon (AC) and carbon nanotubes (CNTs) have been widely reported as promising adsorbents in the removal of heavy metal ions [37]. However, the adsorption capacities of metal ions by AC and CNTs are very low and the whole adsorption process usually takes several hours or even longer. Furthermore, both AC and CNTs are expensive, which further hinders their practical applications in heavy metal wastewater treatment. Recently, various nanosized metal oxides (NMOs) [2, 37], such as nanosized Fe_3O_4, Fe_2O_3, TiO_2 and CeO_2, have be studied as promising alternatives for removal of heavy metal ions from aqueous systems owing to their high specific surface areas and high activities resulted from the so-called size-quantization effect. Nevertheless, NMOs tend to agglomerate owing to their high surface energy; thus adsorption capacity of NMOs would be significantly decreased. Therefore, it is highly challenging but extremely desirable to develop low-cost adsorbents with both high efficiency and high adsorption capacity for practical applications in removal of heavy metals from industrial wastewater.

1.2 Metal-Organic Frameworks and Their Derived Nanostructures

1.2.1 Pristine Metal-Organic Frameworks

Metal-organic frameworks (MOFs) are a family of intriguing porous solids with well-defined crystalline structures and extremely large surface area. They are generally synthesized through the coordination reaction between metal clusters/ions and proper organic ligands [34, 35]. The commonly used metal clusters/ions are transition metals and some lanthanides. The organic ligands function as bridges to link metal ions within the MOFs. The ligands containing pyridyl and cyano groups, crown ethers, polyamines, phosphonates, carboxylates are mostly chosen for preparation of MOFs under specific synthetic conditions [34, 35]. Thanks to a vast variety of primary building blocks, 20,000 different MOFs with controlled sizes, shapes and properties, have been reported so far. It is not surprising that primary building blocks (metal clusters/ions and organic ligands) of MOFs play a very

crucial role in determining their intrinsic physical-chemical properties and structural features. The shape and pore size of various MOFs are distinctly different from each other, owing to the use of diverse primary building blocks. However, it should be noted that the synthesis approaches and processing parameters must be taken into consideration as well.

MOFs can be facilely prepared using various synthesis methods such as solvothermal, microwave-assisted heating, electrochemical and mechanochemical methods [35]. Among them, conventional solvothermal synthesis of MOFs usually takes from a few hours to several days in a large reaction temperature range (80–250 °C). To produce MOFs more efficiently, new synthesis approaches have been developed in the past decade. For example, microwave-assisted synthesis can achieve rapid production of MOFs under hydrothermal conditions. The advantages of this synthetic approach include the decreased crystallization time, narrow particle size distribution, good morphology control, as well as high yields of MOFs. The first environmentally benign electrochemical synthesis of MOFs was reported for a large-scale production of a Cu-based MOF (HKUST-1) in 2005. Instead of using metal salts, this synthesis method utilizes metal ions supplied by anodic dissolution of a bulk metal plate. Mechanochemcial synthesis has also been developed for more efficient production of MOFs, and offers many advantages. For instance, mechanochemical reaction can occur without using any solvents. In addition, there are no specific requirements for temperature and pressure. Interestingly, in this approach metal ions are supplied by metal oxides instead of commonly used metal salts for obtaining MOFs. All the aforementioned synthesis techniques have been systematically studied over the years and show great potential in large-scale production of MOFs for industrial applications.

1.2.2 Metal-Organic Frameworks Derived Nanostructures

To, address the challenges in the field of energy storage and conversion, as shown in Figure 1.4, MOFs have been applied as ideal templates to prepare various nanostructured materials under specific gas atmospheres and proper temperatures in the past five years, including porous carbons, metal oxides, metal sulfides, metal oxides/carbon composites and so forth. For MOFs-derived carbons, nitrogen can be easily doped into the carbons via one-step pyrolysis of MOFs at high temperature, which would be beneficial for improving electrical conductivity and electrochemical activity of MOF-derived carbons. For MOF-derived metal oxides, they can be synthesized via one-step or two-step calcination in air. The obtained metal oxides can keep similar morphologies of MOFs through proper control of calcination temperature and heating/cooling rate. The hollow structures of MOF-derived metal oxides as electrode materials offer many benefits such as freedom of volume change, large surface area, as well as fast charge and mass transport. To improve their electrical conductivity and structural stability, carbon matrix can be incorporated with metal oxides to form metal oxide/carbon composites by carbonization of MOFs in inert gas, followed by calcination in air. The ultrafine metal oxide nanoparticles are well dispersed within the highly porous carbon matrix.

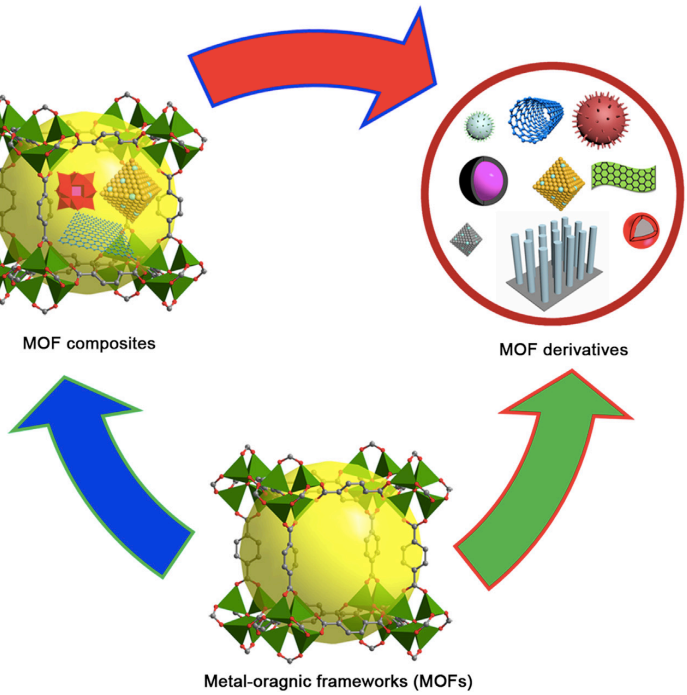

Figure 1.4 Schematics of MOFs, MOF composites and their derived nanostructures [36].

The MOF-derived nanostructures offer many unique advantages [2, 36]: (i) Their chemical compositions can be easily tuned by designing various MOFs combined with specific thermal treatment; (ii) MOF-derived nanostructures provide controlled porosity and huge surface area that facilitate easy access of electrolyte into the electrode and ensure large electrolyte/electrode contact area; (iii) The electron and ion diffusion lengths can be significantly shortened, which is very beneficial for rate performance of the MOF-derived nanostructured electrodes; (vi) The low-cost and easy synthesis of MOF-derived nanostructures allows for potential large scale production for eventual industrial applications.

1.3 Motivation and Goals

As one of the commercially available anode materials for LIBs, graphite is the most common one but still exhibits some drawbacks such as a low theoretical capacity of 372 mAh g^{-1} and distinctly poorer electrochemical performances at higher charge-discharge rates, which is far from satisfactory for meeting the needs of high-energy high-power LIBs. To date, many new carbonaceous anode materials with various nanostructures have been evaluated for lithium storage and demonstrated significantly improved performance compared to commercial graphite anodes, however, most carbonaceous materials have low electrical conductivity and poor structural stability when cycled at high charge/discharge rates as well as limited active sites for effective Li-ion storage. Therefore, it is highly desirable to develop new carbonaceous anode materials with excellent conductivity and better structural stability.

In addition to carbonaceous anodes, Co_3O_4 clearly stands out as a promising anode material for LIBs, thanks to its high theoretical capacity of 890 mAh g^{-1} and other attractive properties, such as highly reactive facets, great chemical/thermal stability as well as good safety during operation. Unfortunately, the fundamental problems of transition metal oxides such as huge volume changes, serious particle aggregation and low intrinsic electric conductivity, lead to severe pulverization of electrodes, thereby resulting in fast capacity decay upon prolonged cycling and inferior rate performance.

As a crucial component in DSSCs, the counter electrodes (CEs) play a key role in governing the power conversion efficiency (PCE) since they mainly transfer electrons from the external circuit and perform electrocatalytic reduction of the redox couples. Therefore, as

an ideal CE, it should possess promising characteristics, such as excellent electrical conductivity, high electrocatalytic activity and low cost. At present, platinum (Pt) has been widely employed as a high-performance CE for DSSCs since it could satisfy most of the above-mentioned characteristics. Nevertheless, Pt is highly expensive and extremely scarce, thereby severely impeding large-scale fabrication of DSSCs for practical commercialization. In addition, the DSSCs based on Pt as CE materials still show unsatisfactory long-term operation stability mainly due to the corrosive iodide/triiodide redox electrolyte. To overcome the aforementioned challenges, it is highly needed to explore new alternatives to replace Pt as efficient and low-cost CEs for DSSCs.

The oxygen evolution reaction (OER) plays a crucial role in electrocatalytic water splitting for production of hydrogen. Due to its sluggish kinetics and high activation overpotential, tremendous efforts have been made to search for highly efficient and robust electrocatalysts. Noble metals and their oxides (RuO_2, IrO_2) are the mostly used catalysts for OER due to their high catalytic activity and good durability. However, the scarcity and high cost impede their practical applications in the global energy system. Therefore, there is a pressing need to develop noble metal-free electrocatalysts with both desirable catalytic activities and reasonable cost for OER application.

Benefiting from MOF derived nanomaterials with controllable structures and desirable properties, my doctoral research projects are mainly focused on design and synthesis of new nanostructured materials by using various MOFs as precursors/templates to address the aforementioned challenges in different energy storage and conversion systems such as LIBs, DSSCs, electrocatalytic water splitting and heavy metal removal for wastewater treatment.

1.4 Outline of the Dissertation

This dissertation presents five research projects on synthesis of metal-organic frameworks derived nanomaterials with desirable structures, morphologies and compositions for applications.

Chapter 1 first introduces the working principals of Li-ion batteries, dye-sensitized solar cells and electrocatalytic water splitting, then discusses heavy metal pollution in water and current challenges that need to be addressed. Metal-organic frameworks and their derived nanostructures as promising energy materials are described as well.

In Chapter 2, the first section presents a synthesis approach to obtain sandwich-like, graphene-based porous nitrogen-doped carbons (PNCs@Gr) via pyrolysis of Zn-based zeolitic imidazolate framework (ZIF-8) nanocrystals grown on graphene oxide (GO) (ZIF-8@GO), for application as a high-performance anode material in LIBs. The second section introduces a robust controllable preparation of Co-based zeolitic imidazolate framework (ZIF-67) derived Co_3O_4 nanoparticles uniformly confined into a sheet-like SWCNT matrix as a LIB anode material, showing highly reversible lithium storage properties. The electrochemical performances of the as-prepared composite samples are evaluated and optimized by varying the loading amounts of Co_3O_4 in the composites.

Chapter 3 presents the synthesis of CoNi embedded carbon nanocages as a new counter electrode in DSSCs for the first time, by applying Co/Ni bimetallic metal organic framework (MOF) as the template. The DSSC efficiency can be maximized by simply optimizing the ratio of Ni^{2+}/Co^{2+} precursor concentration during the synthesis. The DSSC based on this new counter electrode exhibits optimal performance with an improved power conversion efficiency (PCE) compared to commercial Pt counter electrode.

In Chapter 4, the first section presents the application of MOF-derived CoNi embedded carbon nanocages as OER electrocatalysts for water splitting. Various electrochemical measurements are performed to evaluate their catalytic activity and

durability. The second section describes a simple and scalable synthesis of CoN_x@Co/N-doped carbon tubes hybrid as an efficient OER electrocatalyst. The resultant CoN_x@Co/NCT hybrid exhibits bamboo-like structure with high density of active sites originated from abundant CoN_x species, high nitrogen doping level and topological defects, rendering excellent electrocatalytic activities towards OER in alkaline medium.

Chapter 5 displays that water-stable ZIF-8 nanocrystals synthesized at room temperature are evaluated for highly efficient removal of copper ions from aqueous systems due to its high surface area and large porosity. The possible adsorption mechanism is explored for the first time using various characterization techniques, such as scanning electron microscopy (SEM), transmission electron microscopy (TEM), Fourier transform infrared spectroscopy (FTIR), X-ray photoelectron spectroscopy (XPS) and X-ray diffraction (XRD).

Chapter 6 provides a brief summary of my research findings in development of novel nanostructured materials derived from metal-organic frameworks for applications in lithium-ion batteries, dye-sensitized solar cells and electrocatalytic water splitting.

1.5 References

[1] M. Z. Jacobson, Review of solutions to global warming, air pollution, and energy security. Energy Environ. Sci. 2009, 2, 148-173.

[2] Z. Q. Xie, W. W. Xu, X. D. Cui, Y. Wang, Recent progress in metal–organic frameworks and their derived nanostructures for energy and environmental applications, ChemSusChem, 2017, 10, 1645-1663.

[3] Z. Q. Xie, Novel design and synthesis of nanostructured electrode materials for advanced lithium ion batteries" (2017). LSU Master's Theses. 4503.
https://digitalcommons.lsu.edu/gradschool_theses/4503

[4] V. Etacheri, R. Marom, R. Elazari, G. Salitra, D. Aurbach, Challenges in the development of advanced Li-ion batteries: a review. Energy Environ. Sci, 2011, 4, 3243-3262.

[5] T. H. Kim, J. S. Park, S. K. Chang, S. Choi, J. H. Ryu, H. K. Song, The current move of lithium ion batteries towards the next phase. Adv. Energy Mater, 2012, 2, 860-872.

[6] N. A. Kaskhedikar, J. Maier, Lithium storage in carbon nanostructures. Adv. Mater. 2009, 21, 2664-2680.

[7] S. Chu, A. Majumdar, Opportunities and challenges for a sustainable energy future. Nature, 2012, 488, 294−303.

[8] W. W. Xu, Z. Q. Xie, Z. Wang, G. Dietrich, Y. Wang, Interwoven heterostructural Co_3O_4–carbon@FeOOH hollow polyhedrons with improved electrochemical performance. J. Mater. Chem. A, 2016, 4, 19011-19018.

[9] N. Omar, M. Daowd, O. Hegazy, G. Mulder, J.M., Coosemans, T. Timmermans, P. Van den Bossche, J. Van Mierlo, Standardization work for BEV and HEV applications: critical appraisal of recent traction battery documents. Energies, 2012, 5, 138-156.

[10] R. Liu, J. Duay, S. B. Lee, Heterogeneous nanostructured electrode materials for electrochemical energy storage. Chem. Commun., 2011, 47, 1384–1404

[11] C. N. He, S. Wu, N. Q. Zhao, C. S. Shi, E. Z. Liu, J. J. Li, Carbon-encapsulated Fe_3O_4 nanoparticles as a high-rate lithium ion battery anode material. ACS Nano, 2013, 7, 4459-4469.

[12] M. Winter, J. O. Besenhard, Electrochemical lithiation of tin and tin-based intermetallics and composites. Electrochim. Acta, 1999, 45, 31-50.

[13] C. M. Julien, A. Mauger, K. Zaghib, H. Groult, Comparative issues of cathode materials for Li-ion batteries. Inorganics, 2014, 2, 132-154.

[14] A. C. Kozen, C. F. Lin, A. J. Pearse, M. A. Schroeder, X. G. Han, L. B. Hu, S. B. Lee, G. W. Rubloff, M. Noked, Next-generation lithium metal anode engineering via atomic layer deposition. ACS Nano, 2015, 9, 5884 -5892.

[15] Y. Wang, G. Z. Cao, Next-generation lithium metal anode engineering via atomic layer deposition. Adv. Mater., 2008, 20, 2251-2269.

[16] Y. Wang, G. Z. Cao, Synthesis and enhanced intercalation properties of nanostructured vanadium oxides. Chem. Mater., 2006, 18, 2787-2804.

[17] X. X. Zuo, J. Zhu, P. M. Buschbaum, Y. J. Cheng, Silicon based lithium-ion battery anodes: a chronicle perspective review, Nano Energy 2017, 31, 113-143.

[18] S. Goriparti, E. Miele, F. D. Angelis, E. D. Fabrizio, R. P. Zaccaria, C. Capiglia. Review on recent progress of nanostructured anode materials for Li-ion batteries." J. Power Sources 2014, 257, 421-443.

[19] A. Hagfeldt, G. Boschloo, L. Sun, L. Kloo, H. Pettersson, Dye-sensitized solar cells, Chem. Rev. 110 (2010) 6595–6663.

[20] https://en.wikipedia.org/wiki/Dye-sensitized_solar_cell

[21] D. Maheswari, D. Sreenivasan, Review of TiO_2 nanowires in dye sensitized solar cell. Appl. Solar Energy 2015, 51, 112-116.

[22] X. Y. Liu, J. Fang, Y. Liu, T. Lin, Progress in nanostructured photoanodes for dye-sensitized solar cells. Front. Mater. Sci. 2016, 10, 225-237.

[23] Mao S, Wen Z, Huang T, Hou Y, Chen J, High-performance bi-functional electrocatalysts of 3D crumpled graphene–cobalt oxide nanohybrids for oxygen reduction and evolution reactions. Energy Environ Science 2014, 7, 609–616.

[24] Flis-Kabulska I, Flis J, Sun Y, Zakroczymski T, Hydrogen evolution on plasma carburised nickel and effect of iron deposition from the electrolyte in alkaline water electrolysis. Electrochim Acta 2015, 167, 61–68.

[25] M. Gu, A. Genc, I. Belharouak, D. Wang, K. Amine, S. Thevuthasan, D. R. Baer, J. G. Zhang, N. D. Browning, J. Liu, C. Wang, Nanoscale phase separation, cation ordering, and surface chemistry in pristine $Li_{1.2}Ni_{0.2}Mn_{0.6}O_2$ for Li-ion batteries. Chem. Mater., 2013, 25, 2319-2326.

[26] W. Bian, Z. Yang, P. Strasser, R. Yang, A $CoFe_2O_4$/graphene nanohybrid as an efficient bi-functional electrocatalyst for oxygen reduction and oxygen evolution. J Power Sources 2014, 250, 196–203.

[27] Y. Z. Su, Q. Z. Xu, Q. S. Zhong, S. T. Shi, C. J. Zhang, C. W. Xu, $NiCo_2O_4$/C prepared by one-step intermittent microwave heating method for oxygen evolution reaction in splitter. J. Alloys Compd, 2014, 617, 115–119.

[28] Y. Yan, B. Y. Xia, B. Zhao, X. Wang, A review on noble-metal-free bifunctional heterogeneous catalysts for overall electrochemical water splitting. J. Mater. Chem. A, 2016, 4, 17587-17603.

[29] Y. Y. Liang, Y. G. Li, H. L. Wang, J. G. Zhou, J. Wang, T. Regier, H.J. Dai, Co_3O_4 nanocrystals on graphene as a synergistic catalyst for oxygen reduction reaction. Nat Mater., 2011, 10, 780–786.

[30] F. Song, X. Hu, Ultrathin cobalt-manganese layered double hydroxide is an efficient oxygen evolution catalyst. J. Am. Chem. Soc., 2014, 136, 16481–16484.

[31] J. Q. Tian, Q. Liu, A. M. Asiri, K. A. Alamry, X. P. Sun, Ultrathin graphitic C_3N_4 nanosheets/graphene composites: efficient organic electrocatalyst for oxygen evolution reaction, ChemSusChem, 2014, 7, 2125–2130.

[32] Q. Liu, J. T. Jin, J. Y. Zhang, $NiCo_2S_4$@graphene as a bifunctional electrocatalyst for oxygen reduction and evolution reactions. ACS Appl Mater Interfaces, 2013, 5, 5002–5008.

[33] D. H. Xiong, X. G. Wang, W. Li, L. F. Liu, Facile synthesis of iron phosphide nanorods for efficient and durable electrochemical oxygen evolution. Chem. Commun., 2016, 52, 8711–8714

[34] T. R. Cook, Y.-R. Zheng, P. J. Stang. Metal–organic frameworks and self-assembled supramolecular coordination complexes: comparing and contrasting the design, synthesis, and functionality of metal–organic materials. Chem. Rev. 2012, 113, 734-777.

[35] N. Stock, S. Biswas, Synthesis of Metal-organic frameworks (MOFs): routes to various MOF topologies, morphologies, and composites. Chem. Rev. 2011, 112, 933-969.

[36] H. Wang, Q. L. Zhu, R. Zou, Q. Xu, Metal-organic frameworks for energy applications. Chem, 2017, 2, 52-80.

[37] Y. J. Zhang, Z. Q. Xie, Z. Q. Wang, X. H. Feng, Y. Wang, A. G. Wu, Unveiling the adsorption mechansim of zeolitic imidazolate framework-8 with high efficiency for removal of copper ions from aqueous solutions", Dalton Trans, 2016, 45, 12653-12660.

CHAPTER 2. METAL-ORGANIC FRAMEWORKS DERIVED HIGH-PERFORMANCE ANODE MATERIALS FOR RECHARGEABLE LITHIUM-ION BATTERIES

2.1 Overview

In order to achieve high-performance lithium-ion batteries, the electrode materials are required to meet some basic requirements such as high specific capacity and rate capability as well as long-term cycling stability, as described in Chapter 1. Due to the low theoretical capacity (372 mAh g^{-1}) and poor rate performance of commercial graphite anode, many efforts have been made to develop various novel anode materials for LIBs with improved battery performance. New carbonaceous materials with unique nanostructure/morphology and metal oxides (Co_3O_4, SnO_2, etc.) with high theoretical capacities have demonstrated to be two promising anode materials. However, these two categories of anode materials still suffer from some drawbacks. For example, most previously reported carbonaceous materials have low electrical conductivity and poor structural stability when cycled at high charge/discharge rates as well as limited active sites for effective Li-ion storage. Among metal oxides, Co_3O_4 has a high theoretical capacity of 890 mAh g^{-1} and other attractive properties, such as great chemical and thermal stability as well as good safety during operation. Nevertheless, the huge volume change during cycling leads to its poor cycling stability and rate performance for LIBs. To overcome this challenge, one solution is to downsize Co_3O_4 into nano scale, which can partially reduce the induced stress upon cycling. A second solution is to synthesize Co_3O_4-C composite, in which the carbon matrix can accommodate the drastic volume change and also enhance the electric conductivity of electrodes.

In Chapter 2.2, ZIF-8/graphene oxide hybrid is synthesized and applied as a template/precursor to obtain N-doped porous carbon anode materials with large surface area, high electric conductivity and good structural stability, showing significantly enhanced capacity, rate performance and cycle stability compared to graphite and most previously reported carbonaceous anode materials. In Chapter 2.3, ZIF-67 is used to synthesize Co_3O_4 nanoparticles (NPs) via one-step sintering in air, and then as-obtained Co_3O_4 NPs are confined into single-walled carbon nanotubes (SWCNTs) matrix via a facile self-assembly strategy, displaying greatly enhanced lithium storage properties and cycling stability compared to pristine Co_3O_4 NPs and most previously reported metal oxides/carbon composite anode materials.

2.2 Hierarchical Sandwich-Like Structure of Ultrafine N-Rich Porous Carbon Nanospheres Grown on Graphene Sheets as Superior Lithium-Ion Battery Anodes[*]

2.2.1 Introduction

Lithium-ion batteries (LIBs) have been widely used as power sources in portable electronics[1-3]. Nevertheless, the ever-increasing demands for emerging applications in portable electronics and electric vehicles (EVs) are driving the development of LIBs with higher energy density and power density as well as longer cycling life. As one of the commercially available anode materials, graphite is the most common one but still exhibits

[*] Reprinted with permission from Zhiqiang Xie, Ziyang He, Xuhui Feng, Wangwang Xu, Xiaodan Cui, Jiuhong Zhang, Cheng Yan, Moises A. Carreon, Zheng Liu, and Ying Wang, Hierarchical sandwich-like structure of ultrafine N-rich porous carbon nanospheres grown on graphene sheets as superior lithium-ion battery anodes. ACS Appl. Mater. Interfaces, 2016, 8, 10324–10333. Copyright 2016 American Chemical Society.

some drawbacks such as a low theoretical capacity of 372 mAh g^{-1} and distinctly poorer electrochemical performances at higher charge-discharge rates, which is far from satisfactory for meeting the needs of high-energy high-power LIBs [3,4]. Thus, it is imperative to explore alternative carbonaceous electrode materials with larger capacity, improved cycling stability, better rate performance, and the potential for industrial scale production.

To develop high-performance carbonaceous electrode materials for new-generation LIBs, one strategy is to design and synthesize a novel nanostructure with the following features: (*i*) large surface area with abundant active sites to facilitate Li-ion storage capacity [5-7], (*ii*) high porosity for enhanced charge transport, thereby resulting in improved rate capability [8-10], (*iii*) excellent structural stability and electronic conductivity to promote rapid charge transfer with prolonged cycle life [11,12], and (*iv*) heteroatom N or S doping to manipulate electronic and electrochemical properties and increase number of available active sites for Li-ion storage [13-15]. To achieve these, many new carbonaceous anode materials with various nanostructures have been evaluated for lithium storage and demonstrated significantly improved performance compared to commercial graphite anodes, such as heteroatom-doped graphene sheets [12], micro/nanoporous carbon [16], hollow carbon spheres [17], carbon nanofibers [18], and carbon nanobeads [19]. In spite of these efforts, few have sought to satisfy all the aforementioned features simultaneously since most carbonaceous materials have low electrical conductivity and poor structural stability when cycled at high charge/discharge rates as well as limited active sites for effective Li-ion storage. Therefore, the lithium storage capability and rate performance of carbonaceous anodes still need improvements. By introducing more available active sites for lithium storage, incorporation of nitrogen into carbon has proven to significantly enhance both electronic conductivity and electrochemical reactivity of carbon-based anode materials, resulting in improved performance in LIBs and other energy applications [13-15,35,36]. However, the synthesis of N-rich carbonaceous nanostructures reported previously usually involve tedious processes such as complex chemical reactions, chemical vapor deposition (CVD) [20], thermal annealing with ammonia [21], and/or various template-based approaches, which are expensive and time-consuming, and thus limit their practical applications for industrial scale production. Because of these trade-offs, design and synthesis of highly porous N-rich carbonaceous anode materials with superior electrical conductivity remain a big challenge.

Metal organic frameworks (MOFs) are a family of crystalline materials with inorganic-organic hybrid structure and have been widely studied for gas separation [22], sensors [23], catalysis [24], owing to their large pore volumes and extremely high specific surface areas. Recently, MOFs have attracted much interest for the applications in LIBs and have proved to be promising precursors for constructing various nanostructured electrodes [25-28]. For instance, Yue *et al*. reported cubic mesoporous Co-ZnO@C via pyrolysis of Co-doped MOF-5, showing a reversible capacity of 725 mAh g^{-1} after 50 cycles at a specific current of 100 mA g^{-1} [26]. Han *et al*. used direct carbonization at 800^{o}C under inert atmosphere to fabricate ZIF-8@chitosan composites, which exhibit a specific capacity of 750 mAh g^{-1} after 50 cycles at a specific current of 50 mA g^{-1} [27]. Hou *et al*. reported a Co_3O_4/N-doped carbon hybrid with dodecahedrons structure that delivers 892 mAh g^{-1} after 100 cycles at a specific current of 100 mA g^{-1} [28]. Nevertheless, due to the unavoidable breakdown inside the crystalline MOFs and relatively large crystal size ranging from 250 to 500 nm, these MOFs-derived N-doped carbon matrices still exhibit poor structural stability and low electronic conductivity, and thus result in significant capacity fading over prolonged cycling in LIBs.

Herein, to achieve carbonaceous anode material with all the merits of hierarchically porous structure, superior excellent conductivity and high-level nitrogen doping, we present a

in situ synthesis approach to obtain sandwich-like, graphene-based porous nitrogen-doped carbons (PNCs@Gr) via facile pyrolysis of zeolitic imidazolate framework (ZIF-8) nanocrystals grown on graphene oxide (GO) (ZIF-8@GO), for application as a high-performance anode material in LIBs. We selectedZIF-8 as a suitable carbon precursor to yield *in situ* N-doped porous carbon due to its high N content of ~34 wt%, large porosity and high specific surface area, and meanwhile GO serves as a structure-directing agent and potential platform for nucleation, growth and stabilization of ZIF-8 nanocrystals. Due to insufficient surface functional groups of GO, the amide carbonyl groups of poly(vinylpyrrolidone) (PVP) can be utilized to enrich the functional groups of GO, which might be beneficial for the uniform growth of ZIF-8 nanocrystals on the GO sheet. During subsequent carbonization process, ZIF-8 nanoparticles are transformed to N-rich porous carbon nanospheres, meanwhile GO is thermally reduced to highly conductive graphene. Finally, the sandwich-like PNCs@Gr nanostructure with high porosity, superior electrical conductivity and rich nitrogen content is successfully synthesized and will thus boost electrochemical performance in LIBs, due to synergic effects of the highly desirable properties. As a result, the sandwich-like PNCs@Gr electrode demonstrates remarkable capacities, outstanding rate performances, as well as cycling stability that are better than most carbonaceous anode materials reported previously.

2.2.2 Experimental

Preparation of ZIF-8

ZIF-8 crystals were synthesized by mixing 0.81 g of 2-methyimidazole with 25 ml of methanol. To this solution, 0.7 g of $Zn(NO_3)_2 \cdot 6H_2O$ and 25 ml of methanol were added. . Afterwards, the mixed solution was stirred for 5 h. Finally, the solid was collected by centrifuging the mixture at 3000 rpm for 10 min followed by washing with methanol for three times. The collected solid was dried at 75^{o}C overnight before using.

Synthesis of ZIF-8@GO

Synthesis of ZIF-8@GO was carried out based on a modified approach from literature [31]. Typically, one gram of the as-prepared graphene oxide solution (8 mg mL^{-1}) was dispersed in methanol solution containing 50 mg of PVP, by sonication and stirring. Then 5 ml of $Zn(NO_3)_2 \cdot 6H_2O$ of methanol solution and 5 ml of 2-methyimidazole were separately added into GO/PVP solution (40 ml) and the mixed solution was kept for 5 h at room temperature. Afterwards, the product was collected by centrifuging at 3000 rpm for 10 min followed by washing with methanol for three times. After freeze drying, the final product (ZIF-8@GO) was obtained.

Synthesis of PNCs@Gr

The as-synthesized ZIF-8@GO was heated at 700^{o}C for 5 h under N_2 using a ramp rate of 2^{o}C/min. For comparison purpose, bare PNCs was prepared by facile pyrolysis of the as-synthesized ZIF-8 sample under the same condition.

Material characterizations

Powder X-ray diffraction (XRD) was carried out using a Rigaku MiniFlex X-ray diffractometer with Cu Kα radiation. XRD Data was collected in the range of $5^{\circ} \leq 2\Theta \leq 90^{\circ}$ at a scan rate of 2^{o}/min. Scanning electron microscopy (SEM) and energy-dispersive X-ray spectroscopy (EDS) were performed using a FEI Quanta 3D FEG FIB/SEM dual beam system. The nanostructures of the samples were investigated by transmission electron microscopy (TEM) and high-resolution TEM (HRTEM) using a JEM-2010 instrument microscope operating at 200 kV. X-ray photoelectron spectroscope (XPS) was performed using an AXIS 165 spectrometer and a twin-anode AlKa X-ray source. Thermogravimetric (TG) analysis was carried out using an SII STA7300 analyzer at a ramp rate of 1 °C/min under N_2 atmosphere. Brunauer-Emmett-Teller (BET) measurements were conducted using Quantachrome Instruments Autosorb-iQ with extra-high pure gases. Raman spectroscopy was carried out by confocal Raman system in air ambient environment (WITEC alpha300 R) with 532nm diodes laser.

Electrochemical Measurements

The working electrodes in this work were studied by integrating into 2032-type coin cells for various electrochemical measurements at room temperature. Within the coin cells, the lithium foil works as the counter electrode and all the coin cells were assembled in a glove box filled with argon. In a typical fabrication procedure of electrodes, 80 wt% PNCs or PNCs@Gr powders, 10 wt% conductive carbon (acetylene black, Alfa Aesar, 99.5%), and 10 wt% polyvinylidene fluoride (PVDF, Alfa Aesar) binder were first dissolved into 1-methyl-3-pyrrolidone (NMP) to form a homogeneous slurry, which was then uniformly coated on copper foils. Afterwards, the coated copper foils were dried in vacuum at 120˚C for a day. The commercial electrolyte for LIBs was used to construct the battery cells. Typically, 1 M $LiPF_6$ was dissolved in ethylene carbonate (EG)/ dimethyl carbonate (DMC)/diethyl carbonate (DEC) (1:1:1, v/v/v). Electrochemical performances of the as-prepared electrodes were evaluated at various current rates by using an 8-channel battery analyzer (MTI Corporation). Cyclic voltammetric (CV) measurements were carried out using a CHI605C electrochemical analyzer at a scanning rate of 0.1 mV/s.

2.2.3 Results and Discussion

A scheme showing the facile and scalable route for synthesizing PNCs@Gr in this work is presented in Figure 2.1. First, GO is modified with PVP in the solution, since many previous studies have reported that PVP working as surfactant can be absorbed onto the surface of graphene oxide sheets and then help to achieve good dispersion of graphene oxides by lowering their surface energy. In addition, amide carbonyl groups of PVP and oxygen functional groups of GO may coordinate with Zn ions and promote the uniform growth of ZIF-8 crystals on graphene oxide sheets. Next, the sandwich-like ZIF-8@GO sheet was transformed into the PNCs@Gr by direct pyrolysis in N_2 atmosphere at 700^{o}C. During this process, organic ligands (2-methylimidazolate) from ZIF-8 nanocrystals are carbonized, meanwhile part of nitrogen species and the carbon-reduced zinc metal vaporize away due to instability of nitrogen species at high temperature and low melting point of zinc [30,31]. Within this unique nanostructure, both porous N-doped carbon nanoparticles and graphene sheets not only serve as highways for fast electron transport, but also facilitate fast mass transport at electrode/electrolyte interfaces. Therefore, it is expected that the sandwich-like, graphene-based PNCs@Gr nanostructure will boost the electrochemical performance in LIBs.

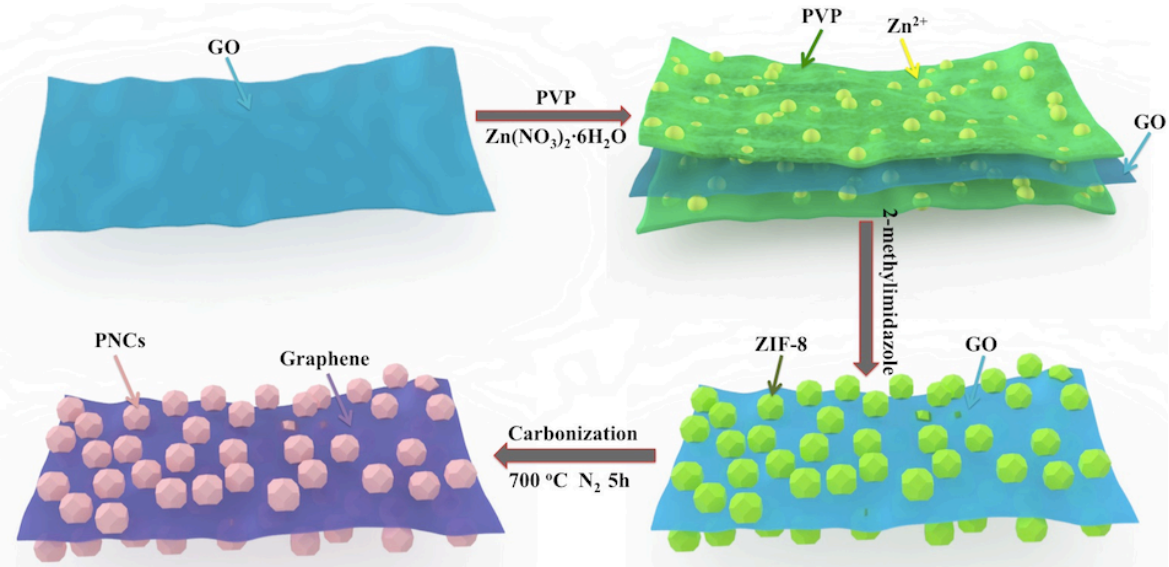

Figure 2.2.1 Scheme showing the synthetic route for preparing the sandwich-like PNCs@Gr nanostructure.

Figure 2.2.2a and b show powder X-ray diffraction (XRD) patterns of the as-synthesized samples, namely, ZIF-8, ZIF-8@GO, bare PNCs and sandwich-like PNCs@Gr nanostructure. Before carbonization, the main diffraction peaks can be readily indexed to crystalline ZIF-8 and no noticeable difference is observed between ZIF-8 and ZIF-8@GO from the XRD patterns, since the main peak of ZIF-8 (112) almost overlaps with the main peak (001) of GO at 2θ =12.5°. After carbonization, ZIF-8 and ZIF-8@GO transform to PNCs and PNCs@Gr. The XRD patterns change significantly with the main peak occurring at around 25° corresponding to the (002) reflection of graphite. The broad low-intensity peaks imply that the PNCs and PNCs@Gr have low degree of graphitization, which is consistent with previous reports of other carbonaceous materials [30-34]. It is also found that Zn diffraction peaks are not present in the XRD patterns of both PNCs and PNCs@Gr, indicating that carbon-reduced Zn metal with low melting point (419.5 °C) may have been vaporized away during the carbonization process at 700°C. The thermo-gravimetric analysis (TGA) result of pristine ZIF-8 sample. It can be seen that the ZIF-8 sample starts to decompose at around 550 °C, indicating a good thermal stability, which is beneficial for being a suitable carbonization precursor, since severe vaporization at high temperature can be avoided, thereby improving the yield of final products.

The lithium storage properties of N-doped carbonaceous anode materials highly depend on the doped nitrogen type and doping amount. Therefore, X-ray photoelectron spectroscopy (XPS) measurements of pristine ZIF-8 and bare PNCs are performed. As can be seen in Figure 2.2.2c-d, after carbonization, the high-resolution spectrum of N 1s is deconvoluted into three different peaks, namely, pyridinic N (398.3 ± 0.2 eV), pyrrolic N (399.8 ± 0.2 eV), and quaternary N (400.8 ± 0.3 eV). This phenomenon indicates successful doping of nitrogen into the resultant porous carbon during the carbonization process of N-containing organic ligands, which is consistent with previous report [31]. According to the literature [35], electronic conductivity of carbonaceous materials can be significantly increased mproved by nitrogen doping, resulting in improved charge transfer at the interface, which are highly desirable for electrodes in LIBs. Furthermore, it is believed that the presence

of nitrogen dopants introduces more defects and thus offers more available active sites to enhance the Li-ion storage properties [36].

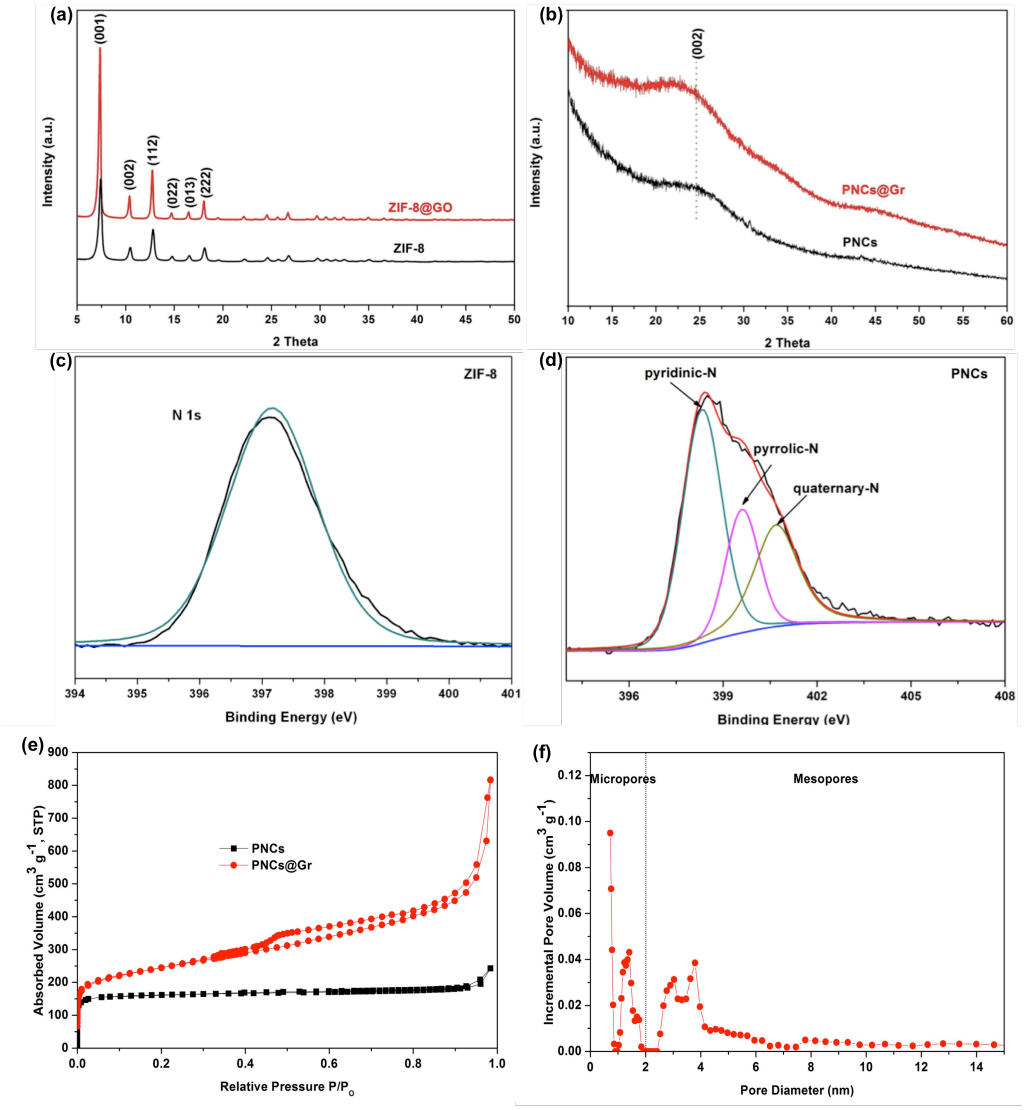

Figure 2.2.2 XRD patterns of (a) ZIF-8 and ZIF-8@GO before carbonization and (b) bare PNCs and sandwich-like PNCs@Gr nanostructure after carbonization. High-resolution spectrums of the N 1s XPS peaks of (c) ZIF-8 and (d) bare PNCs. (e) Nitrogen adsorption-desorption isotherms of bare PNCs and sandwich-like PNCs@Gr nanostructure. (f) Pore size distribution (PSD) of PNCs@Gr.

To further examine the porous structure of bare PNCs and PNCs@Gr, N_2 adsorption-desorption isotherms are performed to determine their specific surface area (SSA) and corresponding pore size distribution (PSD). As shown in Figure 2.2.2e, bare PNCs display a typical type-I isotherm showing a slight step over the relative pressure from 0.9 to 1.0, revealing a large portion of micropores, probably due to the inheritance of highly porous ZIF-8. Nevertheless, the sandwich-like PNCs@Gr shows a typical type-IV curve exhibiting a pronounced hysteresis loop. The high N_2 adsorption at the relative low pressure reveals the high microporosity, while the hysteresis loop indicates some portion of mesopores exist within the sandwich-like structure. The mesopores may originate from the evaporation of Zn during the carbonization process and likely stacking between sandwich-like PNCs@Gr.

Figure 2.2.2f shows the pore size distribution (PSD) of sandwich-like PNCs@Gr, revealing both micropores are peaked at 0.77 and 1.40 nm and mesopores are peaked at 3.05 and 3.80 nm based on the Density Functional Theory (DFT) analysis. The appropriate proportion of micropores guarantees its high SSA and mesopores are preferable for electrolyte penetration and Li-ion transport, and thus are extremely favorable for both high energy density and high rate performance in LIBs. Furthermore, thanks to the abundant micro- and mesopores, the specific surface area (SSA) of PNCs@Gr reaches as high as 872 m^2 g^{-1}, while that of bare PNCs is only 508 m^2 g^{-1}, as revealed by the Brunauer-Emmett-Teller (BET) measurements. Owing to the severe restacking of graphene sheets, the pristine rGO or graphene obtained via thermal annealing of GO proves to possess low SSA of below 100 m^2 g^{-1}[37], which is significantly lower than theoretical SSA value (2630 m^2 g^{-1}) of graphene without any overlap of sheets. Therefore, such a significant improvement in the SSA of sandwich-like PNCs@Gr is mainly attributed to synergic effects of components in this hybrid, whereas the likely agglomeration of PNCs and severe restacking of graphene sheets can be effectively addressed by this hierarchical nanostructure design. The larger surface area of PNCs@Gr is anticipated to offer more active sites for lithium ion storage, thus leading to improved specific capacity and enhanced rate capability compared to bare PNCs.

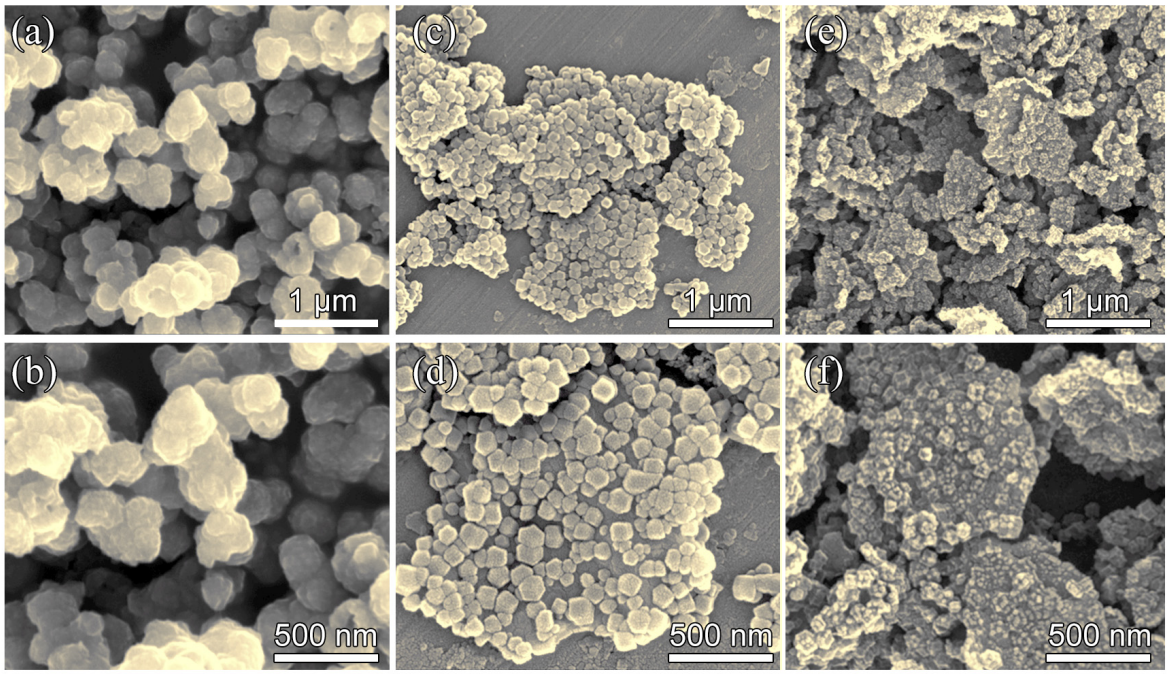

Figure 2.2.3 SEM images of (a, b) bare PNCs, (c, d) ZIF-8@GO and (e, f) sandwich-like PNCs@Gr nanostructure.

Figure 2.2.3 displays SEM images of bare PNCs, ZIF-8@GO and sandwich-like PNCs@Gr. As shown in Figure 2.2.3a and b, bare PNCs consist of numerous nanoparticles (~200 nm in diameter) with rough surfaces and severe agglomeration is also observed. Interestingly, Figure 2.2.3c and d reveal that ZIF-8@GO sample preserves the sheet-like morphology of micrometer-sized GO, in which polyhedron-like ZIF-8 nanocrystals are uniformly grown on the GO surface and their average diameter is approximately 150 nm. As shown in Figure 2.2.3e and f, the PNCs@Gr sample demonstrates that the sheet-like morphology is well preserved after direct carbonization of ZIF-8@GO at 700^{o}C. Moreover, it is observed that most PNCs in the composite of PNCs@Gr are composed of ultrafine

nanoparticles (~20 nm), likely owing to partial decomposition of ZIF-8 during the carbonization process.

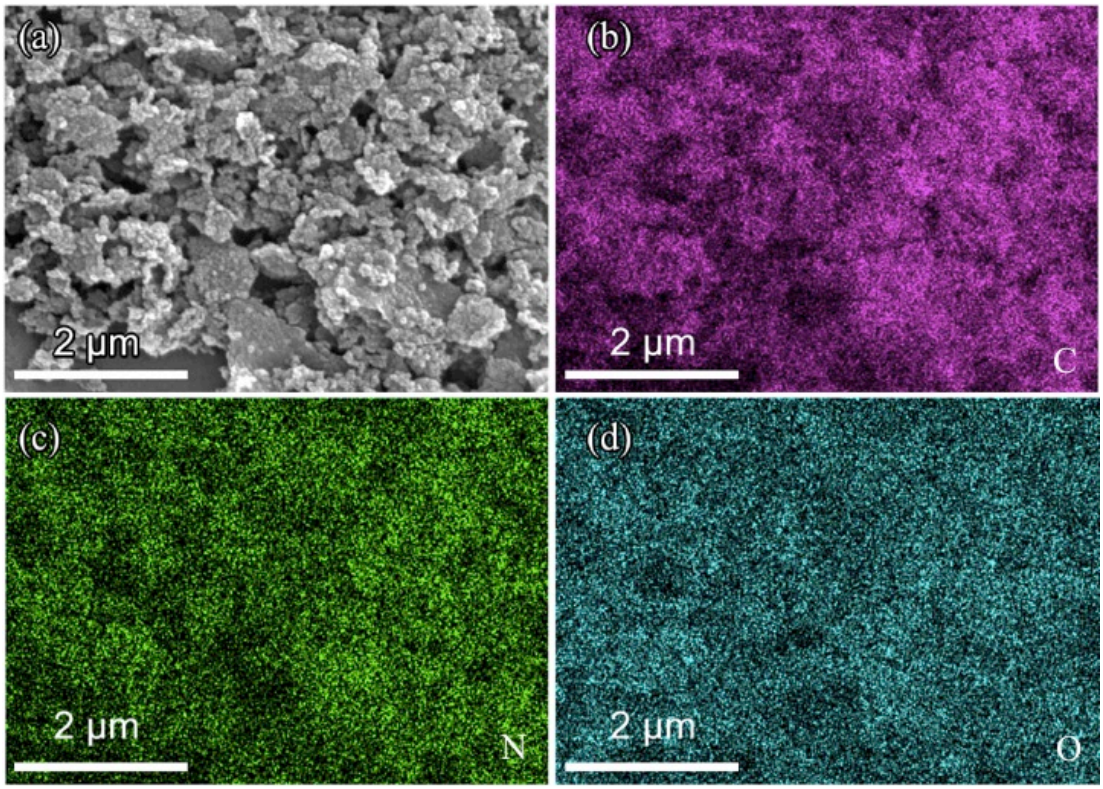

Figure 2.2.4 (a) SEM image of the sandwich-like PNCs@Gr nanostructure, and (b-d) corresponding elemental mapping results.

The composition of sandwich-like PNCs@Gr nanostructure is further analyzed by energy dispersive spectroscopy (EDS) elemental mapping. As revealed in Figure 2.2.4a-d, carbon, nitrogen, and oxygen elements are homogeneously distributed, suggesting that the PNCs derived from ZIF-8 are dispersed uniformly on the graphene sheet, and thus form a sandwich-like nanostructure. Furthermore, due to the evaporation of Zn during the carbonization process, we barely observe Zn element distribution from elemental mapping results. In addition, the PNCs@Gr sample contains 21.5 wt% nitrogen, which is significantly higher than most of previously reported N-doped carbonaceous materials in LIBs [5,16, 40, 44].

TEM characterization was also performed for better visualization of ZIF-8@GO and PNCs@Gr, as displayed in Figure 2.2.5. As can be seen in Figure 2.2.5a and b (TEM images of ZIF-8@GO at different magnifications) that ZIF-8 nanoparticles are homogeneously grown on GO sheets, which is in good agreement with the SEM observations. In addition, the HR-TEM image of ZIF-8@GO in Figure 2.2.5c reveals a very small area of exposed GO at the edges, confirms the existence of GO in the sample and the sandwich-like structure of ZIF-8@GO. After carbonization, Figure 2.2.5d-e reveal that PNCs@Gr displays apparently porous feature and preserve the sandwich-like morphology of ZIF-8@GO. The inset of Figure 2.2.5d shows the corresponding selected area electron diffraction (SAED), indicating the amorphous nature of PNCs@Gr, which is supported by the XRD result above. Finally, the HRTEM image in Figure 2.2.5f confirms the existence of graphene in the composite.

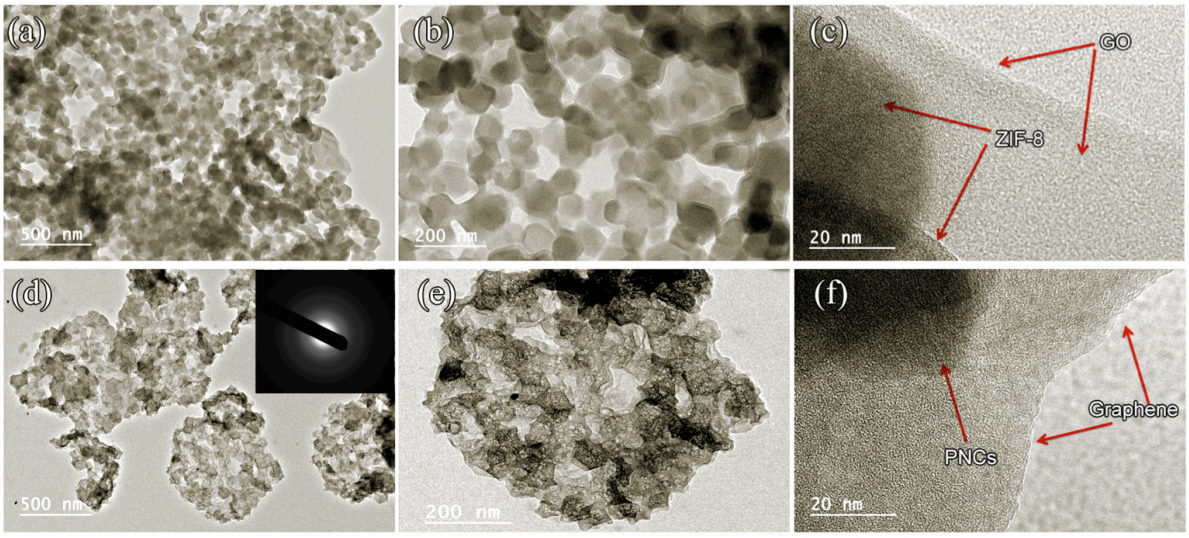

Figure 2.2.5 (a, b) TEM images of ZIF-8@GO at different magnifications, and (c) HRTEM image of ZIF-8@GO. (d, e) TEM images of the sandwich-like PNCs@Gr nanostructure at different magnifications, and (f) HRTEM image of PNCs@Gr.

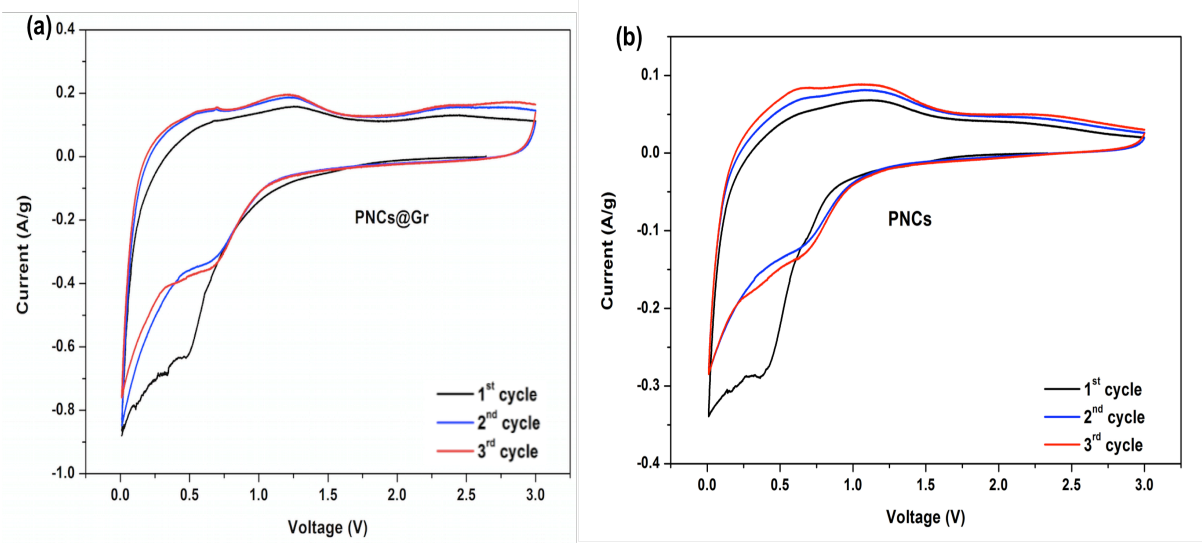

Figure 2.2.6 Cyclic voltammetry curves of (a) sandwich-like PNCs@Gr and (b) bare PNCs at a scan rate of 0.1 mVs^{-1}.

To evaluate lithium storage properties of the as-prepared bare PNCs and sandwich-like PNCs@Gr samples, various electrochemical measurements are performed. Cyclic voltammetry (CV) curves of bare PNCs and sandwich-like PNCs@Gr electrode are recorded between 0.01 and 3.0 V vs. Li/Li^+, as shown in Figure 2.2.6. Both bare PNCs and PNCs@Gr display typical CV characteristics of carbon-based anodes. However, it should be noted that the redox peaks from the PNCs@Gr electrode show obviously higher specific current than that of bare PNCs, likely resulted from the enhanced electrical conductivity and electrochemical reactivity of the electrode.

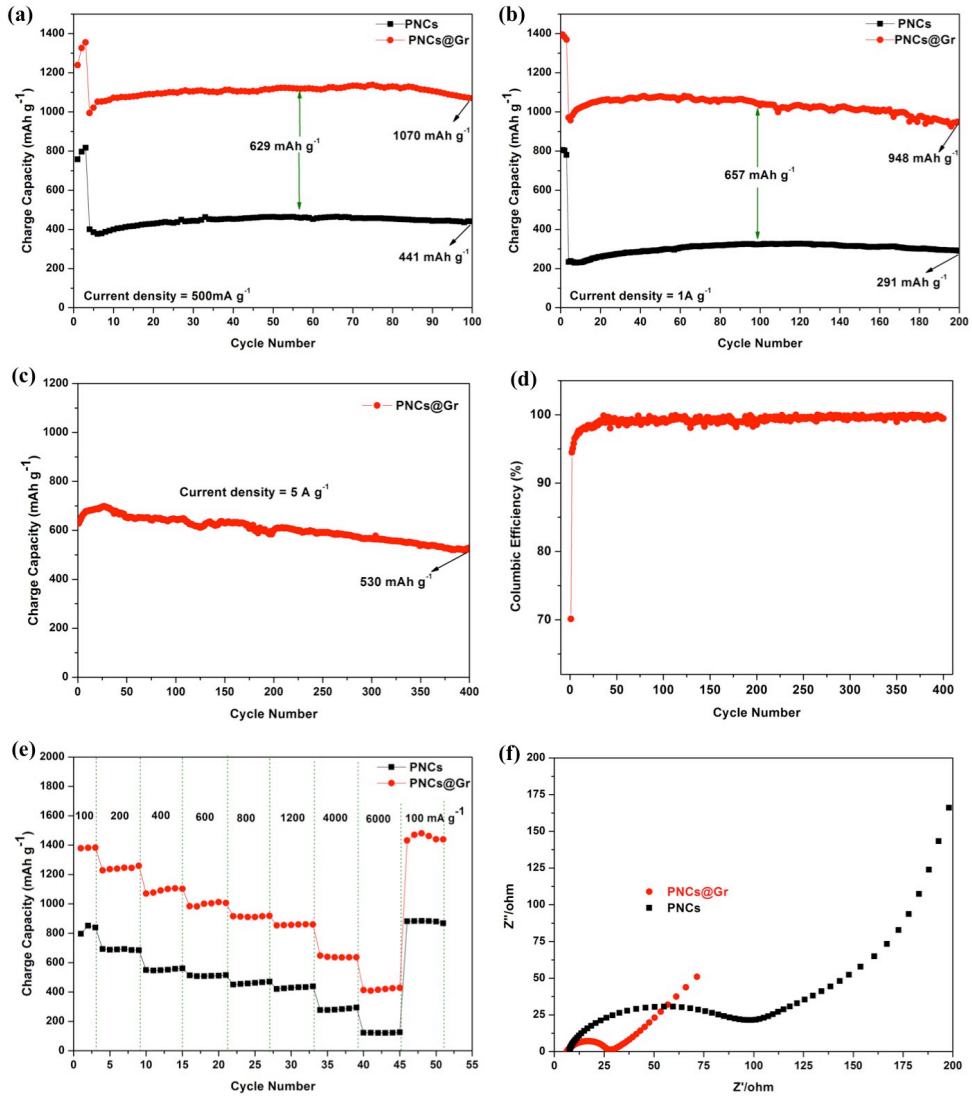

Figure 2.2.7 Electrochemical characterizations of bare PNCs and sandwich-like PNCs@Gr electrodes. (a, b) Cycling test of bare PNCs and sandwich-like PNCs@Gr electrodes at 500 mA g^{-1} and 1A g^{-1}, respectively. (c) Cycling performance of the sandwich-like PNCs@Gr electrode at 5 A g^{-1} for 400 cycles and (d) corresponding Columbic efficiency. (e) Rate capability of bare PNCs and sandwich-like PNCs@Gr electrodes cycled at various specific currents ranging from100 mA g^{-1} to 6 A g^{-1}. (f) Nyquist plots of bare PNCs and sandwich-like PNCs@Gr electrodes.

The cycling performances of both PNCs and PNCs@Gr are also evaluated at specific currents of 500 mA g^{-1} and 1 A g^{-1}, respectively. To activate the electrodes, a specific current of 100 mA g^{-1} is initially used for the first three cycles during the cycling performance. As revealed in Figure 2.2.7a-b, the PNCs@Gr anode shows an outstanding cycling performance and a high reversible capacity. At a specific current of 500 mA g^{-1}, the PNCs@Gr maintains a much higher reversible capacity of 1070 mAh g^{-1} than that of bare PNCs (441 mAh g^{-1}) after 100 cycles, showing a significant improvement of capacity by 629 mAh g^{-1}. Even at a higher specific current of 1 A g^{-1}, the PNCs@Gr can remain a high reversible capacity of 948 mAh g^{-1} after 200 cycles, which is approximately 97.7% of the 4th cycle, while the capacity of bare PNCs is only 291 mAh g^{-1}. More importantly, when the specific current reaches 5 A g^{-1}, the sandwich-like PNCs@Gr nanostructure retains a specific capacity of 530 mAh g^{-1} after 400

cycles, demonstrating a capacity retention of as high as 84.4%, as shown in Figure 2.2.7c. In addition, as shown in Figure 2.2.7d, upon prolonged cycling, the Columbic efficiency of PNCs@Gr is increased to above 99% after initial several cycles, demonstrating its excellent electrochemical reversibility. It is noted that electrochemical performances of PNCs@Gr exceed most previously reported carbon-based materials [16,18,38-45] and recently reported MOF-derived anode materials for LIBs. [16,18,27-29,39-52] Such remarkable improvements of specific capacity and long-term cycling stability are attributed to the following factors. First, in the sandwich-like PNCs@Gr nanostructure, highly desirable combination of micro- and mesopores and ultrafine carbon nanospheres (~20 nm) embedded on the graphene surface offer larger surface area (872 $m^2 g^{-1}$) in comparison with bare PNCs (508 $m^2 g^{-1}$), and thus not only result in large electrode/electrolyte interface to effectively store lithium ions, but also facilitate fast charge transfer. Second, the highly conductive, mechanically strong and flexible graphene not only improve electronic conductivity of the whole electrode, but also help reduce agglomeration and collapse of structure upon long-term cycling, resulting in excellent structural stability and superior cycling performance. Finally, the high-level nitrogen doping is believed to further enhance both electronic properties and electrochemical reactivity of PNCs@Gr electrode via introducing defects and more available active sites for lithium storage.

Notably, the PNCs@Gr anode also shows superior rate capability at various specific currents from 100 to 6000 mA g^{-1}. As displayed in Figure 2.2.7e, the reversible capacities of PNCs@Gr are 1378, 1228, 1070, 984, 915, 854 and 647 mAh g^{-1} at 100, 200, 400, 600, 800, 1200 and 4000 mA g^{-1}, respectively. Even at 6000 mA g^{-1}, the reversible capacity of PNCs@Gr remains 412 mAh g^{-1}. More importantly, when the specific current returns back to 100 mA g^{-1}, the specific capacity can be recovered to 1432 mAh g^{-1}, demonstrating its outstanding reaction reversibility and cycling stability. However, bare PNCs anode shows much lower reversible capacities of 797, 692, 550, 508, 451, 421, 277 and 123 mAh g^{-1} when cycled at 100, 200, 400, 600, 800, 1200, 4000 and 6000 mA g^{-1}, respectively. The superior rate capability of the sandwich-like PNCs@Gr electrode is ascribed to its hieratical nanostructure, in which graphene significantly improves electrical conductivity of the electrode, and ultrafine carbon nanospheres offer shorter transport length of lithium ions and better stability when cycled at higher charge/discharge rates, thereby resulting in considerable improvement in rate capability compared to bare PNCs. Therefore, it can be concluded that the PNCs@Gr anode exhibits superior rate capability, significantly improved cycling stability and reversible capacity compared to bare PNCs.

To further understand the origin of superior rate capability of sandwich-like PNCs@Gr anode, electrochemical impedance spectra (EIS) is carried out to investigate electrochemical kinetics occurring at the electrode/electrolyte interfaces and Li-ion intercalation/deintercalation within electrode materials in the battery cells. As seen in Figure 2.2.7f, the Nyquist plots of bare PNCs and PNCs@Gr shows a slanted line in the low-frequency region and a depressed semicircle in the medium-frequency region. It is observed that the electrode of sandwich-like PNCs@Gr nanostructure shows a charge transfer resistance of 30 Ω, which is much lower than that of bare PNCs (100 Ω), indicating a significantly enhanced charge transfer within the whole electrode.

Figure 2.2.8a shows the initial three cycles of the PNCs@Gr electrode at 100 mA g^{-1} from the rate performance testing. Typical charge/discharge profiles are consistent with N-doped carbonaceous anodes for LIBs [5,16]. It is observed that a large irreversible capacity loss occurs in the initial cycle, attributed to the unavoidable decomposition of the electrolyte and formation of the solid-electrolyte interphase (SEI) film [25]. Such observation is consistent with the CV results in Figure 2.2.6, in which the cathodic peaks disappear in the

2nd and 3rd cycles. The charge/discharge curves of the PNCs@Gr electrode cycled at various rates are also displayed in Figure 2.2.8b.

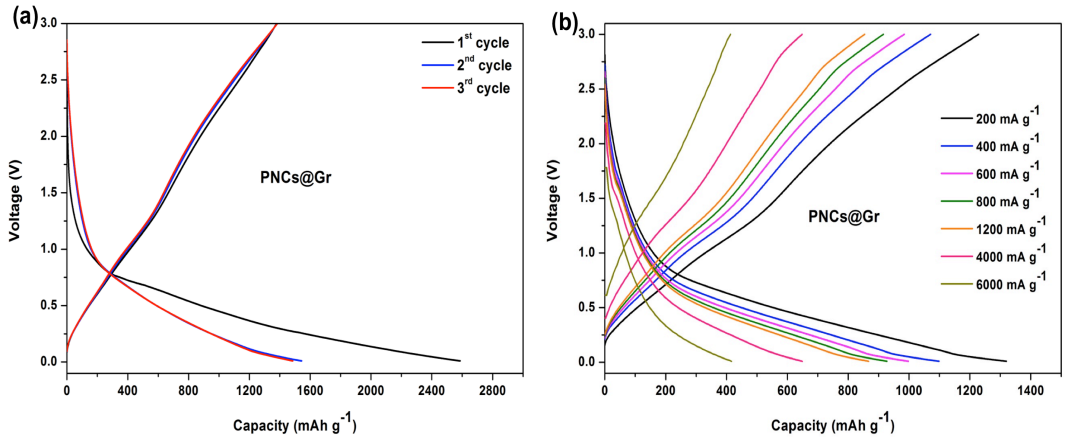

Figure 2.2.8 Charge-discharge profiles of the sandwich-like PNCs@Gr electrode (a) cycled at 100 mA g^{-1} (the initial three cycles from rate capability testing) and (b) cycled at various rates.

The super high capacity, significantly enhanced rate capability, and excellent cycling performance of sandwich-like PNCs@Gr nanostructure are ascribed to their novel nanostructure and desirable nitrogen doping. In its synthesis, *in situ* growth of ultrafine carbon nanoparticles with highly porous structure effectively reduce the agglomeration phenomenon compared to bare PNCs, and thus leads to sufficient electrode/electrolyte interface and shorter transport length of Li ions, thereby promoting rapid charge transfer. Furthermore, highly conductive and mechanically strong graphene provides continuous electron-transport pathways and stabilizes the structure upon long-term cycling. In addition, it is believed that the high-level N-doping in PNCs@Gr composite can further enhance its electronic conductivity and electrochemical reactivity, which is beneficial for its electrochemical performances in LIBs.

2.2.4 Conclusions

In conclusion, a sandwich-like, graphene-based porous nitrogen-doped carbons (PNCs@Gr) has been fabricated through direct pyrolysis of zeolitic imidazolate framework (ZIF-8) nanoparticles *in situ* grown on graphene oxide (GO) (ZIF-8@GO), for application as a promising anode material in LIBs. When tested in battery cells, the sandwich-like nanostructure exhibits high reversible capacity, better cycling stability and excellent rate capability in comparison with bare PNCs. The outstanding electrochemical performances of PNCs@Gr anode can be attributed to its novel sandwich-like nanostructure and proper N-doping in the composite. Thus PNCs@Gr demonstrates to be a promising alternative to commercial graphite anode with great potential in high-performance LIBs. In addition, the obtained sandwich-like PNCs@Gr may also be applicable for supercapacitors and other fields.

2.2.5 References

[1] S. Chu, A. Majumdar, Opportunities and challenges for a sustainable energy future. Nature, 2012, 488, 294−303.

[2] Z. Q. Xie, J. Q. Zhao, Y. Wang, One-step solvothermal synthesis of Sn nanoparticles dispersed in ternary manganese-nickel-cobalt carbonate as superior anode materials for lithium ion batteries. Electrochim. Acta, 2015, 174, 1023-1029.

[3] W. W. Xu, Z. Q. Xie, X. D. Cui, K. N. Zhao, L. Zhang, L. Q. Mai, Y. Wang, Direct growth of an economic green energy storage material: a monocrystalline jarosite-$KFe_3(SO_4)_2(OH)_6$-nanoplates@rGO hybrid as a superior lithium-ion battery cathode. J. Mater. Chem. A. 2016, 4, 3735-3742.

[4] N. A. Kaskhedikar, J. Maier, Lithium storage in carbon nanostructures. Adv. Mater. 2009, 21, 2664-2680.

[5] L. Qie, W. M. Chen, Z. H. Wang, Q. G. Shao, X. Li, L. X. Yuan, X. L. Hu, W. X. Zhang, Y. H. Huang, Nitrogen-doped porous carbon nanofiber webs as anodes for lithium ion batteries with a superhigh capacity and rate capability. Adv. Mater. 2012, 24, 2047-2050.

[6] Y. Chen, X. Li, K. Park, J. Song, J. Hong, L. Zhou, Y. W. Mai, H. Huang, J. B. Goodenough, Hollow carbon-nanotube/carbon-nanofiber hybrid anodes for Li-ion batteries. J. Am. Chem. Soc. 2013, 135, 16280-16283.

[7] L. Qie, W. Chen, H. Xu, X. Xiong, Y. Jiang, F. Zou, X. Hu, Y. Xin, Z. Zhang, Y. Huang, Synthesis of functionalized 3D hierarchical porous carbon for high-performance supercapacitors. Energy Environ. Sci. 2013, 6, 2497-2504.

[8] Y. Li, Z. Li, P. K. Shen, Simultaneous formation of ultrahigh surface area and three-dimensional hierarchical porous graphene-like networks for fast and highly stable supercapacitors. Adv. Mater. 2013, 17, 2474-2480.

[9] Y. Liang, D. Wu, R. Fu, Carbon microfibers with hierarchical porous structure from electrospun fiber-like natural biopolymer. Sci. Rep. 2013, 3, 1119.

[10] C. Hu, L. Wang, Y. Zhao, M. Ye, Q. Chen, Z. Feng, L. Qu, Designing nitrogen-enriched echinus-like carbon capsules for highly efficient oxygen reduction reaction and lithium Ion storage. Nanoscale. 2014, 6, 8002-8009.

[11] Z. Li, Z. Xu, X. Tan, H. Wang, C. M. B. Holt, T. Stephenson, B. C. Olsen, D. Mitlin, Mesoporous nitrogen-rich carbons derived from protein for ultra-high capacity battery anodes and supercapacitors. Energy Environ. Sci. 2013, 6, 871-878.

[12] Z. S. Wu, W. C. Ren, L. Xu, F. Li, H. M. Cheng, Doped graphene sheets as anode materials with superhigh rate and large capacity for lithium ion batteries. ACS Nano. 2011, 5, 5463-5471.

[13] W. H. Shin, H. M. Jeong, B. G. Kim, J. K. Kang, J. W. Choi, Nitrogen-doped multiwall carbon nanotubes for lithium storage with extremely high capacity. Nano Lett. 2012, 12, 2283-2288.

[14] Y. G. Li, W. Zhou, H. L. Wang, L. M. Xie, Y. Y. Liang, F. Wei, J. C. Idrobo, S. J. Pennycook, H. J. Dai, An oxygen reduction electrocatalyst based on carbon nanotube–graphene complexes. Nat. Nanotechnol. 2012, 7, 394-400.

[15] L. J. Yang, S. J. Jiang, Y. Zhao, L. Zhu, S. Chen, X. Z. Wang, Q. Wu, J. Ma, Y. W. Ma, Z. Hu, Boron-doped carbon nanotubes as metal-free electrocatalysts for the oxygen reduction reaction. Angew. Chem., Int. Ed. 2011, 50, 7132-7135.

[16] K. T. Lee, J. C. Lytle, N. S. Ergang, S. M. Oh, A. Stein, Synthesis and rate performance of monolithic macroporous carbon electrodes for lithium-ion secondary batteries. Adv. Funct. Mater. 2005, 15, 547-556.

[17] F. D. Han, Y. J. Bai, R. Liu, B. Yao, Y. X. Qi, N. J. Lun, X. Zhang, Template-free synthesis of interconnected hollow carbon nanospheres for high-performance anode material in lithium-ion batteries. Adv. Energy Mater. 2011, 1, 798-801.

[18] Li, C.; Yin, X.; Chen, L.; Li, Q.; Wang, T. Porous Carbon Nanofibers Derived from Conducting Polymer: Synthesis and Application in Lithium-Ion Batteries with High-Rate Capability. J. Phys. Chem. C. 2009, 113, 13438-13442.

[19] H. Wang, T. Abe, S. Maruyama, Y. Iriyama, Z. Ogumi, K. Yoshikawa, Graphitized carbon nanobeads with an onion texture as a lithium-ion battery negative electrode for high-rate use. Adv. Mater. 2005, 17, 2857-2860.

[20] D. Wei, Y. Liu, Y. Wang, H. Zhang, L. Huang, G. Yu, Synthesis of N-doped graphene by chemical vapor deposition and its electrical properties. Nano Lett. 2009, 9, 1752-1758.

[21] X. R. Wang, X. L. Li, L. Zhang, Y. Yoon, P. K. Weber, H. L. Wang, J. Guo, H. J. Dai, N-doping of graphene through electrothermal reactions with ammonia. Science 2009, 324, 768-771.

[22] T. H. Bae, J. S. Lee, W. Qiu, W. J. Koros, C. W. Jones, S. Nair, A high-performance gas-separation membrane containing submicrometer-sized metal–organic framework crystals. Angew. Chem. Int. Ed. 2010, 49, 9863-9866.

[23] B. V. Harbuzaru, A. Corma, F. Rey, J. L. Jordá, D. Ananias, L. D. Carlos, J. Rocha, A miniaturized linear pH sensor based on a highly photoluminescent self-assembled europium(III) metal–organic framework. Angew. Chem. Int. Ed. 2009, 48, 6476-6479.

[24] R. Li, J. Hu, M. Deng, H. Wang, X. Wang, Y. Hu, H. L. Jiang, J. Jiang, Q. Zhang, Y. Xie, Y. Xiong, Integration of an inorganic semiconductor with a metal–organic framework: a platform for enhanced gaseous photocatalytic reactions. Adv. Mater. 2014, 26, 4783-4788.

[25] F. C. Zheng, Y. Yang, Q. W. Chen, High lithium anodic performance of highly nitrogen-doped porous carbon prepared from a metal-organic framework", Nat. Commun. 2014,5,5261 doi: 10.1038/ncomms6261.

[26] H. Yue, Z. Shi, Q. Wang, Z. Cao, H. Dong, Y. Qiao, Y. Yin, S. Yang, MOF-derived cobalt-doped ZnO@C composites as a high-performance anode material for lithium-ion batteries. ACS Appl. Mater. Interfaces. 2014, 6, 17067-17074.

[27] Y. Han, P. Qi, S. Li, X. Feng, J. Zhou, H. Li, S. Su, X. Li, B. Wang, A novel anode material derived from organic-coated ZIF-8 nanocomposites with high performance in lithium ion batteries. Chem. Commun. 2014, 50, 8057-8060.

[28] Y. Hou, J. Y. Li, Z. H. Wen, S. M. Cui, C. Yuan, J. H. Chen, Co_3O_4 Nanoparticles embedded in nitrogen-doped porous carbon dodecahedrons with enhanced electrochemical properties for lithium storage and water splitting. Nano Energy. 2015, 12, 1-8.

[29] X. Li, W. Qi, D. Mei, M. L. Sushko, I. Aksay, J. Liu, Functionalized graphene sheets as molecular templates for controlled nucleation and self-assembly of metal oxide-graphene nanocomposites. Adv. Mater. 2012, 24, 5136-5141.

[30] H. L. Jiang, B. Liu, Y. Q. Lan, K. Kuratani, T. Akita, H. Shioyama, F. Q. Zong, Q. Xu, From metal–organic framework to nanoporous carbon: toward a very high surface area and hydrogen uptake. J. Am. Chem. Soc, 2011, 133, 11854-11857.

[31] T. Palaniselvam, B. P. Biswal, R. Banerjee, S. Kurungot, Zeolitic imidazolate framework (ZIF)-drived, hollow-core, nitrogen-doped carbon nanostructures for oxygen-reduction reactions in PEFCs. Chem. Eur. J. 2013, 19, 9335-9342.

[32] L. L. Zhang, X. S. Zhao, Carbon-based materials as supercapacitor electrodes. Chem. Soc. Rev. 2009, 38, 2520–2531.

[33] K. Jost, C. R. Perez, J. K. McDonough, V. Presser, M. Heon, G. Dion, Y. Gogotsi, Carbon coated textiles for flexible energy storage. Energy Environ. Sci. 2011, 4, 5060–5067.

[34] Y. W. Zhu, S. Murali, M. D. Stoller, K. J. Ganesh, W. W. Cai, P. J. Ferreira, A. Pirkle, R. M. Wallace, K. A. Cychosz, M. Thommes, Dong. Su, E. A. Stach, R. S. Ruoff, Carbon-based supercapacitors produced by activation of graphene. Science 2011, 332, 1537–1541.

[35] L. Zhao, Y. S. Hu, H. Li, Z. Wang, L. Chen, Porous $Li_4Ti_5O_{12}$ coated with N-doped carbon from ionic liquids for Li-ion batteries. Adv. Mater. 2011, 23, 1385-1388.

[36] J. H. Hou, C. B. Cao, F. Idrees, X. L. Ma, Hierarchical porous nitrogen-doped carbon nanosheets derived from silk for ultrahigh-capacity battery anodes and supercapacitors. ACS Nano. 2015, 9, 2556-2564.

[37] Y. Hou, Z. H. Wen, S. M. Cui, S. Q. Ci, S. Mao, J. H. Chen, An advanced nitrogen-doped graphene/cobalt-embedded porous carbon polyhedron hybrid for efficient catalysis of oxygen reduction and water splitting. Adv. Funct. Mater. 2015, 25, 872-882.

[38] M. Chen, C. Yu, S. H. Liu, X. M. Fan, C. T. Zhao, X. Zhang, J. S. Qiu, Micro-sized porous carbon spheres with ultra-high rate capability for lithium storage. Nanoscale 2015, 7, 1791-1795.

[39] J. Ou, Y. Z. Zhang, L. Chen, Q. Zhao, Y. Meng, Y. Guo, D. Xiao, Nitrogen-rich porous carbon derived from biomass as a high performance anode material for lithium ion batteries. J. Mater. Chem. A. 2015, 3, 6534-6541.

[40] D. C. Guo, F. Han, A. H. Lu, Porous carbon anodes for a high capacity lithium-ion battery obtained by incorporating silica into benzoxazine during polymerization. Chem. Eur. J. 2015, 21, 1520-1525.

[41] F. F. Wang, R. R. Song, H. H. Song, X. H. Chen, J. S. Zhou, Z. K. Ma, M. C. Li, Q. Lei, Simple synthesis of novel hierarchical porous carbon microspheres and their application to rechargeable lithium-ion batteries. Carbon. 2015, 81, 314-321.

[42] Y. M. Chen, X. Y. Li, K. S. Park, J. Song, J. H. Hong, L. M. Zhou, Y. W. Mai, H. T. Huang, J. B. Goodenough, Hollow carbon-nanotube/carbon-nanofiber hybrid anodes for Li-ion batteries. J. Am. Chem. Soc. 2013, 135, 16280-16283.

[43] D. D. Cai, S. Q. Wang, P. C. Lian, X. F. Zhu, D. D. Li, W. S. Yang, H. H. Wang, Super high capacity and rate capability of high-level nitrogen-doped graphene sheets as anode materials for lithium-ion batteries. Electrochim. Acta. 2013, 90, 492-497.

[44] X. F. Li, J. Liu, Y. Zhang, Y. L. Li, H. Liu, X. B. Meng, J. L. Yang, D. S. Geng, D. N. Wang, R. Y. Li, X. L. Sun, High concentration nitrogen doped carbon nanotube anodes with superior Li^+ storage performance for lithium rechargeable battery application. J. Power Sources. 2012, 197, 238-245.

[45] Z. Li, Z. W. Xu, X. H. Tan, H. L. Wang, C. M. B. Holt, T. Stephenson, B. C. Olsen, D. Mitlin, Mesoporous nitrogen-rich carbons derived from protein for ultra-high capacity battery anodes and supercapacitors. Energy Environ. Sci. 2013, 6, 871-878.

[46] G. Huang, F. F. Zhang, X. C. Du, Y. L. Qin, D. M. Yin, L. M. Wang, Metal organic frameworks route to in situ insertion of multiwalled carbon nanotubes in Co_3O_4 polyhedra as anode materials for lithium-ion batteries. ACS. Nano. 2015, 9, 1592-1599.

[47] G. H. Zhang, S. C. Hou, H. Zhang, W. Zeng, F. L. Yan, C. C. Li, H. G. Duan, High-performance and ultra-stable lithium-ion batteries based on MOF-derived ZnO@ZnO quantum dots/C core-shell nanorod arrays on a carbon cloth anode. Adv. Mater. 2015, 27, 2400-2405.

[48] A. Banerjee, U. Singh, V. Aravinda, M. Srinivasan, S. Ogale, Synthesis of CuO nanostructures from Cu-based metal organic framework (MOF-199) for application as anode for Li-ion batteries. Nano Energy. 2013, 2, 1158-1163.

[49] S. J. Yang, S. H. Nam, T. H. Kim, J. H. Im, H. S. Jung, J. H. Kang, S. G. Wi, B. W. Park, C. R. Park, Preparation and exceptional lithium anodic performance of porous carbon-coated ZnO quantum dots derived from a metal–organic framework. J. Am, Chem. Soc. 2013, 135, 7394-7397.

[50] X. D. Xu, R. G. Cao, S. Y. Jeong, J. Cho, Spindle-like mesoporous α-Fe2O3 anode material prepared from MOF template for high-rate lithium batteries. Nano Lett. 2012, 12, 4988-4991.

[51] Z. L. Xiu, M. H. Alfaruqi, J. H. Gim, J. J. Song, S. J. Kim, T. V. Thi, P. T. Duong, J. P. Baboo, V. Mathew, J. K. Kim, Hierarchical porous anatase TiO_2 derived from a titanium metal–organic framework as a superior anode material for lithium ion batteries. Chem. Commun. 2015, 51, 12274-12277.

2.3 Facile Self-Assembly Route to Co_3O_4 Nanoparticles Confined into Single-Walled Carbon Nanotube Matrix for Highly Reversible Lithium Storage*

2.3.1 Introduction

In Chapter 2.2, ZIF-8/graphene oxide hybrid is proved to be a suitable carbon precursor to synthesize porous carbon anode materials with significantly improved battery performance. This Chapter 2.3 introduces another Co-based MOF (ZIF-67), which is applied as a single precursor to synthesize ultrafine Co_3O_4 nanoparticles. Furthermore, SWCNTs with excellent conductivity and mechanical properties are employed to obtain Co_3O_4 nanoparticles confined with the SWCNTs matrix for high-performance LIBs.

Up to date, a rich variety of emerging anode materials have been extensively exploited as promising alternatives to replace commonly used graphite, including lithium alloys (Sn, Al, Si etc) [1, 2], nitrides [3], polymers [4], carbon nanomaterials (graphene, carbon nanotubes etc) [5, 6], transition metal oxides (SnO_2 [7], TiO_2 [8], Co_3O_4 [9, 10]) and their composites. Among these materials, Co_3O_4 clearly stands out as a promising candidate, thanks to its high theoretical capacity of 890 mAh g^{-1} and other attractive properties, such as highly reactive facets, great chemical/thermal stability as well as good safety during operation [10, 11]. Unfortunately, the fundamental problems of transition metal oxides (TMOs) such as huge volume changes, serious particle aggregation and low intrinsic electric conductivity, lead to severe pulverization of electrodes, thereby resulting in fast capacity decay upon prolonged cycling and inferior rate performance.

To overcome the aforementioned challenges, one appealing strategy is to design nanostructures with unique morphologies, such as plates [11], nanoparticles (NPs) [11], nanowires [12], and octahedral cages [13], which possess a high surface-to-volume ratio, thereby not only providing abundant reaction sites and shorter diffusion paths of lithium ions, but also alleviating volume strain. Other effective strategies include constructing Co_3O_4/carbon hybrid nanostructures, such as Co_3O_4@carbon [14-20], Co_3O_4@graphene [21,22] and Co_3O_4@carbon nanotubes (Co_3O_4@CNTs) composites [23-25]. The carbonaceous components within such composites can not only function as mechanical support to cushion the drastic volume change of Co_3O_4 upon cycling, but also offer continuous charge transport pathways. However, most of the previous attempts in fabricating Co_3O_4/carbon hybrid nanostructures introduced new challenges for their practical applications. For example, the commonly used methods for Co_3O_4@carbon usually require complicated synthetic processes, and thus are costly, tedious and time-consuming. Furthermore, the resulted composites still possess relatively low electronic conductivity and poor mechanical properties, thereby leading to limited enhancement in LIB performances. More importantly, the loading amount of active materials in such composites is usually below 50 wt% and can not be well controlled during preparation, which severely hinder their practical applications in high-performance LIBs.

The Co_3O_4@graphene and Co_3O_4@CNTs composites have been explored to further enhance the lithium storage properties for LIBs [21,22,24,25], however, most of the reported methods cannot achieve high mass loading of nanoparticles on CNTs or graphene. It was also found that Co_3O_4 NPs are usually decorated onto the surface of CNTs or graphene sheets *via* weak physical adsorption, which can be prone to severe aggregation and likely desorbed from the surface after dozens of electrochemical cycles, thereby dramatically diminishing their cycling stability and rate capability [23,24]. In addition, for most previously reported reduced

* Reprinted with permission from Zhiqiang Xie, Chengmin Jiang, Wangwang Xu, Xiaodan Cui, Carlosde los Reyes, Angel A. Martí, Ying Wang, Facile self-assembly route to Co_3O_4 nanoparticles confined into single-walled carbon nanotube matrix for highly reversible lithium storage. Electrochim. Acta, 2017, 235, 613-622. Copyright 2017 Elsevier.

graphene oxide (RGO)-based or acid-assisted CNT-based electrode composites, the presence of remaining intrinsic and extrinsic oxygen-related functional groups or defects in resultant graphene or CNTs could likely deteriorate their electrical conductivity, and thus lead to limited rate performance enhancement in LIBs. To solve the aforementioned problems, it is highly desirable to prepare the Co_3O_4 nanoparticles well confined into the highly conductive and mechanically strong CNT matrix using a simple but controllable fabrication method.

More recently, we have studied how to obtain single-walled carbon nanotubides (SWCNTDs) dispersions with controllable concentration. SWCNTDs are chemically reduced CNTs bearing negatively charged surfaces, which still maintain excellent electrical conductivity and mechanical properties [26]. After adding polar aprotic solvents, the SWCNTDs could spontaneously exfoliate in solutions due to the Coulombic repulsion between individual nanotubes. Compared with other dispersion methods, such as surfactant-assisted dispersion, SWCNTDs could solubilize without assistance of sonication and more importantly the SWCNTDs dispersions could be compatible with various metal oxides such as Co_3O_4 (which is incompatible with strongly acidic solutions). Nevertheless, to our best knowledge, the application of SWCNTDs in constructing single-walled carbon nanotube (SWCNT)-based electrode materials for LIBs has never been previously reported. Benefiting from better electrical conductivity and mechanical robustness of SWCNT than commonly used carbonaceous materials (amorphous carbon, RGO and strong acid treated CNTs) in the electrodes, it is expected that the Co_3O_4@SWCNT composite would enhance the electrochemical performances of LIBs.

In this project, a robust controllable preparation of Co_3O_4 nanoparticles uniformly confined into a sheet-like SWCNT matrix (Co_3O_4 NPs@SWCNT heterostructures) with a high mass loading content of up to ~ 83 wt% has been developed via evaporation-induced self-assembly (EISA) of SWCNTD dispersions. As shown in Figure 2.3.1a and b, Co_3O_4 NPs@SWCNT heterostructures are expected to possess highly desirable features for application as high-performance LIB anode materials. First, such heterostructures have high mass loading of high-capacity Co_3O_4 NPs, which can significantly improve practical energy density of the entire electrode. Second, the ultrasmall Co_3O_4 NPs with high crystallinity offer shorter pathways for charge transport, and meanwhile the SWCNT sheet-like matrix also provides continuous fast charge transport pathways. More importantly, the intimate contact between Co_3O_4 NPs and flexible SWCNT sheet can effectively suppress aggregation of Co_3O_4 NPs and facilitate their strain relaxation and therefore, the structural integrity of the entire electrode can be maintained. Benefiting from its structure, the resultant optimal Co_3O_4 NPs@SWCNT samples were studied as LIB anode materials and demonstrate highly reversible capacity, improved long-term cycling performance and rate capability. Taking such remarkable electrochemical performances and facile, controllable fabrication method into consideration, the concept of electrode materials design and preparation demonstrated here may shed light on future development of high-performance TMOs-based anodes for LIBs. Notably, we believe the synthetic approach reported in this work can be generalized to form various SWCNT-based hybrid nanostructures for applications in supercapacitors, water splitting and other fields.

2.3.2 Experimental

Preparation of ZIF-67 and Co_3O_4 nanoparticles

In brief, 0.3 g cobalt nitrate hexahydrate and 0.6 g 2-methylimidazole were separately dissolved in 15 mL methanol, respectively. Afterwards, the two solutions were mixed under stirring for 10 min and aged for 24 h at room temperature. The resultant purple solid was

collected from the solution by centrifugation at 4000 rpm for 10 min and then washed with methanol at least three times. After washing, the zeolitic imidazolate framework-67 (ZIF-67) powders were dried overnight at 80 °C. Afterwards, the Co_3O_4 nanoparticles were prepared by a facile calcination of ZIF-67 nanocrystals at 350 °C for 2 hours in air.

Preparation of SWCNTDs and SWCNTD dispersions

Synthesis of SWCNTDs was performed following our reported method [26]. Briefly, 119.5 mg potassium metal (3.1 mmol), 284 mg naphthalene (2.22 mmol), and 93 mL anhydrous tetrahydrofuran (THF) were transferred to a round-bottom flask and kept stirring for 3 days at room temperature, until no apparent solid observed. The produced potassium naphthalenide stock solution in dark green color was used within 24 h. Purified 150 mg SWCNTs synthesized via the high-pressure monooxide conversion (HiPco) process (HiPco SWCNTs) and 24 mL stock potassium naphthalenide solution were transferred to a dry round-bottom flask and kept stirring for 2 days at room temperature. The resultant solid was filtered using 0.45 μm polytetrafluoroethylene (PTFE) membranes, and rinsed with anhydrous THF to produce SWCNTDs. The SWCNTD solids were dried overnight under vacuum at room temperature. All of the above work was carried out inside a nitrogen-filled glovebox.

The SWCNTD solid was dispersed in dimethyl sulfoxide (DMSO) at an initial mixture concentration of 9 mg/mL, and the mixture was stirred overnight, following by centrifugation at 9900 g to remove undispersed solid. The supernatant was collected and its solubility was determined by UV-Vis spectrum based on the previously established proportional constant [26].

Preparation of Co_3O_4 NPs@SWCNT heterostructures

Co_3O_4 NPs@SWCNT heterostructures with three weight ratios of 4:1, 5:1 and 6:1 are prepared by simply mixing Co_3O_4 nanoparticles into SWCNTD solutions in DMSO and shaking in a VWR mini shaker at speed of 1000 rpm for 24 hours. The materials are then heated at 110 °C under vacuum for one day for complete drying.

Materials characterization

The X-ray diffraction (XRD) data were recorded at a constant scanning rate of 2 °/min on a Rigaku MiniFlex X-ray diffractometer (Cu Kα radiation). The scanning electro microscopy (SEM) imaging was carried out on a FEI Quanta 3D FEG FIB/SEM, which is equipped with Energy-dispersive X-ray spectroscopy (EDS). Transmission electron microscopy (TEM) and high-resolution TEM (HRTEM) imaging was performed on a JEOL JEM-2010 microscope at 200 kV. Raman analysis of the samples were conducted using a Renishaw inVia Raman microscope equipped with 785 nm laser and WiRe software. Thermogravimetry (TG) data were collected using an SII STA7300 analyzer in air.

Electrochemical measurements

All the battery testings were performed in 2032 coin-type cells between 0.01-3.0 V at room temperature. Pure lithium foil was used as counter electrode. Briefly, the working electrodes were prepared by coating the mixture of active materials (Co_3O_4 NPs@SWCNT), acetylene black and polyvinylidene fluoride (8:1:1, wt/wt/wt) onto a Cu substrate. Afterwards, the anodes were completely dried in a vacuum oven at 120 °C overnight. The commercial

electrolyte we used is 1 M $LiPF_6$ in ethylene carbonate/dimethyl carbonate/diethyl carbonate (1:1:1, v/v/v). All the working electrodes were assembled in a glove box with argon gas filled. All potentials are given *vs.* the Li/Li^+ semi-couple.

2.3.3 Results and discussion

Fig. 3.1c displays a scheme depicting the facile, controllable synthetic process for preparing Co_3O_4 NPs@SWCNT heterostructures via EISA of SWCNTDs. In this work, we use Co_3O_4 as an example and such a strategy could be expanded to other TMOs. Briefly, Co_3O_4 nanoparticles are simply obtained by facile calcination of metal-organic framework ZIF-67 nanocrystals. Afterwards, the resultant Co_3O_4 nanoparticles (Co_3O_4 NPs) are directly mixed with the as-prepared SWCNTDs in DMSO, followed by continuous shaking for 24 hours at room temperature. During the pre-mixing process, Co_3O_4 NPs can be well dispersed in the mixed solution and tend to spontaneously self-assembly on the negatively charged surfaces of SWCNTs. As the solvent gradually evaporates under vacuum, the SWCNTs form a continuous network that joins the particles together. Finally, the Co_3O_4 NPs@SWCNT heterostructures are obtained with controllable compositions. Within such unique nanostructure, Co_3O_4 nanoparticles are uniformly confined into a highly conductive, mechanically strong and flexible SWCNT matrix. Unlike most of the reported nanoparticle-decorated CNTs- the majority of which still suffer from severe nanoparticle aggregation, low loading of active materials, and unsatisfactory mechanical protection- the Co_3O_4 NPs@SWCNT heterostructures in this work can well address all the aforementioned problems, which are expected to boost the electrochemical performances in LIBs.

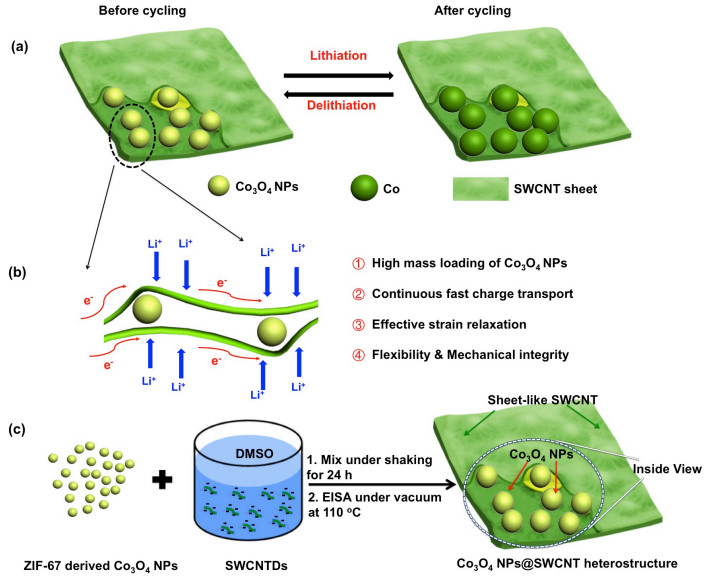

Figure 2.3.1 (a, b) Schematic illustrations of Co_3O_4 NPs@SWCNT heterostructure during electrochemical cycling. (c) Fabrication process of the Co_3O_4 NPs@SWCNT heterostructure.

To clarify the crystalline structures of the Co_3O_4 NPs@SWCNT heterostructures, X-ray diffraction (XRD) measurements of three composite samples with various weight ratios (Co_3O_4: SWCNT= 4:1, 5:1 and 6:1) are carried out. As revealed in Figure 2.3.2a, the main diffraction peaks detected for all the three Co_3O_4 NPs@SWCNT heterostructures are readily indexed to the cubic spinel Co_3O_4 (JPCDS No.42-1467) [27]. Raman spectroscopy is performed to further confirm the hybrid nanostructures due to its better sensitivity to a short-range order. Figure 2.3.2b displays typical Raman spectra of pristine SWCNT and Co_3O_4 NPs@SWCNT heterostructures. It can be seen that the black trace displays characteristic

features of SWCNTs: D band at 1303 cm^{-1}, G band at 1552 and 1591 cm^{-1}, and 2D band at 2607 cm^{-1} [28]. The characteristic splitting of the G band reveals the two mode vibrations of SWCNTs. Specifically, one is in the axis of SWCNTs and the other one is circumstance. Raman spectra of the three Co_3O_4 NPs@SWCNT heterostructures exhibit all the characteristic peaks appearing in the typical spectrum of SWCNTs and new peaks at 479.1, 617.6 and 689.5 cm^{-1}. These new peaks at 479.1 and 689.5 cm^{-1} are attributed to the E_g and A_{1g} mode vibrations of the crystalline Co_3O_4, respectively. Furthermore, it is noticed that the relative peak intensities of the D band for three Co_3O_4 NPs@SWCNT heterostructures are apparently larger than that of bare SWCNTs, which could be due to an increase in the number of sp^3 carbons in the SWCNTs which is related process of incorporation of Co_3O_4 NPs in the material. Thus, SWCNTs are successfully incorporated with Co_3O_4 NPs, forming the unique Co_3O_4 NPs@SWCNT heterostructures.

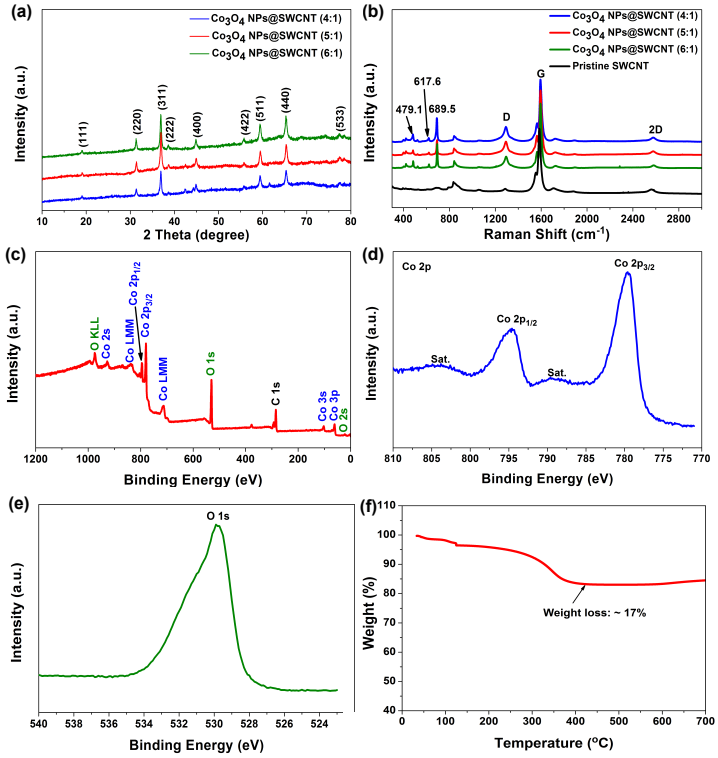

Figure 2.3.2 (a) XRD patterns and (b) Raman spectra of Co_3O_4 NPs@SWCNT heterostructures with different weight ratios of 4:1, 5:1 and 6:1, respectively. The samples are excited at 785nm. (c) XPS survey spectrum of the optimal Co_3O_4 NPs@SWCNT (5:1) heterostructure. The corresponding high-resolution XPS spectrum of (d) Co 2p, (e) O 1s. (f) Thermogravimetric curve of the optimal Co_3O_4 NPs@SWCNT (5:1) heterostructure.

Experiments presented further in the manuscript show that the Co_3O_4 NPs: SWCNT (5:1) sample demonstrates the best electrochemical performances, and therefore we perform a detailed X-ray photoelectron spectroscopy (XPS) study to address its chemical composition. XPS characterizations are performed between 0-1200 eV. As presented in Figure 2.3.2c, the XPS survey spectrum confirms the presence of elemental C, O and Co in the heterostructures. The high-resolution XPS spectrum of Co 2p in Figure 2.3.2d displays two bands at 795.6 eV and 780.1 eV, which are attributed to characteristic Co $2p_{1/2}$ and Co $2p_{3/2}$ peaks of Co_3O_4 [15]. As revealed in Figure 2.3.2e, the XPS peak of O 1s appears at 530.2 eV, corresponding to oxygen species in the Co_3O_4 phase [29]. Thermogravimetric (TG) analysis as presented in Figure 2.3.2f indicates that the mass percentage of Co_3O_4 in the Co_3O_4 NPs@SWCNT

heterostructures is ~83%, which is consistent with its nominal amount, suggesting the well controllable composition of as-prepared samples through facile EISA of SWCNTDs.

Scanning electron microscopy (SEM) characterizations are performed to demonstrate the morphologies of Co_3O_4 NPs@SWCNT heterostructures. As observed in the typical SEM image of the optimal Co_3O_4 NPs@SWCNT (5:1) in Figure 2.3.3a, the sample clearly displays a sheet-like morphology with a large area of several tens of μm^2. The highly dense SWCNT sheets with relatively smooth surfaces can be well recognized by the top view SEM image in high magnification in Figure 2.3.3b-c, and the Co_3O_4 nanoparticle aggregates are barely observed, suggesting the desirable confinement of Co_3O_4 NPs into the SWCNT sheets. Transmission electron microscopy (TEM) studies are carried out as well for better visualization of the Co_3O_4 NPs@SWCNT heterostructure (Figure 2.3.3d and e**)**. Figure 2.3.3e clearly shows that numerous Co_3O_4 NPs are relatively uniformly distributed onto the continuous SWCNT sheet without any noticeable particle aggregation, whereas the Co_3O_4 NPs are marked in yellow circles. The corresponding selected-area electron diffraction (SAED) pattern is displayed in Figure 2.3.3f, in which the bright polycrystalline diffraction rings are readily indexed to (220), (311), (400) (511) and (440) planes of spinel Co_3O_4. The elemental distributions of Co_3O_4 NPs@SWCNT heterostructure are further examined by EDS elemental mapping. As revealed in Fig. 3h-j, the C, Co and O elements are homogeneously distributed, indicating the Co_3O_4 NPs and SWCNTs are successfully mixed with each other through a facile EISA process. It is noteworthy that the loading amount of Co_3O_4 NPs in the heterostructured sample can be calculated to be as high as 83 wt%, which is among the highest loadings achieved among various reported Co_3O_4@carbon aerogel, Co_3O_4@graphene and Co_3O_4@CNTs composites [30-33].

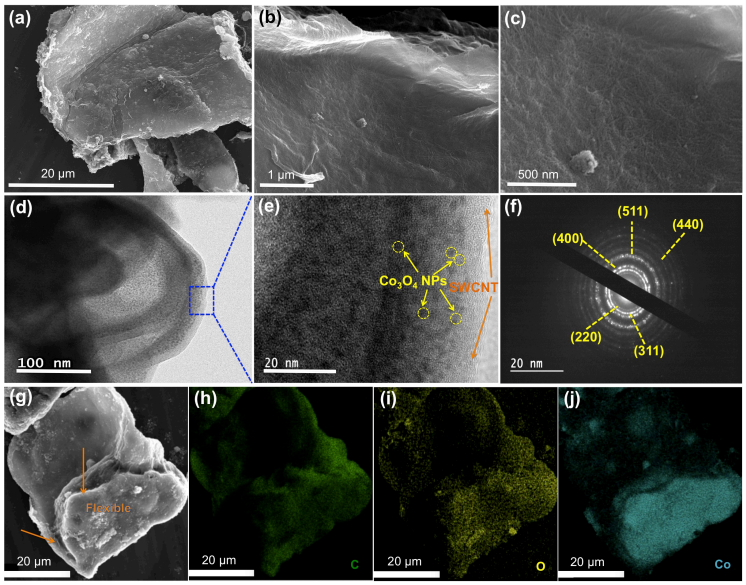

Figure 2.3.3 (a) Typical SEM image and (b-c) top view SEM image of the optimal Co_3O_4 NPs@SWCNT (5:1) heterostructure in high magnification. (d) TEM image and (e) High-resolution TEM image and (f) Electron diffraction pattern of the optimal Co_3O_4 NPs@SWCNT (5:1) heterostructure. (g) SEM image of the optimal Co_3O_4 NPs@SWCNT (5:1) heterostructure and its corresponding EDS elemental mapping of (h) C, (i) O and (j) Co, respectively.

To analyze the lithium storage properties of Co_3O_4 NPs@SWCNT heterostructures as high-performance anode materials in LIBs, various electrochemical tests are performed. The electrochemical properties of pristine Co_3O_4 are also tested as controls. Cyclic voltammetry

(CV) is first carried out to study the electrochemical process of pristine Co_3O_4 and Co_3O_4 NPs@SWCNT (5:1) electrodes, as revealed in Figure 2.3.4a. As for the pristine Co_3O_4 (Fig. S2), the main cathodic peak appears at 0.82 V in the initial cycle, which is mainly ascribed to the electrochemical reduction of Co_3O_4 with lithium to metallic Co and the evolution of solid electrolyte interphase (SEI) layer [34,35]. The main anodic peak appears at 2.09 V, which corresponds to the oxidation of Co to Co_3O_4. During subsequent cycles, it is found that the cathodic peak is shifted to 1.10 V. The Co_3O_4 NPs@SWCNT (5:1 loading) shows similar electrochemical features with that of pristine Co_3O_4 (Fig. 4a). However, it is noteworthy that the specific current of redox peaks from the Co_3O_4 NPs@SWCNT electrode is higher than that of pristine Co_3O_4, which might be ascribed to the improved electric conductivity and better electrochemical reactivity. Furthermore, it is clearly observed that the subsequent four electrochemical curves of Co_3O_4 NPs@SWCNT are very similar, indicating significantly improved electrochemical reversibility and better structural stability compared to pristine Co_3O_4. Figure 2.3.4b presents representative charge/discharge profiles of the optimal Co_3O_4 NPs@SWCNT (5:1) heterostructure in the first three cycles at 100 mA g^{-1}. As we can see that the Co_3O_4 NPs@SWCNT (5:1) provides a high initial discharge capacity of 1520 mAh g^{-1}, mainly attributed to the evolution of SEI layer [22, 36-38]. It is also found that three Co_3O_4 NPs@SWCNT heterostructures display similar initial discharge/charge capacities.

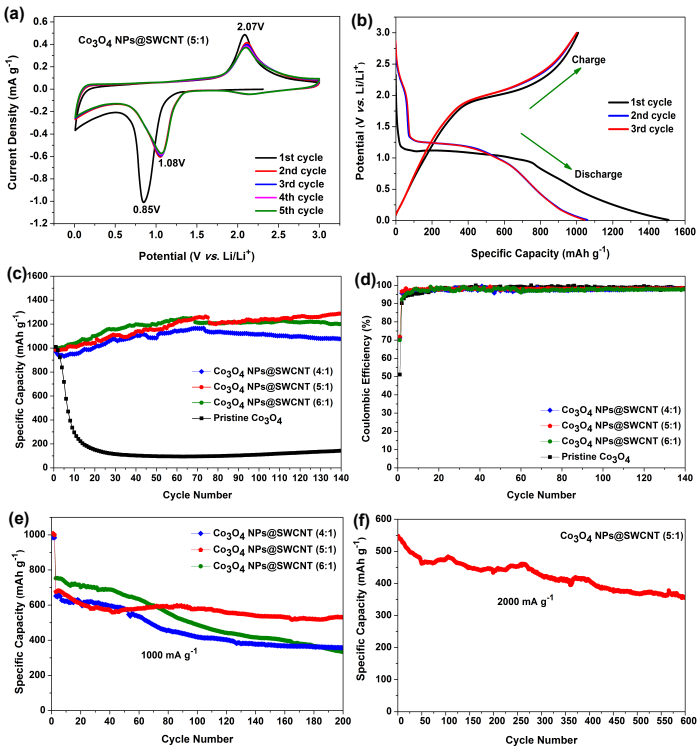

Figure 2.3.4 (a) Cyclic voltammogram (CV) curves of the optimal Co_3O_4 NPs@SWCNT (5:1) heterostructure. (b) Galvanostatic charge/discharge curves of the first three cycles for the optimal Co_3O_4 NPs@SWCNT (5:1) heterostructure electrode. (c) Cycling performances of pristine Co_3O_4 NPs and three Co_3O_4 NPs@SWCNT heterostructures at 100 mA g^{-1}. (d) The corresponding Coulombic efficiencies of four samples cycled at 100 mA g^{-1}. (e) Cycling performances of three Co_3O_4 NPs@SWCNT heterostuctures over 200 cycles at 1000 mA g^{-1}. (f) Cycling performance of the optimal Co_3O_4 NPs@SWCNT (5:1) heterostructure over 600 cycles at a higher specific current of 2000 mA g^{-1}.

To directly compare cycling stability of three Co_3O_4 NPs@SWCNT heterostructures with different loading amounts of Co_3O_4, their cycling performances at 100 mA g^{-1} are first investigated. For comparison purpose, pristine Co_3O_4 electrode is also tested under the same conditions. As can be seen in Figure 2.3.4c, after 140 cycles, all three Co_3O_4 NPs@SWCNT heterostructures, namely, Co_3O_4 NPs@SWCNT (4:1), Co_3O_4 NPs@SWCNT (5:1) and Co_3O_4 NPs@SWCNT (6:1), exhibit a high specific capacity of 1076, 1286 and 1201 mAh g^{-1}, respectively. It is observed that the Co_3O_4 NPs@SWCNT (5:1) demonstrates the highest capacity among them, suggesting this sample has the optimal loading of Co_3O_4. However, the capacity of pristine Co_3O_4 fades fast from 1008 mAh g^{-1} to only 143 mAh g^{-1} after 140 cycles, showing a capacity retention of only 10.9%, which can be attributed to severe electrode pulverization caused by drastic volume changes upon cycling. In addition, it is found that the reversible capacities of all three Co_3O_4 NPs@SWCNT heterostructures gradually increase with the increase of cycling numbers, likely due to the gradually continuous decomposition of Li_2O produced in the initial several cycles and the likely reversible formation of the polymer gel-like layer. As shown in Figure 2.3.4d, the initial Coulombic efficiency (CE) of the optimal Co_3O_4 NPs@SWCNT (5:1) is 71.2%, which is much higher than that of pristine Co_3O_4 (~51.0%), implying the advantage of highly conductive and mechanically strong SWCNT sheet-like matrix in such composite. Compared to pristine Co_3O_4, the significantly enhanced cycling stability of three Co_3O_4 NPs@SWCNT heterostructures in terms of initial cycle Coulombic efficiency and cycling performance can be presumably attributed to the synergic effects of high-capacity Co_3O_4 NPs and the highly conductive, mechanically strong and flexible SWCNT sheet-like matrix, which can well accommodate drastic volume changes and significantly improve the electric conductivity of the entire electrode, thereby enabling the full utilization of Co_3O_4.

To further evaluate the rate capability and long-term cycling performance, galvanostatic discharge/charge tests of three Co_3O_4 NPs@SWCNT heterostructures are carried out at 1000 mA g^{-1} for over 200 cycles. As displayed in Figure 2.3.4e, the Co_3O_4 NPs@SWCNT (5:1) electrode can maintain a specific capacity of 530 mAh g^{-1} after 200 cycles, which significantly outperforms the Co_3O_4 NPs@SWCNT (4:1) and Co_3O_4 NPs@SWCNT (6:1) electrodes with capacity values of 358 and 334 mAh g^{-1}, respectively. At low loading of SWCNTs, the Co_3O_4 NPs@SWCNT (6:1) electrode provides the highest capacity in the initial 60 cycles but suffers from severe capacity fading in the extended cycles. Therefore, these results suggest that there is an optimal ratio between Co_3O_4 and SWCNT, with the Co_3O_4 NPs@SWCNT (5:1) heterostructure demonstrating the best battery performance particularly with regard to reversible capacity and prolonged cycling stability. Remarkably, as revealed in Figure 2.3.4f, even at as high as 2000 mA g^{-1}, the optimal Co_3O_4 NPs@SWCNT (5:1) heterostructure still delivers a capacity of 356 mAh g^{-1} after 600 cycles.

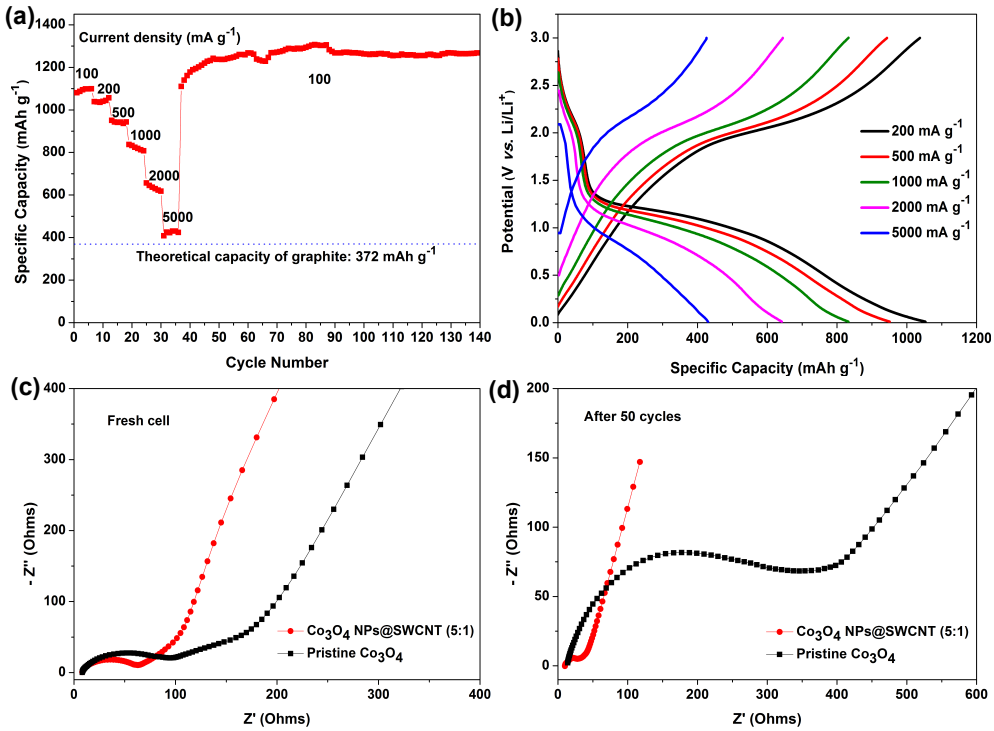

Figure 2.3.5 (a) Rate capability of the optimal Co_3O_4 NPs@SWCNT (5:1) heterostructure electrode tested at different current rates. (b) The corresponding charge/discharge profiles at various current rates. Electrochemical impedance spectra (EIS) of pristine Co_3O_4 and optimal Co_3O_4 NPs@SWCNT (5:1) heterostructure: (c) before cycling (fresh cells) and (d) after 50 cycles at 100 mA g^{-1}.

Notably, the optimal Co_3O_4 NPs@SWCNT (5:1) electrode also demonstrates impressive rate capability. As it can be seen in Figure 2.3.5a, the specific capacities of Co_3O_4 NPs@SWCNT (5:1) are 1080, 1038, 950, 837, and 656 mAh g^{-1} at 100, 200, 500, 1000 and 2000 mA g^{-1}, respectively. When tested at 5000 mA g^{-1}, its capacity can still maintain as high as 425 mAh g^{-1}. Remarkably, when the current rate goes back to 100 mA g^{-1}, the capacity of Co_3O_4 NPs@SWCNT (5:1) can be recovered to 1109 mAh g^{-1} and gradually stabilized at 1267 mAh g^{-1} after 100 extended cycles, indicating its excellent reaction reversibility and cycling stability. Fig. 5b shows its corresponding charge/discharge curves at various current rates.

To further understand the origin of improved cyclic performance and rate capability of the optimal Co_3O_4 NPs@SWCNT (5:1) electrode, electrochemical impedance spectroscopy measurements (EIS) are performed to study the kinetic properties of the electrode materials. Figure 2.3.5c and d show the Nyquist plots of pristine Co_3O_4 and the optimal Co_3O_4 NPs@SWCNT (5:1) anodes before and after 50 cycles at 100 mA g^{-1}. As a result, before cycling test, the Co_3O_4 NPs@SWCNT (5:1) shows a lower charge transfer resistance of ~65 Ω than that of pristine Co_3O_4 (~100 Ω), indicating better charge transport properties at the electrode/electrolyte interface. After 50 cycles, the charge transfer resistance of the Co_3O_4 NPs@SWCNT (5:1) is reduced to only ~40 Ω, much lower than that of pristine Co_3O_4 (~400 Ω), suggesting that the SWCNT sheet matrix can significantly improve its electrical conductivity and mechanical stability, leading to significant enhancement in the overall electrochemical performance in LIBs.

It is worth mentioning that the optimal Co_3O_4 NPs@SWCNT sample in this work displays significantly enhanced electrochemical performance in comparison with most previously reported Co_3O_4-based composites, such as Co_3O_4/graphene, Co_3O_4/CNT and

Co_3O_4/C and other nanostructured Co_3O_4 (including double-shelled hollow spheres, nanofibers, nanosheets, etc.) [22, 39-55]. As shown in Figure 2.3.6a, the reversible capacity of Co_3O_4 NPs@SWCNT is as high as 1286 mAh g^{-1} at 100 mA g^{-1}, significantly outperforming the previously reported results obtained at a current density ranging from 50 to 180 mA g^{-1}. When tested at extremely high current densities of 1000 and 2000 mA g^{-1} for over 200 and 600 cycles, respectively, the high capacity retention of Co_3O_4 NPs@SWCNT can still be achieved. Figure 2.3.6b exhibits the comparison of rate capability in the present work and other recently published reports in literature [22, 46, 48-55]. As we can see that the optimal Co_3O_4 NPs@SWCNT sample also demonstrates superior rate capability compared to previously reported Co_3O_4-based electrode materials for LIBs, further confirming the successful electrode materials design and effective preparation method demonstrated in this work. Such significantly enhanced electrochemical performance, in terms of high reversible capacity, prolonged cycling stability and superior rate performance, can be mainly ascribed to the several aspects. First, the high mass loading of Co_3O_4 in the composites ensures high practical energy density of the entire electrode. Second, the Co_3O_4 nanoparticles offer shorter pathways for lithium ion diffusion, and the flexible, highly conductive SWCNT sheet-like matrix provides continuous fast charge transport pathways. Third, the intimate contact between Co_3O_4 and SWCNT matrix guarantees that the mechanically strong SWCNT sheet-like matrix can effectively suppress the nanoparticles aggregation and facilitate their strain relaxation during long-term cycling.

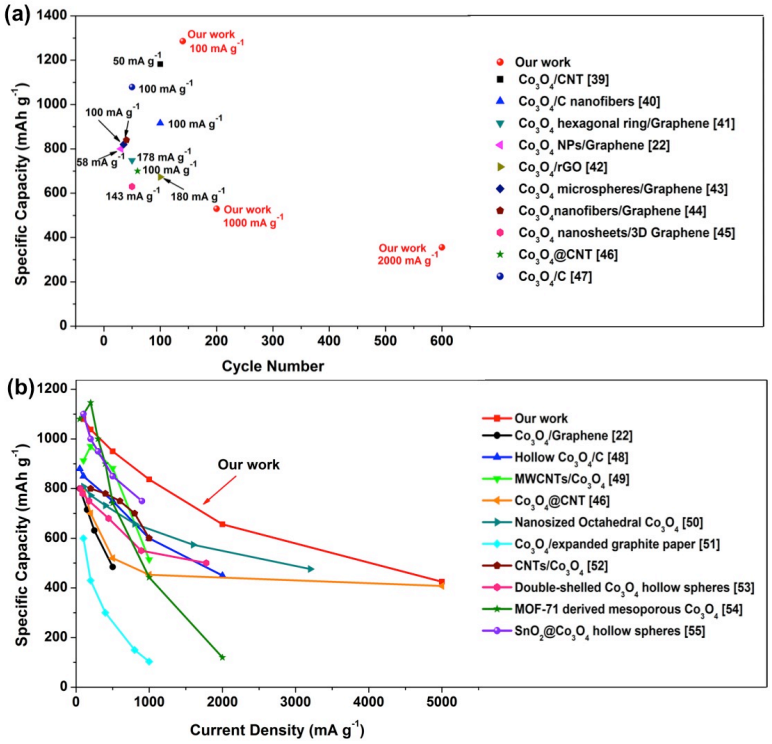

Figure 2.3.6 (a) Comparisons of specific capacity and cycling performance between the optimal Co_3O_4 NPs@SWCNT in our work and previously reported Co_3O_4-carbonaceous composites (including carbon nanotubes, graphene, porous carbon, etc.) (b) Comparisons of rate capability in the present work and other recently published reports in literature.

2.3.4 Conclusions

In conclusion, a facile evaporation-induced self-assembly (EISA) approach has been developed for fabricating a novel Co_3O_4 NPs@SWCNT heterostructure. This approach realizes a uniform dispersion and well confinement of as high as 83 wt% Co_3O_4 NPs within

the SWCNT matrix. The as-prepared Co_3O_4 NPs@SWCNT heterostructure demonstrates extremely high reversible capacity, outstanding cycling performance at various high current rates and superior rate performance. We believe that such a facile self-assembly strategy is not restricted to the Co_3O_4 NPs@SWCNT nanocomposite, which can also be generalized to form various SWCNT-based nanostructures for a wide variety of applications in LIBs, supercapacitors and other fields.

2.3.5 References

[1] B. Wang, X.L. Li, X.F. Zhang, B. Luo, M.H. Jin, M. H. Liang, S.A. Dayeh, S.T. Picraux, L.J. Zhi, Adaptable silicon–carbon nanocables sandwiched between reduced graphene oxide sheets as lithium ion battery anodes, ACS Nano, 2013, 7, 1437-1445.

[2] Y.H. Xu, Q.Liu, Y.J. Zhu, Y.H. Liu, A. Langrock, M.R. Zachariah, C.S. Wang, Uniform nano-Sn/C composite anodes for lithium ion batteries, Nano Lett. 2013, 13, 470-474.

[3] Z.Q. Xie, J.Q. Zhao, Y. Wang, One-step solvothermal synthesis of Sn nanoparticles dispersed in ternary manganese-nickel-cobalt carbonate as superior anode materials for lithium ion batteries, Electrochim. Acta, 2015, 174, 1023-1029.

[4] J.L. C. Rowsell, V. Pralong, L.F. Nazar, Layered lithium iron nitride: A promising anode material for li-ion batteries, J. Am. Chem. Soc. 2001, 123, 8598–8599.

[5] P. Novak, K. Muller, K.S.V. Santhanam, O. Haas, Electrochemically active polymers for rechargeable batteries, Chem. Rev. 1997, 97, 207-281.

[6] Z.S. Wu, W.C. Ren, L. Xu, F. Li, H.M. Cheng, Doped graphene sheets as anode materials with superhigh rate and large capacity for lithium ion batteries, ACS Nano, 2011, 5, 5463-5471.

[7] H.J. Peng, J.Q. Huang, M.Q. Zhao, Q. Zhang, X.B. Cheng, X.Y. Liu, W.Z. Qian, F. Wei, Nanoarchitectured graphene/CNT@porous carbon with extraordinary electrical conductivity and interconnected micro/mesopores for lithium-sulfur batteries, Adv. Funct. Mater. 2014, 24, 2772-2781.

[8] P. Meduri, C. Pendyala, V. Kumar, G.U. Sumanasekera, M.K. Sunkara, Hybrid tin oxide nanowires as stable and high capacity anodes for li-ion batteries, Nano Lett. 2009, 9, 612-616.

[9] Y.S. Hu, L. Kienle, Y.G. Guo, J. Maier, High lithium electroactivity of nanometer-sized rutile TiO_2, Adv. Mater. 2006, 18, 1421-1426.

[10] W.Y. Li, L.N. Xu, J. Chen, Co_3O_4 Nanomaterials in lithium-ion batteries and gas sensors, Adv. Funct. Mater. 2005, 15, 851-857.

[11] W.L. Yao, J. Yang, J.L. Wang, Y. Nuli, Multilayered cobalt oxide platelets for negative electrode material of a lithium-ion battery, J. Electrochem. Soc. 2008, 155, A903-A908.

[12] B. Liu, X.B. Zhang, H. Shioyama, T. Mukai, T. Sakai, Q. Xu, Converting cobalt oxide subunits in cobalt metal-organic framework into agglomerated Co_3O_4 nanoparticles as an electrode material for lithium ion battery, J. Power Sources 2010, 195, 857-861.

[13] Y.G. Li, B. Tan, Y.Y. Wu, Mesoporous Co_3O_4 nanowire arrays for lithium ion batteries with high capacity and rate capability, Nano Lett., 2008, 8, 265-270.

[14] X. Wang, L.J. Yu, X.L. Wu, F.L. Yuan, Y.G. Guo, Y. Ma, J.N. Yao, Synthesis of single-crystalline Co_3O_4 octahedral cages with tunable surface aperture and their lithium storage properties, J. Phys. Chem. C, 2009, 113, 15553-15558.

[15] S.L. Xiong, J.S. Chen, X.W. Lou, H.C. Zeng, Mesoporous Co_3O_4 and CoO@C topotactically transformed from chrysanthemum-like $Co(CO_3)_{0.5}(OH)\cdot 0.11H_2O$ and their lithium-storage properties, Adv. Funct. Mater. 2012, 22, 861-871.

[16] Y. Wang, H.J. Zhang, L. Lu, L.P. Stubbs, C.C. Wong, J.Y. Lin, Designed functional systems from peapod-like Co@Carbon to Co_3O_4@Carbon nanocomposites, ACS Nano, 2010, 4, 4753-4761.

[17] L.J. Zhi, Y.S. Hu, B.E. Hamaoui, X. Wang, I. Lieberwirth, U. Kolb, J. Maier, K. Mîllen, Precursor-controlled formation of novel carbon/metal and carbon/metal oxide nanocomposites, Adv. Mater. 2008, 20, 1727-1731.

[18] F.B. Hao, Z.W. Zhang, L.W. Yin, Co_3O_4/carbon aerogel hybrids as anode materials for lithium-ion batteries with enhanced electrochemical properties, ACS Appl. Mater. Interfaces, 2013, 5, 8337-8344.

[19] L.M. Wang, B. Liu, S.H. Ran, H.T. Huang, X.F. Wang, B. Liang, D. Chen, G.Z. Shen, Nanorod-assembled Co_3O_4 hexapods with enhanced electrochemical performance for lithium-ion batteries, J. Mater. Chem. 2012, 22, 23541-23546.

[20] Y.T. Zhong, X. Wang, K.C. Jiang, J.Y. Zheng, Y.G. Guo, Y. Ma, J.N. Yao, A facile synthesis and lithium storage properties of Co_3O_4–C hybrid core-shell and hollow spheres, J. Mater. Chem. 2011, 21, 17998-18002.

[21] H. Kim, D.H. Seo, S.W. Kim, J. Kim, K. Kang, Highly reversible Co_3O_4/graphene hybrid anode for lithium rechargeable batteries, Carbon, 2011, 49, 326-332.

[22] Z.S. Wu, W.C. Ren, L. Wen, L.B. Gao, J.P. Zhao, Z.P. Chen, G.M. Zhou, F. Li, H.M. Cheng, Graphene anchored with Co_3O_4 nanoparticles as anode of lithium ion batteries with enhanced reversible capacity and cyclic performance, ACS Nano, 2010, 4, 3187-3194.

[23] N. Du, H. Zhang, B.D. Chen, J.B. Wu, X.Y. Ma, Z.H. Liu, Y.Q. Zhang, D.R. Yang, X.H. Huang, J.P. Tu, Porous Co_3O_4 nanotubes derived from $Co_4(CO)_{12}$ clusters on carbon nanotube templates: a highly efficient material for li-battery applications, Adv. Mater. 2007, 19, 4505-4509.

[24] X.F. He, Y. Wu, F. Zhao, J.P. Wang, K.L. Jiang, S.S. Fan, Enhanced rate capabilities of Co_3O_4/Carbon nanotube anodes for lithium ion battery applications, J. Mater. Chem. A, 2013, 1, 11121-11125.

[25] M.W. Xu, F. Wang, Y. Zhang, S. Yang, M.S. Zhao, X.P. Song, Co_3O_4–Carbon nanotube heterostructures with bead-on-string architecture for enhanced lithium storage performance, Nanoscale, 2013, 5, 8067-8072.

[26] C.M. Jiang, A. Saha, C.S. Xiang, C.C. Young, J.M. Tour, M. Pasquali, A.A. Marti, Increased solubility, liquid-crystalline phase, and selective functionalization of single-walled carbon nanotube polyelectrolyte dispersions, ACS Nano, 2013, 7, 4503-4510.

[27] C.S. Yan, G. Chen, X. Zhou, J.X. Sun, C. Lv, Template-based engineering of carbon-doped Co_3O_4 hollow nanofibers as anode materials for lithium-ion batteries, Adv. Funct. Mater., 2016, 26, 1428-1436.

[28] M.S. Dresselhaus, G. Dresselhaus, A. Jorio, A.G. Souza, R. Saito, Raman spectroscopy on isolated single wall carbon nanotubes, Carbon, 2002, 40, 2043-2061.

[29] B. Varghese, T.C. Hoong, Z. Yanwu, M.V. Reddy, B.V.R. Chowdari, A.T.S. Wee, T.B.C. Vincent, C.T. Lim, C.H. Sow, Co_3O_4 Nanostructures with different morphologies and their field-emission properties, Adv. Funct. Mater., 2007, 17, 1932-1939.

[30] B.G. Choi, S.J. Chang, Y.B. Lee, J.S. Bae, H.J. Kim, Y.S. Huh, 3D heterostructured architectures of Co_3O_4 nanoparticles deposited on porous graphene surfaces for high performance of lithium ion batteries, Nanoscale, 2012, 4, 5924-5930.

[31] L. Wang, Y.L. Zheng, X.H. Wang, S.H. Chen, F.G. Xu, L. Zuo, J.F. Wu, L.L. Sun, Z. Li, H.Q. Hou, Y.H. Song, Nitrogen-doped porous carbon/Co_3O_4 nanocomposites as anode materials for lithium-ion batteries, ACS Appl. Mater. Interfaces, 2014, 6, 7117-7125.

[32] F.B. Hao, Z.W. Zhang, L.W. Yin, Co_3O_4/carbon aerogel hybrids as anode materials for lithium-ion batteries with enhanced electrochemical properties, ACS Appl. Mater. Interfaces, 2013, 5, 8337-8344.

[33] X.Y. Lu, H.M. Chan, C.L. Sun, C.M. Tseng, C. Zhao, Interconnected core–shell carbon nanotube–graphene nanoribbon scaffolds for anchoring cobalt oxides as bifunctional electrocatalysts for oxygen evolution and reduction, J. Mater. Chem. A, 2015, 3, 13371-13376.

[34] Q.M. Su, J. Zhang, Y.S. Wu, G.H. Du, Revealing the electrochemical conversion mechanism of porous Co_3O_4 nanoplates in lithium ion battery by in situ transmission electron microscopy, Nano Energy, 2014, 9, 264-272.

[35] L.L. Luo, J.S. Wu, J.M. Xu, V.P. Dravid, Atomic resolution study of reversible conversion reaction in metal oxide electrodes for lithium-ion battery, ACS Nano, 2014, 8, 11560-11566.

[36] P. Poizot, S. Laruelle, S. Grugeon, L. Dupont, J.M. Tarascon, Searching for new anode materials for the li-ion technology: time to deviate from the usual path, J Power Sources, 2001, 97-98, 235-239.

[37] M.R. Gao, X. Cao, Q. Gao, Y.F. Xu, Y.R. Zheng, J. Jiang, S.H. Yu, Nitrogen-doped graphene supported $CoSe_2$ nanobelt composite catalyst for efficient water oxidation, ACS Nano, 2014, 8, 3970-3978.

[38] J. Zhu, L. Bai, Y. Sun, X. Zhang, Q. Li, B. Cao, W. Yan and Y. Xie, Topochemical transformation route to atomically thick Co_3O_4 nanosheets realizing enhanced lithium storage performance, Nanoscale, 2013, 5, 5241-5246.

[39] N. Venugopal, D.J. Lee, Y.J. Lee, Y.K. Sun, Self-assembled hollow mesoporous Co_3O_4 hybrid architectures: a facile synthesis and application in li-ion batteries, J. Mater. Chem. A, 2013, 1, 13164-13170.

[40] Y.L. Tan, Q.M. Gao, C.X. Yang, K. Yang, W.Q. Tian, L.H. Zhu, One-dimensional porous nanofibers of Co_3O_4 on the carbon matrix from human hair with superior lithium ion storage performance, Sci. Rep. 2015, 5, 12382.

[41] C. Nethravathi, C.R. Rajamath, M. Rajamathi, X. Wang, U.K. Gautam, D. Golberg, Y. Bando, Cobalt hydroxide/oxide hexagonal ring-graphene hybrids through chemical etching of metal hydroxide platelets by graphene oxide: energy storage applications, ACS Nano, 2014, 8, 2755-2765.

[42] J.X. Zhu, Y.K. Sharma, Z.Y. Zeng, X.J. Zhang, M. Sirnivasan, S. Mhalsalkar, H. Zhang, H.H. Hng, Q.Y. Yan, Cobalt oxide nanowall arrays on reduced graphene oxide sheets with controlled phase, grain size, and porosity for li-ion battery electrodes, J. Phys. Chem. C, 2011, 115, 8400-8406.

[43] X.L. Yang, K.C. Fan, Y.H. Zhu, J.H. Shen, X. Jiang, P. Zhao, C.Z. Li, Tailored graphene-encapsulated mesoporous Co_3O_4 composite microspheres for high-performance lithium ion batteries, J. Mater. Chem. 2012, 22, 17278-17283.

[44] X.L. Yang, K.C. Fan, Y.H. Zhu, J.H. Shen, X. Jiang, P. Zhao, S.R. Luan, C.Z. Li, Electric papers of graphene-coated Co_3O_4 fibers for high-performance lithium-ion batteries, ACS Appl. Mater. Interfaces, 2013, 5, 997-1002.

[45] H.Y. Sun, Y.G. Liu, Y.L. Yu, M. Ahmad, D. Nan, J. Zhu. Mesoporous Co_3O_4 nanosheets-3D graphene networks hybrid materials for high-performance lithium ion batteries, Electrochim. Acta, 2014, 118, 1-9.

[46] D. Gu, W. Li, F. Wang, H. Bongard, B. Spliethoff, W. Schmidt, C. Weidenthaler, Y.Y. Xia, D.Y. Zhao, F. Schüth, Controllable synthesis of mesoporous peapod-like Co_3O_4@carbon nanotube arrays for high-performance lithium-ion batteries, Angew. Chem. Int. Ed. 2015, 54, 7060-7064.

[47] J. Sun, H.M. Liu, X. Chen, D.G. Evans, W.S. Yang, An oil droplet template method for the synthesis of hierarchical structured Co_3O_4/C anodes for li-ion batteries, Nanoscale, 2013, 5, 7564-7571.

[48] D.L. Wang, Y.C. Yu, J. Wang, W.D. Zhou, H.D. Abruna, Template-free synthesis of hollow-structured Co_3O_4 nanoparticles as high-performance anodes for lithium-ion batteries, ACS Nano, 2015, 9, 1775-1781.

[49] G. Huang, F.F. Zhang, X.C. Du, Y.L. Qin, D.M. Yin, L.M. Wang, Metal organic frameworks route to in situ insertion of multiwalled carbon nanotubes in Co_3O_4 polyhedra as anode materials for lithium-ion batteries, ACS Nano, 2015, 9, 1592-1599.

[50] G.L. Xu, J.T. Li, L. Huang, W.F. Lin, S.G. Sun, Synthesis of Co_3O_4 nano-octahedra enclosed by {111} facets and their excellent lithium storage properties as anode material of lithium ion batteries, Nano Energy, 2013, 2, 394-402.

[51] Y. Zhao, C.L. Ma, Y. Li, H.L. Chen, Z.P. Shao, Self-adhesive Co_3O_4/expanded graphite paper as high-performance flexible anode for Li-ion batteries, Carbon, 2015, 95, 494-496.

[52] L.H. Zhuo, Y.Q. Wu, J. Ming, L.Y. Wang, Y.C. Yu, X.B. Zhang, F.Y. Zhao, Facile synthesis of a Co_3O_4–carbon nanotube composite and its superior performance as an anode material for Li-ion batteries, J. Mater. Chem. A, 2013, 1, 1141-1147.

[53] X. Wang, X.L. Wu, Y.G. Guo, Y.T. Zhong, X.Q. Cao, Y. Ma, J.N. Yao, Synthesis and lithium storage properties of Co_3O_4 nanosheet-assembled multishelled hollow spheres, Adv. Funct. Mater. 2010, 20, 1680-1686.

[54] C. Li, T.Q. Chen, W.J. Xu, X.B. Lou, L.K. Pan, Q. Chen, B.W. Hu, Mesoporous nanostructured Co_3O_4 derived from MOF template: a high-performance anode material for lithium-ion batteries, J. Mater. Chem. A, 2015, 3, 5585-5591.

[55] W.S. Kim, Y. Hwa, H.C. Kim, J.H. Choi, H.J. Sohn, S.H. Hong, SnO_2@Co_3O_4 hollow nanospheres for a Li-ion battery anode with extraordinary performance, Nano Res. 2014, 7, 1128-1136.

CHAPTER 3. METAL-ORGANIC FRAMEWORK DERIVED CONI EMBEDDED CARBON NANOCAGES FOR EFFICIENT DYE-SENSITIZED SOLAR CELLS*

3.1 Introduction

Dye-sensitized solar cells (DSSCs) have become one of the most promising photovoltaic devices for efficient conversion of solar energy into electricity, owing to their environmental friendliness and easy fabrication [1, 2]. DSSCs mainly consist of three crucial components: a photoanode, a counter electrode (CE) and an electrolyte containing iodide-triiodide (I^-/I_3^-) redox shuttle [3]. Among them, the CEs play a key role in governing the power conversion efficiency (PCE) since they mainly transfer electrons from the external circuit and perform electrocatalytic reduction of the redox couples [4]. Therefore, as an ideal CE, it should possess promising characteristics, such as excellent electrical conductivity, high electrocatalytic activity and low cost [5]. At present, platinum (Pt) has been widely employed as a high-performance CE for DSSCs since it could satisfy most of the above-mentioned characteristics. Nevertheless, Pt is highly expensive and extremely scarce, thereby severely impeding large-scale fabrication of DSSCs for practical commercialization. In addition, the DSSCs based on Pt as CE materials still show unsatisfactory long-term operation stability mainly due to the corrosive iodide/triiodide redox electrolyte [6]. To overcome the aforementioned challenges, it is always desirable to explore new alternatives to replace Pt as efficient and low-cost CEs for DSSCs. To date, various Pt-free CEs based on conducting polymers [7, 8], carbon materials (carbon black [9], graphene [10, 11], carbon nanotubes [12, 13] etc.) and transition metal compounds (selenides [14, 15], sulfides [16, 17], nitrides [18], oxides [19, 20, 21], carbides [22], alloys [5, 25, 26] etc.) have been reported. Unfortunately, these materials are either limited by their low electrical conductivities or poor electrocatalytic activities. Their performances are still not comparable with the Pt, and most of the reported DSSCs have PCEs generally lower than 7.5 % [23, 24]. In addition, the stability of most new Pt-free CEs remains largely unknown.

Metal-organic frameworks (MOFs), built from metal ions/clusters as nodes and organic linkers as struts, have attracted more and more interest in recent years owing to their high surface area, large pore volume and diverse structures [32, 33]. Inspired by these properties, I proposed to apply Co-based ZIF-67 as a suitable precursor to synthesize cobalt sufide embedded carbon nanocages to improve the electric conductivity of the entire counter electrode and also reduce the aggregation of CoS_2 nanoparticles. To synthesize CoS_2 embedded carbon nanocages, the as-prepared ZIF-67 crystals were transferred into a beaker containing 0.1 M thioacetamide (TAA), 150 mL anhydrous ethanol, and 150 μL distilled water. Then the mixture was heated at 90 °C for different time length. Afterwards, the samples were annealed in N_2 at 450 °C for 1 hour. The sulfurizing time significantly affects the structure and composition of CoS_2. After sulfurization, uniform hollow spheres with ultra-thin walls were formed. By subsequent thermal annealing in N_2, these hollow spheres are transformed into porous nanocages. It is noticed that the wall thickness of nanocages is very thin, however, they still maintain a great thermal stability without showing apparent morphology change during annealing at high temperature. The DSSC PCE is maximized to 8.20%, which is slightly higher than that of Pt-based DSSC (7.88%). However, its

* Reprinted with permission from Zhiqiang Xie, Xiaodan Cui, Wangwang Xu, and Ying Wang, Metal-organic framework derived CoNi@CNTs embedded carbon nanocages for efficient dye-sensitized solar cells. Electrochim. Acta, 2017, 229, 361-370. Copyright 2017 Elsevier.

electrochemical stability is still unsatisfactory for practical application in DSSCs.

To further improve the PCE and electrochemical stability of MOF-derived CEs, a material with a more robust nanostructure and more active catalytic sites are highly desired. Compared to sulfides-based CEs, metal alloy nanoparticles are more environmental friendly and have emerged as new candidates for CE in DSSCs, however, the preparation of metal alloy/carbon nanostructures by using bimetallic MOFs as the single precursor has rarely been reported [32,33]. In comparison with other synthesis methods of alloy nanoparticles, one-step pyrolysis of bimetallic MOFs offers a new route to prepare well-dispersed alloy nanoparticles embedded conductive carbon matrix without using any surfactants or toxic reducing agent. The chemical composition and particle size of alloy can also be optimized by simply varying the mixed metal ions ratio during the synthesis.

In this chapter, novel CoNi alloy@carbon nanotubes embedded carbon nanocages (CoNi@CNTs-C) have been successfully prepared, through one-step pyrolysis of Co/Ni bimetallic metal organic framework (MOF) in Ar atmosphere. Within such MOF-derived nanostructure, the CoNi alloy nanoparticles offer numerous active sites to efficiently catalyze the redox reactions, and meanwhile the CNTs and carbon nanocages serve as conductive network, which can prevent CoNi nanoparticles from aggregation and reduce corrosion by acidic electrolyte. As demonstrated in various electrochemical measurements, the optimal CoNi@CNTs-C-200 CE demonstrates the highest PCE and current density of 9.04% and 18.3 mA/cm^2, respectively, which are significantly higher than 7.88% and 15.0 mA/cm^2 from the DSSC based on Pt CE. More importantly, the CoNi@CNTs-C-200 CE also exhibits much better electrochemical stability than conventional Pt CE during long-term electrochemical cycling, which is crucial for practical application in high-performance DSSCs.

3.2 Experimental

Preparation of Co-C and CoNi@CNTs-C

In brief, 2 g cobalt nitrate hexahydrate and 3.06 g 2-methylimidazole were separately dissolved in 100 mL methanol, respectively. Afterwards, the two solutions were mixed under stirring for 10 min and aged for 24 h at room temperature. The resultant purple solid was collected from the solution by centrifugation at 4000 rpm for 10 min and then washed with methanol at least three times. After washing, the zeolitic imidazolate framework-67 (ZIF-67) powders were dried overnight at 80 °C . Afterwards, cobalt nanoparticles embedded within N-doped carbon nanocages (Co-C) were prepared by a facile calcination of ZIF-67 nanocrystals at 900 °C for 2 hours in Ar atmosphere.

When introducing different amounts of nickel nitrate hexahydrate (100, 200, 400 mg, respectively) into the above synthesis of ZIF-67, Ni^{2+} incorporated ZIF-67 powders were synthesized and then transformed to CoNi@CNTs-C by a direct pyrolysis at 900 °C for 2 hours in Ar atmosphere. For convenience, the as-prepared CoNi@CNTs-C samples were labeled as CoNi@CNTs-C-100, CoNi@CNTs-C-200 and CoNi@CNTs-C-400, respectively.

Electrodes preparation

The photoanodes and counter electrodes for DSSCs were fabricated according to our previous reports. In brief, for the preparation of the counter electrodes in DSSCs, 0.2 g of the as-synthesized products were well dispersed in ethanol (2mL) by continuously magnetic stirring. Subsequently, the solutions of terpineol (0.86 mL) and ethyl celluloses (1.1 mL) in ethanol solvent were dipped into the above mixed solution, respectively, followed by sonication and continuous stirring. Afterwards, the resulted slurry was uniformly coated onto

the FTO coated glass (7 Ω/sq Sigma-Aldrich) by simply spin coating method at 4000 rpm for 30 s. Afterwards, the annealing treatment of electrodes was carried out at 450 °C for a half hour in argon atmosphere. For comparison purpose, Pt counter electrodes were also prepared by following the standard preparation method: drop casting 0.5 mM H_2PtCl_6/isopropanol solution onto the FTO coated glass, followed by post-treatment at 450 °C for 20 min in air.

For the preparation of photoanodes in DSSCs, 1 g TiO_2 nanoparticles with the size of 25 nm (Sigma Aldrich 99.7%) were well dispersed in ethanol (8mL), terpineol (4.3 mL) and ethyl celluloses (5.5 mL) in ethanol (10 wt%). Afterwards, the above mixed solution was concentrating down at 70 °C due to the gradual solvent evaporation. Subsequently, the as-obtained slurry was applied to the FTO coated glass through the doctor's blade method. Then, the heat treatment of photoanodes was performed at 125 °C for 6 min in air, 325 °C for 5 min, 375 °C for 5 min, 450 °C for 15 min and 500 °C for 15 min sequentially and then the photoanodes cool down to the room temperature. Afterwards, the TiO_2 photoanodes were soaked in anhydrous ethanol solution containing 0.2 mM N719 dye (Ru[LL'-(NCS)2], L = 2,2'-bipyridyl-4,4'-dicarboxylic acid, L'=2,2'-bipyridyl-4,4'-ditetrabutyl-ammonium carboxylate, Solaronix Co.) and dye-sensitized for 24 h at room temperature.

DSSC fabrication

Typically, the counter electrode and the dye-sensitized TiO_2 photoanode were sandwiched together with the hot-melt sealing film as the spacer (100 μm in thickness). Afterwards, the electrolyte containing 0.1 M GTC (guanidine thiocyanate) in a mixture of acetonitrile and valeronitrile (85:15 vol/vol) (No. ES-0004, IoLiTec Inc., Germany) was injected into the DSSC devices.

Characterizations and measurements

The crystalline structures of as-obtained products were identified by using X-ray diffraction (XRD) technique, and the data were recorded at a constant scanning rate of 2 ^{o}/min on a Rigaku MiniFlex X-ray diffractometer (Cu Kα radiation). The microstructures and morphologies of samples were characterized by using scanning electron microscope (SEM) and high-resolution transmission electron microscope (HRTEM). The SEM imaging and elemental mapping were carried out on a FEI Quanta 3D FEG FIB/SEM with energy-dispersive X-ray spectroscopy (EDS) equipped. TEM and HRTEM imaging was conducted on a JEOL JEM-2010 microscope at 200 kV.

The typical current-voltage (J-V) performance of DSSCs was measured by using a Keithley 2400 source meter, which has a solar light simulator (model: 67005, Oriel) to simulate sunlight under one sun illumination (100 mW/cm^2). A series of electrochemical measurements were also carried out, including the cyclic voltammetry (CV), electrochemical impedance spectroscopy (EIS) and Tafel polarization. The CV measurements were performed at a scan rate of 20 mV/s by using an electrochemical workstation (CHI 6504C). Specifically, for the CV measurements, an Hg/Hg^+ electrode works as reference electrode, the as-fabricated counter electrode acts as working electrode and a Pt foil works as auxiliary electrode. The total exposure area of the counter electrode in an acetonitrile solution containing 0.1 M $LiClO_4$, 10 mM LiI and 1 mM I_2 is 1.5 cm^2. The EIS and Tafel polarization measurements were carried out using an electrochemical work station (CHI 6504C). In brief, the EIS measurements were conducted by using an applied voltage aptitude of 10 mV and bias voltage 0 V in the frequency range from 10^5 Hz to 0.01 Hz. The Tafel data were collected in the voltage range of 1 V to -1 V.

3.3 Results and Discussion

The overall synthesis of MOF-derived CoNi@CNTs-C nanostructures involves two steps. Firstly, the Co/Ni bimetallic metal organic frameworks (MOFs) are synthesized using various ratio of Co^{2+}/Ni^{2+} and 2-methylimidazole at room temperature. During the following pyrolysis process at 900 °C for 2 h, Co^{2+} and Ni^{2+} are simultaneously reduced into metallic Co and Ni by the resultant carbon from the decomposition of organic linkers and meanwhile metallic Co and Ni undergo the alloying reaction to form CoNi alloy nanoparticles. The resultant CoNi alloy can subsequently function as catalysts to promote the formation of CNTs. In this process, bimetallic MOFs act not only as the carbon source for the formation of carbon nanotubes with the assistance of CoNi alloy catalysts, but also as a sacrificial template for the nanocage-like framework. Specifically, the carbon nanocages are formed by annealing the as-prepared MOF particles as the template at 900 °C in inert gas, in which the organic ligands 2-Methylimidazole ($C_4H_6N_2$) containing rich nitrogen content serve as the carbon source. During the annealing treatment, the organic ligands within the polyhedron-like MOFs will decompose and transform into the N-doped carbon matrix, retaining a similar morphology with the MOF template. This formation process of N-doped carbon matrix using MOFs as the template/precursor has been confirmed by our early work [39] and other previous reports [29, 30]. Finally, we obtained the CoNi@CNTs-C with a unique nanostructure, whereas CoNi alloy nanoparticles are well encapsulated into the CNTs (CoNi@CNTs), and the CoNi@CNTs are completely embedded into carbon nanocages. It is worth mentioning that the synthesis process of CoNi nanoparticles embedded carbon nanocages is facile and scalable, since we simply use MOFs as the template and precursors during the whole synthesis process. It does not require complex procedures or precise control of reaction conditions such as pH and concentration of the solutions.

To identify the crystalline structures and phases of the MOF-derived CoNi@CNTs-C samples, the powder X-ray diffraction (XRD) measurements are first performed. The XRD results show that all the CoNi@CNTs-C samples are composed of graphitic carbon and face-centered cubic (fcc) CoNi alloy (Figure 3.1a). It is clearly observed that the strongest (111) reflection peak positions of all samples lie between the peak position of pure Co (JCPDS# 15-0806) and pure Ni (JCPDS# 04-0850) (Figure 3.1b), which is well consistent with previously reported CoNi alloys. The main (111) peaks of CoNi@CNTs-C samples obviously shift to higher angles with the increase of Ni^{2+} amounts during the synthesis, further confirming the formation of CoNi alloys. No other impurities or phases are observed, implying a complete transformation of Ni^{2+} incorporated ZIF-67 to CoNi@CNTs-C. In addition, the sharp peaks in the XRD spectra of the CoNi alloy indicate that the samples are highly crystalline.

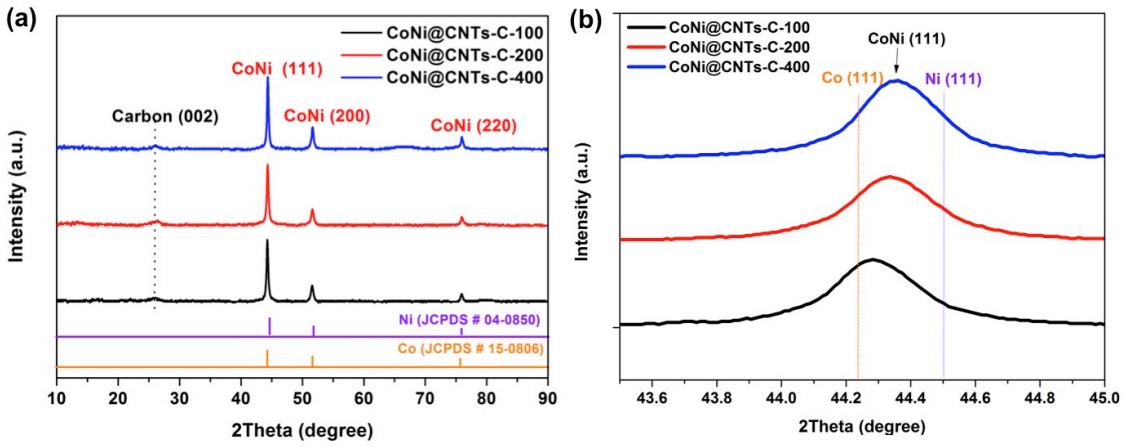

Figure 3.1 (a) XRD patterns and (b) Selected enlarged portion of CoNi@CNTs-C-100, CoNi@CNTs-C-200 and CoNi@CNTs-C-400 samples in comparison with standard XRD peaks of pure Co and Ni.

Scanning electron microscopy (SEM) images show that ZIF-67 samples are composed of polyhedron-like particles with smooth surfaces. However, after one-step pyrolysis process in inert gas atmosphere, the as-synthesized CoNi@CNTs-C-100 and CoNi@CNTs-C-200 samples consist of polyhedron-like carbon nanocages (200~500 nm) with CoNi alloy nanoparticles well embedded (Figure 3.2a-d). However, some of the carbon nanocages in CoNi@CNTs-C-400 sample are broken and one can notice that relatively larger CoNi alloy particles are located outside the carbon nanocages (Figure 3.2e-f). This observation indicates that the Ni amount plays a crucial role in control of the particle size of CoNi alloy and thus might affect structural stability of CoNi@CNTs-C samples in acidic electrolyte when applied as CEs for DSSCs.

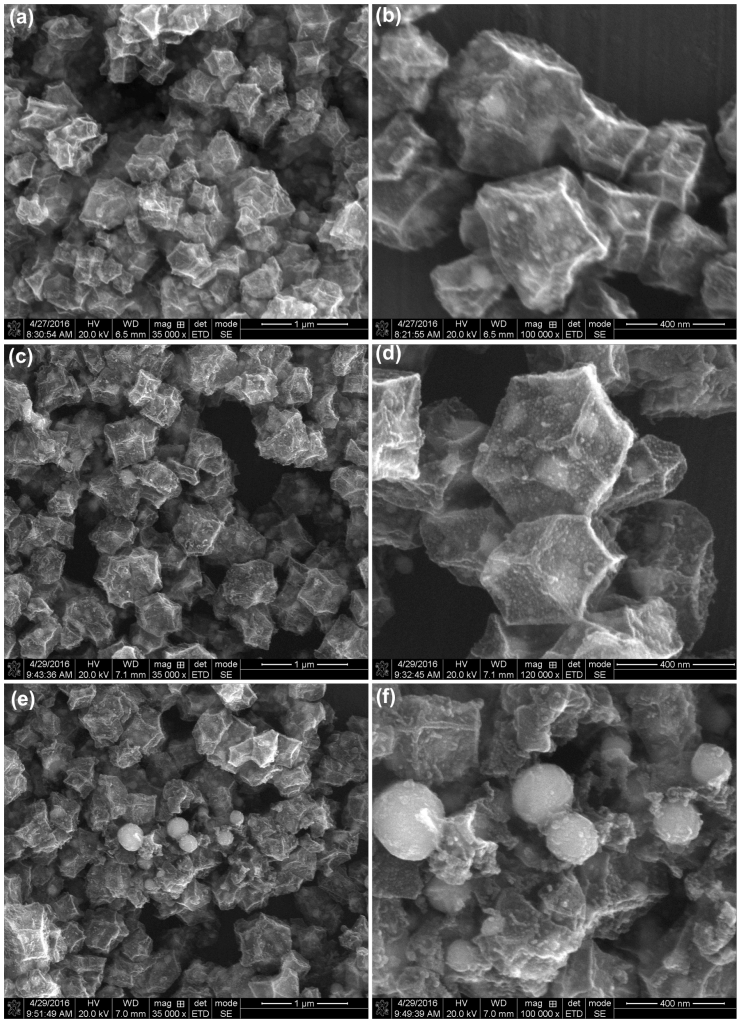

Figure 3.2 SEM images of (a, b) CoNi@CNTs-C-100, (c, d) CoNi@CNTs-C-200 and (e, f) CoNi@CNTs-C-400.

Experiments presented further in the work show that DSSC based on the CoNi@CNTs-C-200 CE demonstrates the highest energy conversion efficiency, and therefore we perform a detailed transmission electron microscopy (TEM) and high resolution (HR) TEM to better understand its microstructure and nanostructure, as displayed in Figure 3.3a-d. It can be clearly observed that the CoNi@CNTs-C-200 sample is composed of numerous CoNi alloy nanoparticles with the size of 20 ~ 100 nm (dark dots), which are well

confined in the carbon nanocages (grey framework). Interestingly, one can observe that some short CNTs (marked by red arrow in Figure 3.3b) protrude from the surface of carbon nanocages. Further HRTEM images display that individual CoNi alloy nanoparticle is completely enwrapped by CNTs (Figure 3.3c, d), and the distinct lattice fringe with the measured d-spacing of 0.21 nm can be assigned to the (111) plane of CoNi alloy. It is believed that metal alloy possesses better catalytic activity for CNTs growth than single metal catalysts, and thus leads to the formation and protrusion of CNTs during pyrolysis of Ni^{2+} incorporated ZIF-67 at high temperature in Ar atmosphere.

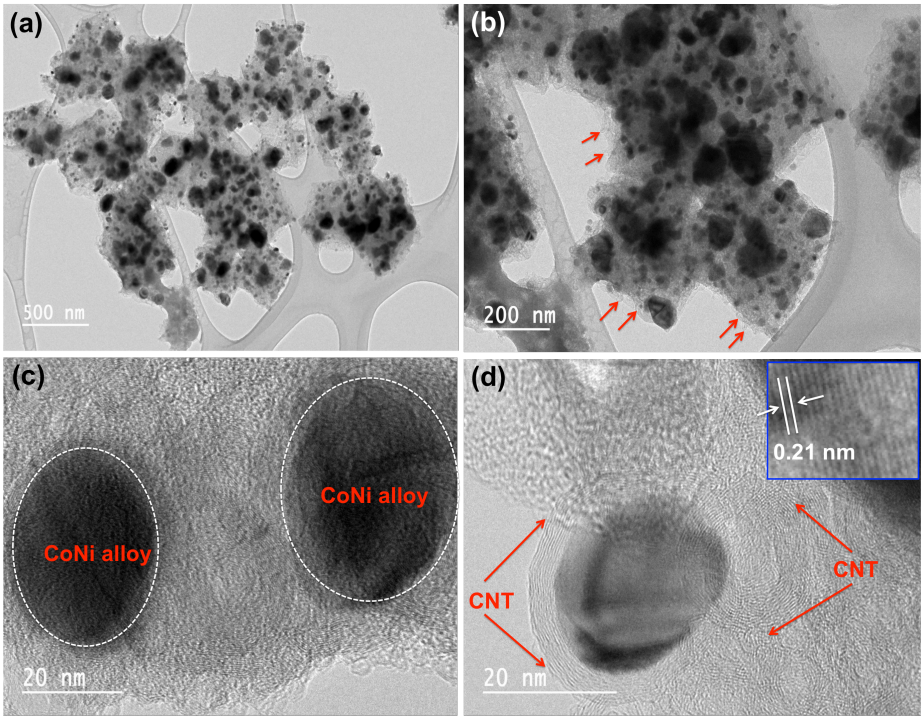

Figure 3.3 (a, b) TEM images and (c, d) HRTEM images of CoNi@CNTs-C-200 (optimal sample).

The corresponding energy-dispersive X-ray (EDS) mapping results further confirm the coexistence of C, N, Co and Ni elements within the sample, and both the Co and Ni elements show homogeneous distribution for all the nanoparticles (Figure 3.4), confirming the CoNi alloy phase, which are well consistent with previous XRD and TEM results. It has been reported that proper alloying of transition metals is favorable for electronic perturbation of single metals, and thus the alloy such as CoNi usually demonstrates better catalytic activity than pure Co and Ni catalysts. In addition, nitrogen doping has been proved effective in enhancing catalytic activity and electrical conductivity of carbon materials. Therefore, we believe that CoNi@CNTs-C-200 could be a promising CE material for new-generation DSSCs. It is also worth noting that chemical composition of the as-prepared CoNi alloy in our work can be easily tuned by varying the weight ratio of cobalt and nickel precursors during the synthesis of Ni^{2+} incorporated ZIF-67 nanocrystals. The atomic ratio of Co/Ni in the optimal sample CoNi@CNTs-C-200 is found to be 9:1 through EDS mapping results, indicating a certain amount of Ni ions can be encapsulated within ZIF-67 nanocrystals during the synthesis process in methanol at room temperature.

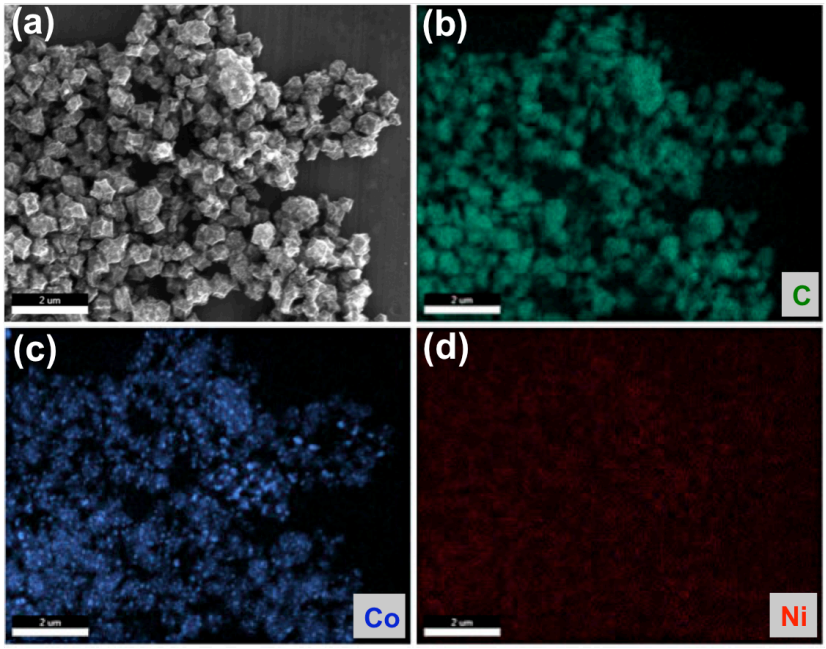

Figure 3.4 (a) SEM image of CoNi@CNTs-C-200 (optimal sample) and its corresponding EDS elemental mapping of (b) C, (c) Co and (d) Ni, respectively.

Thanks to such a unique hierarchical nanostructure composed of CoNi@CNTs within the carbon nanocages, the as-prepared CoNi@CNTs-C composites are explored as counter electrode materials for DSSCs for the first time. The classic assembly of a DSSC device is shown in Figure 3.5a, which is mainly composed of TiO_2 photoanode with N719 dye, I_3^-/I^- redox electrolyte and CoNi@CNTs-C counter electrode. Figure 3.5b displays representative *J-V* curves of DSSCs with Pt, CoNi@CNTs-C-100, CoNi@CNTs-C-200, CoNi@CNTs-C-400 and Co-C as CEs, measured under a light intensity of 100 mW/cm^2. The corresponding photovoltaic performances are summarized in Table 3.1. It is found that the corresponding PCEs of these DSSCs are in the order of CoNi@CNTs-C-400 < Co-C < Pt < CoNi@CNTs-C-100 < CoNi@CNTs-C-200. Notably, the DSSC with conventional Pt as CE yields PCE=7.88%, J_{sc}=15.0 mA/cm^2 and V_{oc}=0.73 V, while the one with CoNi@CNTs-C-200 as CE demonstrates much higher photovoltaic parameters with PCE=9.04%, J_{sc}=18.30 mA/cm^2 and V_{oc}=0.76 V, showing ~15% overall PCE enhancement compared to the Pt counterpart. Such remarkable PCE from the DSSC consisting of CoNi@CNTs-C-200 demonstrates an ideal Pt-free CE for next-generation DSSCs.

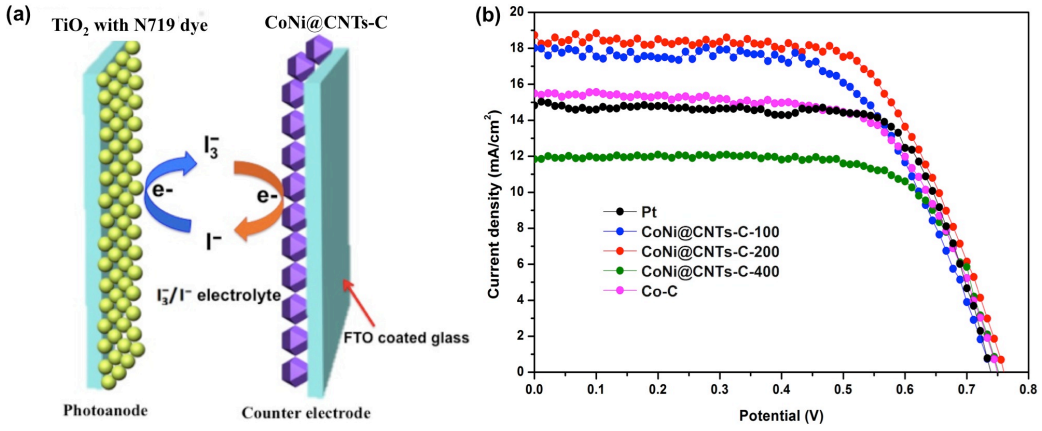

Figure 3.5 (a) Scheme of a DSSC configuration using CoNi@CNTs-C as the counter electrode. (b) Photocurrent density-voltage (*J-V*) curves of DSSCs with Pt, CoNi@CNTs-C-100, CoNi@CNTs-C-200, CoNi@CNTs-C-400 and Co-C, measured under a light intensity of 100 mW/cm^2.

Table 3.1 Photovoltaic performance of DSSCs with various CEs

Samples	J_{sc} (mA/cm^2)	V_{oc} (V)	FF	η (%)
Co-C	15.5	0.75	0.66	7.63
CoNi@CNTs-C-100	18.0	0.73	0.62	8.10
CoNi@CNTs-C-200	18.3	0.76	0.65	9.04
CoNi@CNTs-C-400	11.8	0.75	0.72	6.36
Pt	15.0	0.73	0.72	7.88

To scrutinize the remarkable difference in photovoltaic performances of these DSSCs, a series of electrochemical measurements are carried out, including cyclic voltammetry (CV), electrochemical impedance spectroscopy (EIS) and Tafel polarization. Figure 3.6 displays CV curves of different CEs based on Pt, CoNi@CNTs-C-100, CoNi@CNTs-C-200, CoNi@CNTs-C-400 and Co-NC, recorded at a scan rate of 20 mV/s in acetonitrile solution containing 10.0 mM LiI, 1.0 mM I_2 and 0.1 M $LiClO_4$. Two pairs of oxidation/reduction peaks (Ox-1/Red-1, Ox-2/Red-2) can be observed for the CV curves of all the CEs, which can be assigned to the following reaction (1) and (2), respectively[*].

$$I_3^- + 2e \rightarrow 3I^- \quad (1)$$

$$3I_2 + 2e \rightarrow 2I_3^- \quad (2)$$

The characteristics of Ox-1/Red-1 pair are our focus of analysis as the CEs mainly perform electrocatalytic reduction of the redox couples (I_3^-/I^-). The second redox peak in the CV curve is attributed to the reduction of molecular iodine (I_2). In general, the peak-to-peak separation (E_{pp}) and peak current density are utilized to study catalytic activities of CEs in DSSCs. The small E_{pp} and high peak current density are two crucial indicators for high electrocatalytic activity. Close examination shows that the E_{pp} value of the CoNi@CNTs-C-200 CE is only 267 mV, which is much smaller than that of conventional Pt CE (320 mV). In addition, the E_{pp} values of all the CEs are in the order of CoNi@CNTs-C-200 < CoNi@CNTs-C-100 < Pt < Co-C < CoNi@CNTs-C-400, while the corresponding peak current densities are in the reversed order: CoNi@CNTs-C-200 > CoNi@CNTs-C-100 > Pt > Co-C > CoNi@CNTs-C-400. Therefore, the above results indicate that CoNi@CNTs-C-200 and CoNi@CNTs-C-100 demonstrate superior electrocatalytic activities compared to other CEs. The large differences in electrocatalytic activities of three CoNi@CNTs-Cs are likely ascribed to the different chemical composition and particle size of alloy. As observed from SEM images in Figure 3.2, the particle size of alloy in CoNi@CNTs-C-400 is much larger than CoNi@CNTs-C-100 and CoNi@CNTs-C-200, thereby reducing the surface area and active sites for catalytic reaction. In addition, the breakage of carbon nanocages in CoNi@CNTs-C-400 sample may lead to poor chemical stability CoNi alloy in acidic electrolyte compared to the other two CoNi@CNTs-C samples. Therefore, CNTs-C-400 demonstrates the worst electrocatalytic activities. It is also found that both CoNi@CNTs-C-100 and CoNi@CNTs-C-200 display better electrocatalytic activities than Co-C, indicating the superiority of alloy compared to single metal catalysts.

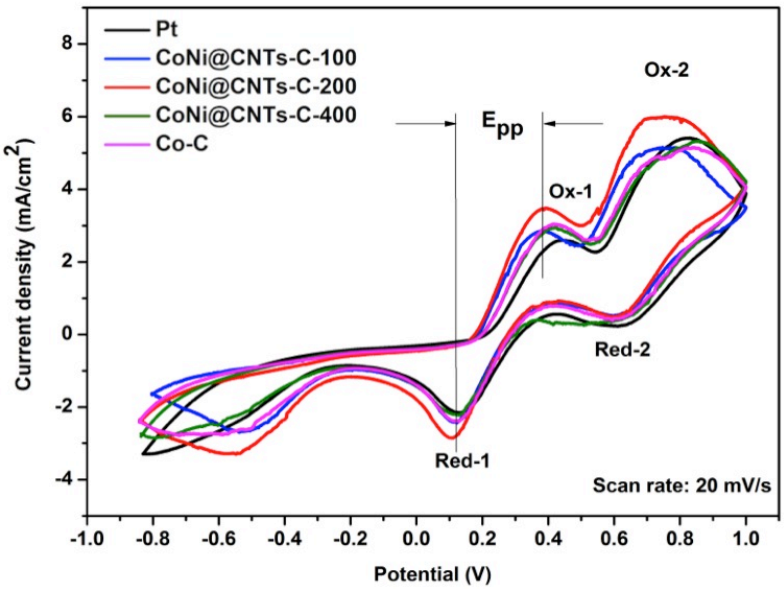

Figure 3.6 Cyclic voltammetry (CV) curves of the CEs with Pt, CoNi@CNTs-C-100, CoNi@CNTs-C-200, CoNi@CNTs-C-400 and Co-C obtained at a scan rate of 20 mV/s in acetonitrile solution containing 10.0 mM LiI, 1.0 mM I_2 and 0.1 M $LiClO_4$.

To further elucidate the catalytic activity differences of all the CEs, electrochemical impedance spectroscopy (EIS) measurements are also carried out to study intrinsic charge transfer and transport properties by using symmetrical dummy cells. The EIS spectra (Nyquist plots) obtained from varied CEs are shown in Figure 3.7a. It can be seen that Nyquist plots are composed of two semicircles in different frequency ranges. The first semicircle (left) in the high-frequency range corresponds to the interfacial charge transfer resistance (R_{ct}) between the electrode and electrolyte. The second semicircle (right) in the low-frequency range indicates the well-known Nernst mass diffusion impedance (Z_N) within the electrolyte. According to previous reports, smaller R_{ct} and Z_N usually indicate higher catalytic activity and faster mass diffusion of CEs within the electrolyte, respectively. The overall series resistances (R_s) of symmetrical dummy cells fabricated with varied CEs is also considered, which is generally attributed to the sum of resistance of FTO substrate, CE materials as well as electric contact. The Nyquist plots are also fitted with an equivalent circuit inset in the Figure 3.7a. By comparison, it is found that both R_{ct} and Z_N of CoNi@CNTs-C-200 are smaller than other CEs, indicating the best catalytic activity among all the CEs, which is in good accordance with the CV observation. It has been widely reported that pristine carbon materials or single Co or Ni metallic nanoparticles usually demonstrate limited available catalytic active sites, thereby resulting in unsatisfactory power conversion efficiency of DSSC devices. However, our work shows that CoNi alloy nanoparticles enwrapped by CNTs within the unique carbon nanocages can efficiently promote the charge transfer from metallic nanoparticles to the 3D conductive carbon frameworks, which may reduce the surface work function of carbon framework, thereby improving catalytic activity of carbon nanocages. It is also demonstrated that CoNi alloy with proper chemical composition demonstrates obviously enhanced catalytic activity than bare metallic Co, which is well consistent with previous report. Therefore, chemical composition of CoNi alloy plays a crucial role in the catalytic activity of a CE.

Tafel polarization is another powerful technique, which is usually utilized to investigate catalytic activity of varied CEs for DSSCs. Therefore, the Tafel polarization

curves of all the CEs are obtained by using the symmetrical dummy cells, as displayed in Figure 3.7b. It is clearly observed that the slopes of both the cathodic and anodic branches of CEs are in the order of CoNi@CNTs-C-200 > CoNi@CNTs-C-100 > Pt > Co-C > CoNi@CNTs-C-400. This result suggests that CoNi@CNTs-C-200 exhibits the highest exchange current density (J_0), indicating the best catalytic activity among all the CEs.

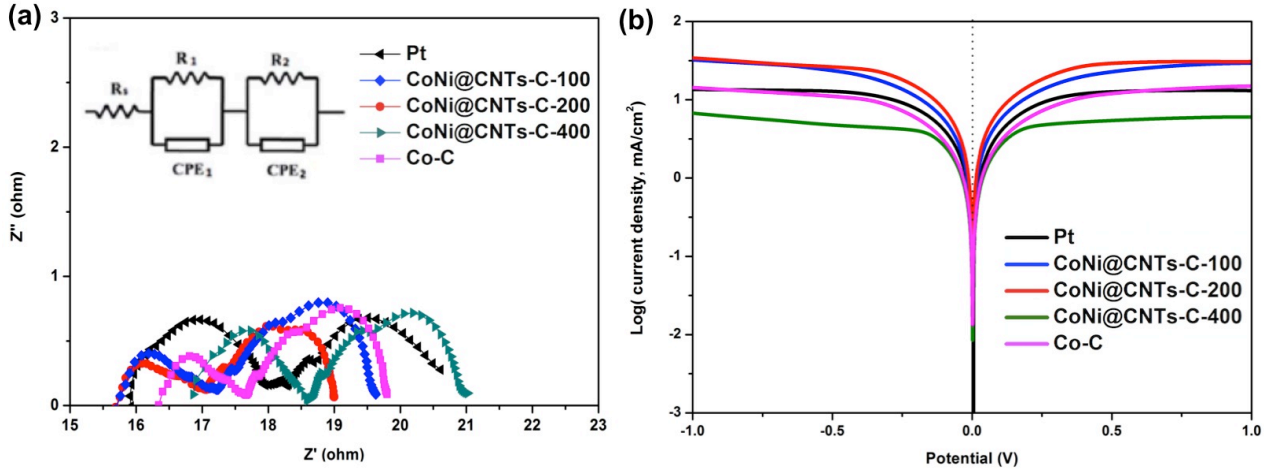

Figure 3.7 (a) Nyquist plots for symmetric cells fabricated with aforementioned samples. (b) The corresponding Tafel polarization curves of symmetric cells.

Taking the above results of CV, EIS and Tafel polarization into consideration, CoNi@CNTs-C-200 demonstrates the best catalytic activity among all the CEs. Therefore, compared to the other CEs including conventional Pt, the DSSC based on CoNi@CNTs-C-200 CE exhibits the highest PCE of 9.04%, J_{sc} of 18.3 mA/cm^2, and a moderate fill factor (FF) of 0.65, proving as a very promising Pt-free CE for application in DSSCs. Notably, among iodine-mediated DSSCs using carbon materials and transition metal compounds, the DSSC based on such unique hybrid of CoNi alloy and N-doped carbon network (CoNi@CNTs-C-200) delivers the highest PCE and J_{sc}.

To further explore practical application of CoNi@CNTs-C-200 as an alternative Pt-free CE for new-generation DSSCs, its electrochemical stability is another crucial factor and needs to be seriously considered. Therefore, we fabricate symmetrical cells using CoNi@CNTs-C-200 and Pt photo-electrode, respectively, and test them for over 300 electrochemical cycles via CV characterization at a scan rate of 50 mV/s (Figure 3.8). It is found that both E_{pp} value and current density of CoNi@CNTs-C-200 show subtle change, however, the Pt CE displays obvious reduction of peak current density and increased E_{pp}. Therefore, CoNi@CNTs-C-200 demonstrates outstanding electrochemical stability compared to commonly used Pt for DSSCs. The excellent stability could be ascribed to the unique hybrid structure of CoNi alloy and N-doped carbon framework, whereas both CNTs and carbon framework can efficiently protect the embedded CoNi alloy nanoparticles from corrosion in the acidic electrolyte during long-term operation.

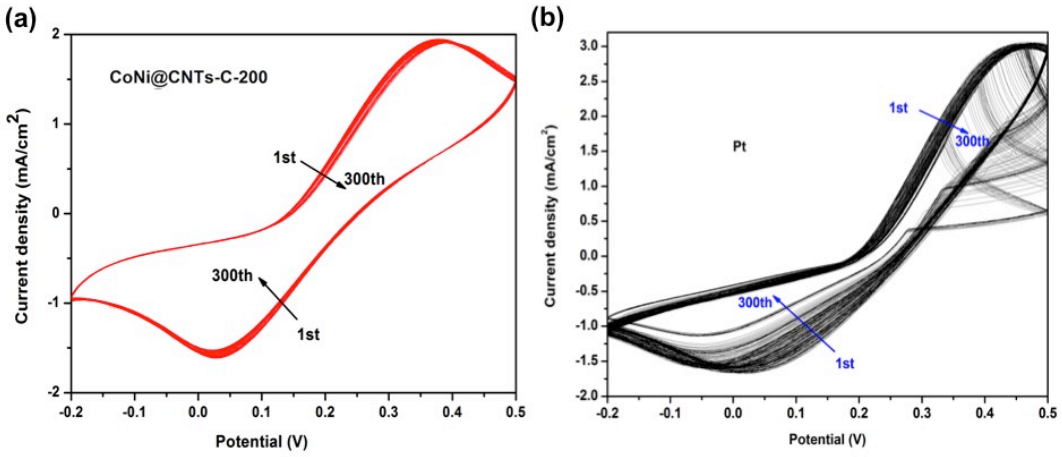

Figure 3.8 CV curves of the CEs based on (a) CoNi@CNTs-C-200 and (b) conventional Pt for 300 cycles. The CV curves are recorded at a scan rate of 50 mV/s in acetonitrile solution containing 10.0 mM LiI, 1.0 mM I_2 and 0.1 M $LiClO_4$.

3.4 Conclusions

In summary, we report, for the first time, a facile synthesis of CoNi alloy@CNTs within carbon nanocages by direct pyrolysis of Ni^{2+} incorporated ZIF-67 in inert gas atmosphere. It is found that the CoNi@CNTs-C-200 CE shows the best catalytic activity towards the reduction of I_3^-, thereby leading to an impressive PCE of 9.04% as a low-cost Pt-free CE for application in next-generation DSSCs, showing ~15% overall PCE enhancement compared to the expensive Pt counterpart (7.88%). More importantly, the CoNi@CNTs-C-200 CE also exhibits much better electrochemical stability than conventional Pt CE during long-term electrochemical cycling, which is crucial for practical application in high-performance DSSCs. This work may open up a new route for further study of various metal organic frameworks as templates in design and development of low-cost, environmentally friendly, highly stable and efficient counter electrodes for DSSCs. Due to its unique structure and superior properties, the as-prepared CoNi@CNTs-C-200 may also find wide applications in water splitting, lithium ion batteries, supercapacitors and other fields.

3.5 References

[1] A. Hagfeldt, G. Boschloo, L. Sun, L. Kloo, H. Pettersson, Dye-sensitized solar cells. Chem. Rev. 2010, 110, 6595-6663.

[2] U. Bach, D. Lupo, P. Comte, J.E. Moser, F. Weissortel, J. Salbeck, H. Spreitzer, M. Gratzel, Solid-state dye-sensitized mesoporous TiO_2 solar cells with high photon-to-electron conversion efficiencies. Nature. 1998, 395, 583–585.

[3] H.N. Tian, Z. Yu, A. Hagfeldt, L. Kloo, L. Sun, Organic redox couples and organic counter electrode for efficient organic dye-sensitized solar cells. J. Am. Chem. Soc. 2011, 133, 9413-9422.

[4] M.J. Ju, J.C. Kim, H.J. Choi, I.T. Choi, S.G. Kim, K. Lim, J. Ko, J.J. Lee, I.Y. Jeon, J.B. Baek, H.K. Kim, N-doped graphene nanoplatelets as superior metal-free counter electrodes

for organic dye-sensitized solar cells, ACS Nano. 2013, 7, 5243-5250.

[5] X.J. Zheng, J. Deng, N. Wang, D.H. Deng, W.H. Zhang, X.H. Bao, C. Li, Podlike N-doped carbon nanotubes encapsulating FeNi alloy nanoparticles: high-performance counter electrode materials for dye-sensitized solar cells. Angew. Chem. Int. Ed. 2014, 53, 7023-7027.

[6] E. Olsen, G. Hagen, S.E. Lindquist, Dissolution of platinum in methoxy propionitrile containing LiI/I_2. Sol. Energy Mater. Sol. Cells. 2000, 63, 267–273.

[7] H.N. Tsao, J. Burschka, C.Yi, F. Kessler, M.K. Nazeeruddin, M. Gratzel, Influence of the interfacial charge-transfer resistance at the counter electrode in dye-sensitized solar cells employing cobalt redox shuttles. Energy Environ. Sci. 2011, 4, 4921-4924.

[8] H. Tian, Z. Yu, A. Hagfeldt, L. Kloo, L. Sun, Organic redox couples and organic counter electrode for efficient organic dye-sensitized solar cells. J. Am. Chem. Soc. 2011,133, 9413-9422.

[9] T.N. Murakami, S. Ito, Q. Wang, M.K. Nazeeruddin, T. Bessho, I. Cesar, P. Liska, R. Humphry-Baker, P. Comte, P. Pechy, M. Grätzel, Highly efficient dye-sensitized solar cells based on carbon black counter electrodes. J. Electrochem. Soc. 2006, 153, A2255-A2261.

[9] Y. Xue, J. Liu, H. Chen, R. Wang, D. Li, J. Qu, L. Dai, Nitrogen-doped graphene foams as metal-free counter electrodes in high-performance dye-sensitized solar cells. Angew. Chem. 2012, 51, 12124-12127.

[10] S. Hou, X. Cai, H. Wu, X. Yu, M. Peng, K. Yan, D. Zou, Nitrogen-doped graphene for dye-sensitized solar cells and the role of nitrogen states in triiodide reduction. Energy Environ. Sci. 2013, 6, 3356-3362.

[11] M. Wu, X. Lin, T. Wang, J. Qiu, T. Ma, Low-cost dye-sensitized solar cell based on nine kinds of carbon counter electrodes. Energy Environ. Sci. 2011, 4, 2308-2315.

[12] J. Han, H. Kim, D.Y. Kim, S.M. Jo, S.Y. Jang, Water-soluble polyelectrolyte-grafted multiwalled carbon nanotube thin films for efficient counter electrode of dye-sensitized solar cells. ACS Nano 2010, 4, 3503-3509.

[13] F. Gong, H. Wang, X. Xu, G. Zhou, Z.S. Wang, In situ growth of $Co_{0.85}Se$ and $Ni_{0.85}Se$ on conductive substrates as high-performance counter electrodes for dye-sensitized solar cells. J. Am. Chem. Soc. 2012, 134, 10953-10958.

[14] F. Gong, X. Xu, Z. Li, G. Zhou, Z.S. Wang, $NiSe_2$ as an efficient electrocatalyst for a Pt-free counter electrode of dye-sensitized solar cells. Chem. Commun. 2013, 49, 1437-1439.

[15] X.D. Cui, W.W. Xu, Z.Q. Xie, Y. Wang, High-performance dye-sensitized solar cells based on Ag-doped SnS_2 counter electrodes. J. Mater. Chem. A. 2016, 4, 1908-1914.

[16] X.D. Cui, W.W. Xu, Z.Q. Xie, Y. Wang, Hierarchical SnO_2@ SnS_2 counter electrodes for remarkable high-efficiency dye-sensitized solar cells. Electrochim. Acta, 2015, 186, 125-132.

[17] M. Wu, X. Lin, Y. Wang, L. Wang, W. Guo, D. Qi, X. Peng, A. Hagfeldt, M. Grätzel, T. Ma, Economical Pt-free catalysts for counter electrodes of dye-sensitized solar cells. J. Am. Chem. Soc. 2012, 134, 3419-3428.

[18] Y. Hou, D. Wang, X.H. Yang, W.Q. Fang, B. Zhang, H.F. Wang, G.Z. Lu, P. Hu, H.J. Zhao, H.G. Yang, Rational screening low-cost counter electrodes for dye-sensitized solar cells. Nat. Commun. 2013, 4, 1583.

[19] L. Wang, Y.T. Shi, H. Zhang, X.G. Bai, Y.X. Wang, T.L. Ma, Iron oxide nanostructures as highly efficient heterogeneous catalysts for mesoscopic photovoltaics. J. Mater. Chem. A 2014, 2, 15279–15283.

[20] L. Wang, Y.T. Shi, Y.X. Wang, H. Zhang, H.W. Zhou, Y. Wei, S.Y. Tao, T.L. Ma, Composite catalyst of rosin carbon/Fe_3O_4: highly efficient counter electrode for dye-sensitized solar cells. Chem. Commun. 2014, 50, 1701-1703.

[21] M. X. Wu, X. Lin, A. Hagfeldt, T. L. Ma, Low-cost molybdenum carbide and tungsten carbide counter electrodes for dye-sensitized solar cells. Angew. Chem. 2011, 50, 3520-3524.

[22] Q.H. Li, J.H. Wu, Q.W. Tang, Z. Lan, P.J. Li, J.M. Lin, L.Q. Fan, Application of microporous polyaniline counter electrode for dye-sensitized solar cells. Electrochem. Commun. 2008, 10, 1299-1302.

[23] J.H. Wu, Q.H. Li, L.Q. Fan, Z. Lan, P.J. Li, J.M. Lin, S.C. Hao, High-performance polypyrrole nanoparticles counter electrode for dye-sensitized solar cells. J. Power Sources 2008, 181, 172-176.

[24] M. Motlak, N.A.M. Barakat, A.G. Ei-Deen, A.M. Hamza, M. Obaid, O.B. Yang, M.S. Akhtar, K.A. Khalil, NiCu bimetallic nanoparticle-decorated graphene as novel and cost-effective counter electrode for dye-sensitized solar cells and electrocatalyst for methanol oxidation. Appl. Catal. A, 2015, 501, 41-47.

[25] M. Motlak, N.A.M. Barakat, M.S. Akhtar, A.M. Hamza, B.S. Kim, C.S. Kim, K.A. Khalil, A. A. Almajid, High performance of NiCo nanoparticles-doped carbon nanofibers as counter electrode for dye-sensitized solar cells. Electrochim. Acta 2015, 160, 1-6.

[26] M. Hu, J. Reboul, S. Furukawa, L. Radhakrishnan, Y. Zhang, P. Srinivasu, H. Iwai, H. Wang, Y. Nemoto, N. Suzuki, S. Kitagawa and Y. Yamauchi, Direct synthesis of nanoporous carbon nitride fibers using Al-based porous coordination polymers (Al-PCPs). Chem. Commun. 2011, 47, 8124-8126.

[27] W. Cho, Y.H. Lee, H.J. Lee, M. Oh, Systematic transformation of coordination polymer particles to hollow and non-hollow In_2O_3 with pre-defined morphology. Chem. Commun. 2009, 31, 4756-4758.

[28] W. Xia, R.Q. Zou, L. An, D.G. Xia, S.J. Guo, A metal–organic framework route to in situ encapsulation of Co@Co_3O_4@C core@bishell nanoparticles into a highly ordered porous carbon matrix for oxygen reduction. Energy Environ. Sci. 2015, 8, 568-576.

[29] Y. Hou, J.Y. Li, Z.H. Wen, S.M. Cui, C. Yuan, J.H. Chen, Co_3O_4 nanoparticles embedded in nitrogen-doped porous carbon dodecahedrons with enhanced electrochemical properties for lithium storage and water splitting. Nano Energy. 2015, 12, 1-8.

[30] X.D. Cui, Z.Q. Xie, Y. Wang, Novel CoS_2 embedded carbon nanocages by direct sulfurizing metal–organic frameworks for dye-sensitized solar cells, Nanoscale 2016, 8, 11984-11992.

[31] L.T. Yu, J. Liu, X.J. Xu, L.G. Zhang, R.Z. Hu, J.W. Liu, L.C. Yang, M. Zhu, Metal-organic framework-derived NiSb alloy embedded in carbon hollow spheres as superior lithium-ion battery anodes, ACS Appl. Mater. Interfaces, 2016, DOI: 10.1021/acsami.6b14233.

[32] X.N. Li, A.I. Rykov, B. Zhang, Y.J. Zhang, J.H. Wang, Graphene encapsulated Fe_xCo_y nanocages derived from metal-organic frameworks as efficient activators for peroxymonosulfate, Catal. Sci. Technol. 2016, 6, 7486-7494.

[33] J.K. Sun, Q. Xu, Functional materials derived from open framework templates/precursors: synthesis and applications. *Energy Environ. Sci.* 2014, 7, 2071-2100.

[34] M.J. Hu, B. Lin, S.H. Yu, Magnetic field-induced solvothermal synthesis of one-dimensional assemblies of Ni-Co alloy microstructures. Nano Res. 2008, 1, 303-313.

[35] M.J. Hu, Y. Lu, S. Zhang, S.R. Guo, B. Lin, M. Zheng, S.H. Yu, High yield synthesis of bracelet-like hydrophilic Ni-Co magnetic alloy flux-closure nanorings. J. Am. Chem. Soc. 2008, 130, 11606-11607.

[36] D.H. Deng, L. Yu, X.Q. Chen, G.X. Wang, L. Jin, X.L. Pan, J. Deng, G.Q. Sun, X.H. Bao, Iron encapsulated within pod-like carbon nanotubes for oxygen reduction reaction. Angew. Chem. 2013, 52, 371-375.

[37] J. Deng, L. Yu, D.H. Deng, X.Q. Chen, F. Yang, X.H. Bao, Highly active reduction of oxygen on a FeCo alloy catalyst encapsulated in pod-like carbon nanotubes with fewer walls. J. Mater. Chem. A 2013, 1, 14868-14873.

[38] Z.Q. Xie, Z.Y. He, X.H. Feng, W.W. Xu, X.D. Cui, J.H. Zhang, C. Yan; M. A. Carreon, Z. Liu, Y. Wang, Hierarchical sandwich-like structure of ultrafine N-rich porous carbon nanospheres grown on graphene sheets as superior lithium-ion battery anodes. ACS Appl. Mater. Interfaces. 2016, 8, 10324-10333.

[39] S.N. Yun, A. Hagfeldt, T. L. Ma, Pt-free counter electrode for dye-sensitized solar cells with high efficiency. Adv. Mater. 2014, 26, 6210-6237.

[40] T.Y. Hsieh, T.C. Wei, P. Zhai, S.P. Feng, M. Ikegami, T. Miyasaka, A room-temperature process for fabricating a nano-Pt counter electrode on a plastic substrate for efficient dye-sensitized cells. J. Power Sources 2015, 283, 351-357.

[41] M.X. Wu, Y.D. Wang, X. Lin, N. Yu, L. Wang, L.L. Wang, A. Hagfeldt, T.L. Ma, Economical and effective sulfide catalysts for dye-sensitized solar cells as counter electrodes. Phys. Chem. Chem. Phys. 2011, 13, 19298-19301.

CHAPTER 4. METAL-ORGANIC FRAMEWORK DERIVED ELECTROCATALYSTS FOR OXYGEN EVOLUTION REACTION

4.1 Overview

As described in Chapter 2 and 3, metal-organic frameworks can serve as ideal templates/precursors to synthesize nanostructured electrode materials with tunable chemical composition and desirable electrochemical properties for LIBs and DSSCs. Electrocatalytic water splitting is another promising energy technology to produce hydrogen as an efficient energy storage carrier thanks to its abundant and sustainable nature. As introduced in Chapter 1, the major challenge of water splitting is its sluggish kinetics of oxygen evolution reaction (OER) as compared to hydrogen evolution reaction (HER), which usually requires a large overpotential for multi-step transfer of four electrons. Up to date, noble metal oxides such as ruthenium oxides (RuO_2) and iridium oxides (IrO_2) are efficient electrocatalysts for OER. Nevertheless, their large-scale applications are severely hindered by the high cost and scarcity of the noble metals. In addition, these noble metal oxides exhibit poor chemical stability in alkaline solution.

In the first section of Chapter 4, MOF derived CoNi embedded carbon nanocages are synthesized and evaluated as an economical electrocatalysts for OER. It is found that CoNi-C-200 shows an overpotential of 408 mV at a current density of 10 mA cm^{-2}, which is comparable commercial noble metal oxides electrocatalysts. To further lower the overpotential of MOF derived electrocatalysts, it is still highly needed to design and synthesize electrocatalysts with sufficient targeted active sites such as CoN_x species, topological defects (e.g., edge sites), pyridinic and/or graphitic N dopants. In this regard, the second section of Chapter 4 presents a simple and scalable synthesis of MOF-derived CoN_x@Co/N-doped carbon tubes hybrids (denoted as CoN_x@Co/NCT hereinafter) via one-step pyrolysis of ZIF-67 at a low temperature of 650 ^oC with the introduction of urea. The CoN_x@Co/NCT hybrid shows an overpotential as low as 290 mV at 10 mA cm^{-2} with a small Tafel slope of 60 mV/dec, which exceeds most noble metal-free electrocatalysts for OER.

4.2 Metal-Organic Framework Derived CoNi-Embedded Carbon Nanocages as Efficient Electrocatalysts for Oxygen Evolution Reaction*

4.2.1 Introduction

With ever-increasing energy demands and depletion of fossil fuels, extensive efforts have been devoted to exploring new sustainable and environment-friendly energy conversion and storage systems [1,2]. Hydrogen has attracted wide attention as an efficient energy storage carrier thanks to its abundant and sustainable nature [3]. In the present, electrolysis of water is considered as the most efficient ways to produce high-purity hydrogen at low cost [4,5]. The splitting of water involves two half reactions [6,7]. At the cathode, protons are reduced to hydrogen in the alkaline solution $2H^+ + 2e^- \rightarrow H_2$ (hydrogen evolution reaction, HER). At the anode, four hydroxyl groups are oxidized to oxygen in alkaline solution $4OH^- \rightarrow O_2 + 2H_2O + 4e^-$ (oxygen evolution reaction, OER). The major challenge of water splitting is the sluggish kinetics of OER as compared to HER, which usually requires a large overpotential for multi-step transfer of four electrons [8]. Up to date, noble metal oxides such

* Reprinted with permission from Zhiqiang Xie and Ying Wang, Metal-organic framework derived CoNi@CNTs embedded carbon nanocages as efficient electrocatalysts for oxygen evolution reaction. Ionics, 2017, 1-8. Copyright 2017 Springer Nature.

as ruthenium oxides (RuO_2) and iridium oxides (IrO_2) are efficient electrocatalysts for OER [9,10]. Nevertheless, their large-scale applications are severely hindered by the high cost and scarcity of the noble metals. In addition, these noble metal oxides exhibit poor chemical stability in alkaline solution.

To overcome the aforementioned challenges, it is always desirable to explore new alternatives to replace noble metal oxides as low-cost and efficient electrocatalysts for OER. To date, various noble metal-free electrocatalysts such as transition metal oxides [11], hydroxides [12], nitrides [13], sulfides [14] and phosphides [15], have been widely reported. Unfortunately, most of these materials are either limited by their low electrical conductivities or poor electrocatalytic activities, resulting in much higher overpotential at a current density of 10 mA cm^{-2} compared to RuO_2 (410 mV) [16]. Recently, transition metal alloys have attracted more and more interest, owing to their low cost and environmental benignity. So far, various transition metal alloys such as NiFe, NiCu, NiCe and their composites have been explored for OER [17]. Despite much progress having been made in the development of transition metal alloy-based catalyst for OER, the catalytic activity of OER is still not comparable to commercial noble metal oxide catalyst. Such limited performance is originated from the complex synthesis and much stricter requirement for the transition metal alloy-based catalysts such as chemical composition, particle size and structural stability. Therefore, more efforts are highly needed to optimize the transition metal alloy-based catalysts for efficient OER.

Metal-organic frameworks (MOFs), built from metal ions/clusters as nodes and organic linkers as struts, have attracted more and more interest in recent years due to their high surface area, large pore volume and diverse structures [18]. Inspired by these features, MOFs have been reported as new templates and precursors for synthesis of various hierarchical nanostructured materials such as porous carbons [19], metal oxides [20], metal/carbon composites [21] and metal oxides/carbon composites [22]. These MOF-derived nanostructures can offer many unique advantages: (i) the chemical composition can be easily tuned by designing MOFs combined with specific thermal treatment; (ii) MOF-derived nanostructures provide controlled porosity and huge surface area, which can effectively facilitate the access of electrolyte into the electrode and ensure large electrolyte/electrode contact area; (iii) the charge diffusion lengths can be largely shortened and thus facilitate the charge transfer for OER activity; (iv) the low cost and ease of synthesis allow MOF-derived nanostructures to be potentially scaled up for industrial applications. Up to now, transition metal alloy nanoparticles have emerged as new candidates for electrocatalyst for OER, however, the preparation of metal alloy/carbon nanostructures by using bimetallic MOFs as the single precursor has rarely been reported [23,24]. Compared to other synthesis methods of alloy nanoparticles, one-step pyrolysis of bimetallic MOFs offers a facile route to prepare well-dispersed alloy nanoparticles embedded conductive carbon matrix without using any surfactants or toxic reducing agent. The chemical composition and particle size of alloy can also be optimized by simply varying the mixed metal ions ratio during the synthesis.

To combine the merits of transition metal alloy and MOF-derived nanostructures, we synthesized novel CoNi alloy embedded carbon nanocages (CoNi-C), through one-step pyrolysis of Co/Ni bimetallic metal organic framework (MOF) in argon atmosphere. Within such MOF-derived nanostructure, inner CoNi alloy nanoparticles can offer numerous active sites to efficiently catalyze the redox reactions, meanwhile the carbon nanocages serve as conductive network supporting the CoNi catalysts, which can effectively prevent CoNi nanoparticles from aggregation and reduce corrosion by alkaline electrolyte during long-term operation. As a result, CoNi-C-200 with a Co/Ni atomic ratio of 9:1 demonstrates obviously enhanced catalytic activity for OER in 1M KOH aqueous solution compared with cobalt nanoparticles embedded nanocages (Co-C), showing a small overpotential of 408 mV for a

current density of 10 mA cm^{-2} and a smaller overpotential of 366 mV after 5000 cyclic voltammetric sweeps. To the best of our knowledge, this work is the first report on the application of MOF-derived transition metal alloys as efficient and robust catalysts for OER. We believe that the strategy presented here opens up a new route to development of versatile metal alloy/carbon nanocomposites for wide electrochemical applications, such as dye-sensitized solar cells, photocatalysts and so forth.

4.2.2 Experimental

Preparation of Co-C and CoNi-C

The pure ZIF-67 powders were prepared according to previous reports with some modifications [5, 6]. In brief, 2 g cobalt nitrate hexahydrate and 3.06 g 2-methylimidazole were separately dissolved in 100 ml methanol, respectively. Afterwards, the two solutions were mixed under stirring for 10 min and aged for 24 h at room temperature. The resultant purple solid was collected from the solution by centrifugation at 4000 rpm for 10 min and then washed with methanol at least three times. After washing, the ZIF-67 powders were dried overnight at 80 ^{o}C. Afterwards, cobalt nanoparticles embedded within N-doped carbon nanocages (Co-C) were prepared by a facile calcination of ZIF-67 nanocrystals at 900 ^{o}C for 2 hours in Ar atmosphere.

Similar to synthesis of ZIF-67, Co/Ni bimetallic MOFs were prepared by using 2 g cobalt nitrate hexahydrate, 3.06 g 2-methylimidazole and different amounts of nickel nitrate hexahydrate (100, 200, 400 mg, respectively). Afterwards, Co/Ni based MOFs were transformed to CoNi-C by a direct pyrolysis at 900 ^{o}C for 2 hours in Ar atmosphere. For convenience, the as-prepared CoNi-C samples were labeled as CoNi-C-100, CoNi-C-200 and CoNi-C-400, respectively.

Characterizations

The crystalline structures of as-obtained products were identified by using X-ray diffraction (XRD) technique, and the data were recorded at a constant scanning rate of 2 ^{o}/min on a Rigaku MiniFlex X-ray diffractometer (Cu Kα radiation). The microstructures and morphologies of samples were characterized by using scanning electron microscope (SEM) and high-resolution transmission electron microscope (HRTEM). The SEM imaging was carried out on a FEI Quanta 3D FEG FIB/SEM, which is equipped with energy-dispersive X-ray spectroscopy (EDS). TEM and HRTEM imaging was performed on a JEOL JEM-2010 microscope at 200 kV.

Electrochemical measurements

The electrochemical measurements were performed by using a CHI 760D electrochemical workstation (CH Instruments, Inc.) and a rotating disk electrode controller (AFMSRCE, Pine Instrument Co.). A platinum wire and Ag/AgCl electrode were used as counter electrode and reference electrode, respectively. The measured potentials vs. Ag/AgCl were converted to reversible hydrogen electrode (RHE).

To prepare catalyst film-coated glassy carbon working electrode, 8 mg powders were dispersed in 2mL freshly prepared dispersion solution (Ethanol/Nafion=100:1(V/V)), following by sonication for 1 hour. Afterwards, 10 μL fresh catalyst ink was deposited on a rotating disk electrode with geometric area of 0.196 cm^2 by a house-built spinning coating device under a gentle airflow.

The oxygen evolution reaction (OER) properties of the CoNi-C-100, CoNi-C-200 and CoNi-C-400 and Co-C catalysts were studied using linear sweep voltammetry (LSV). The potential was swept at a scan rate of 5 mV s^{-1} and an electrode rotation rate of 1600 rpm in N_2-saturated 1M KOH aqueous solution. The electrochemical impedance spectroscopy (EIS) measurements were carried out in the frequency range from 10^5 Hz to 0.01 Hz using an electrochemical workstation (CHI 6504C). To study the electrochemical stability of as-prepared electrocatalysts, the cyclic voltammetry (CV) was carried out at a scan rate of 100 mV s^{-1} for up to 5000 cycles.

4.2.3 Results and discussion

The overall synthesis of MOF-derived CoNi-C nanostructures involves two steps. In the first step, the Co/Ni bimetallic metal organic frameworks (MOFs) are synthesized using various ratio of Co^{2+}/Ni^{2+} and 2-methylimidazole at room temperature. During the following pyrolysis process at 900 ^oC for 2 h, Co^{2+} and Ni^{2+} are simultaneously reduced into metallic Co and Ni by the resultant carbon from the decomposition of organic linkers at high temperature, and meanwhile metallic Co and Ni undergo the alloying reaction process to form CoNi alloy nanoparticles, which can subsequently function as catalyst to promote the formation of onion-like carbon around them.

To identify the crystalline structures and phases of the MOF-derived CoNi-C samples, the powder X-ray diffraction (XRD) measurements are first performed. The XRD results show that all the CoNi-C samples are composed of graphitic carbon and face-centered cubic (fcc) CoNi alloy (Figure 4.2.1a). It is clearly observed that the strongest (111) reflection peak positions of all samples lie between the peak position of pure Co (JCPDS# 15-0806) and pure Ni (JCPDS# 04-0850) (Figure 4.2.1b), which is well consistent with previously reported CoNi alloys [27,28]. The main (111) peaks of CoNi-C samples obviously shift to higher angles with the increase of Ni^{2+} amounts during the synthesis, further confirming the formation of CoNi alloys. No other impurities or phases are observed, implying a complete transformation of Ni^{2+} incorporated ZIF-67 to CoNi-C. In addition, the sharp peaks in the XRD spectra of the CoNi alloy indicate that the samples are highly crystalline.

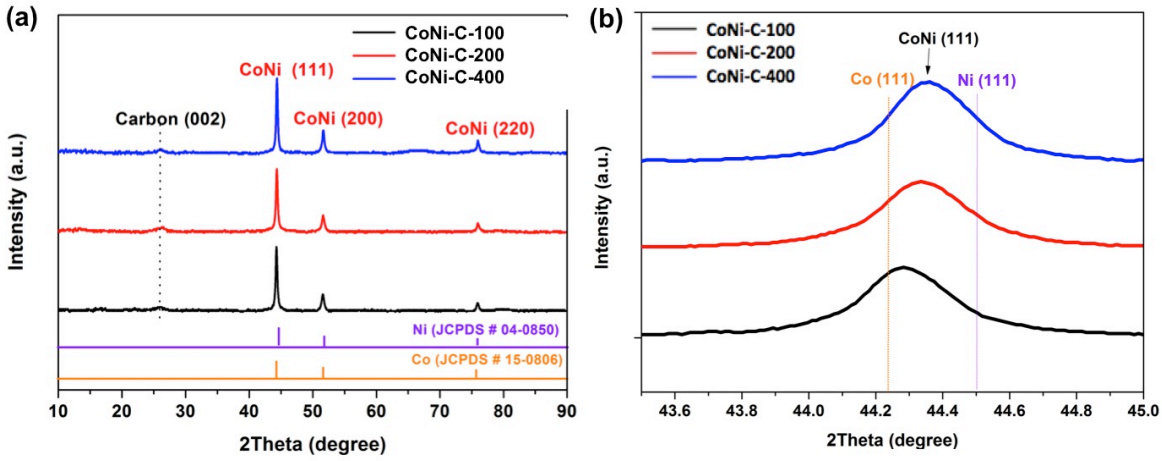

Figure 4.2.1 (a) XRD patterns and (b) Selected enlarged portion of CoNi-C-100, CoNi-C-200 and CoNi-C-400 samples in comparison with standard XRD peaks of pure Co and Ni.

Scanning electron microscopy (SEM) images show that ZIF-67 samples are composed of polyhedron-like particles with smooth surfaces. After one-step pyrolysis process

in inert gas atmosphere, the low-magnification SEM images in Figure 4.2.2a and c show that the as-synthesized CoNi@-C-100 and CoNi-C-200 samples consist of polyhedron-like carbon nanocages (200~500 nm) with CoNi alloy nanoparticles well embedded. By comparison of high-magnification SEM images in Figure 2b and 2d, it is observed that larger particles are embedded within the carbon nanocages in the CoNi-C-200 sample than CoNi-C-100. On the contrary, some of the carbon nanocages in CoNi-C-400 sample are broken and one can notice that relatively larger CoNi alloy particles are located outside the carbon nanocages (Figure 4.2.2e-f). This observation indicates that the Ni amount plays a crucial role in control of the particle size of CoNi alloy.

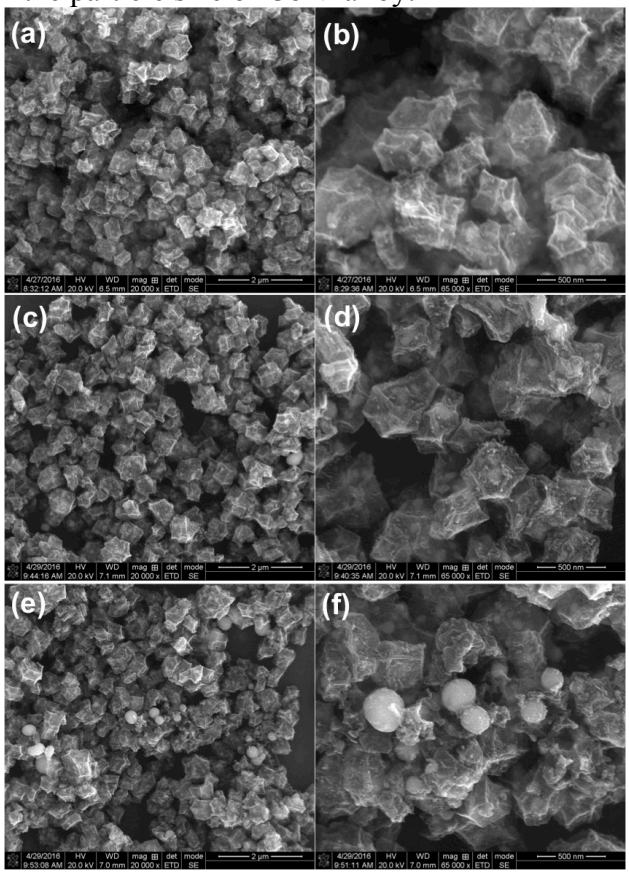

Figure 4.2.2 SEM images of (a, b) CoNi-C-100, (c, d) CoNi-C-200 and (e, f) CoNi-C-400.

Experiments presented further in the work show that the catalyst based on the CoNi-C-200 demonstrates the highest catalytic activity for OER, and therefore we perform detailed transmission electron microscopy (TEM) and high resolution (HR) TEM characterizations for better visualization of its nanostructure, as displayed in Figure 4.2.3a-d. It can be clearly observed that CoNi alloy nanoparticles with the size of 20 ~ 100 nm (dark dots) are well embedded in carbon nanocages (grey framework) in CoNi-C-200 sample. Interestingly, one can observe that CoNi nanoparticles are encapsulated by onion-like carbon (marked by blue arrows in Figure 4.2.3d). As we can see from the inset in Figure 4.2.3d, the distinct lattice fringe with the measured d-spacing of 0.21 nm can be assigned to the (111) plane of CoNi alloy, which further confirms successful formation of MOF-derived CoNi alloy through a facile one-step pyrolysis process in inert gas atmosphere. Thus, the SEM and TEM observations above indicate that we have successfully obtained the CoNi-C sample with a unique nanostructure, whereas CoNi alloy nanoparticles are well encapsulated into the onion-like carbon, meanwhile they are completely embedded into carbon nanocages.

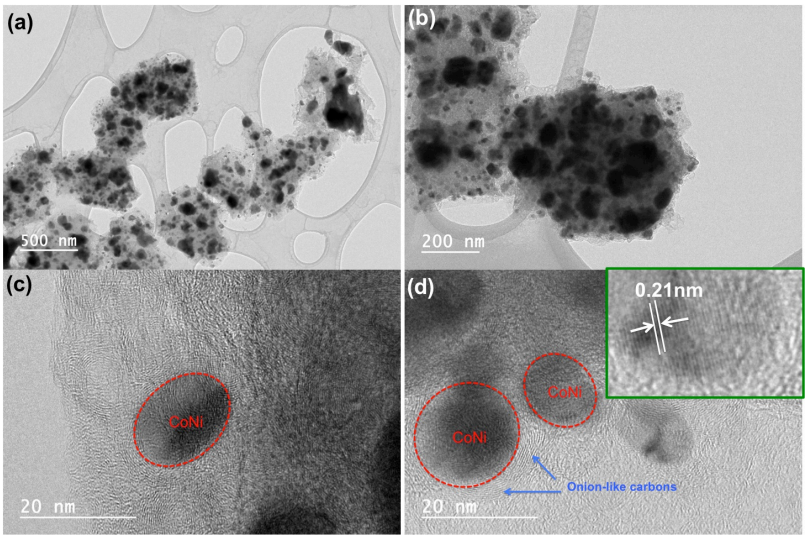

Figure 4.2.3 (a, b) TEM images and (c, d) HRTEM images of CoNi-C-200 (optimal sample).

The corresponding energy-dispersive X-ray (EDS) mapping results further confirm the coexistence of C, Co and Ni elements within the sample, and both Co and Ni elements show homogeneous distribution for the inner nanoparticles within the carbon nanocages, confirming the CoNi alloy phase, which are well consistent with previous XRD and TEM results. It is also worth noting that chemical composition of the as-prepared CoNi alloy in our work can be easily tuned by varying the atomic ratio of cobalt and nickel ions during the synthesis of Ni^{2+} incorporated ZIF-67 nanocrystals. The atomic ratio of Co/Ni in the optimal sample CoNi-C-200 is found to be 9:1 through EDS mapping results, indicating a certain amount of Ni ions can be encapsulated within ZIF-67 nanocrystals during the synthesis process in methanol at room temperature. Thanks to such a unique hierarchical nanostructure composed of CoNi embedded carbon nanocages, the as-prepared CoNi-C composites are explored as catalysts for OER for the first time.

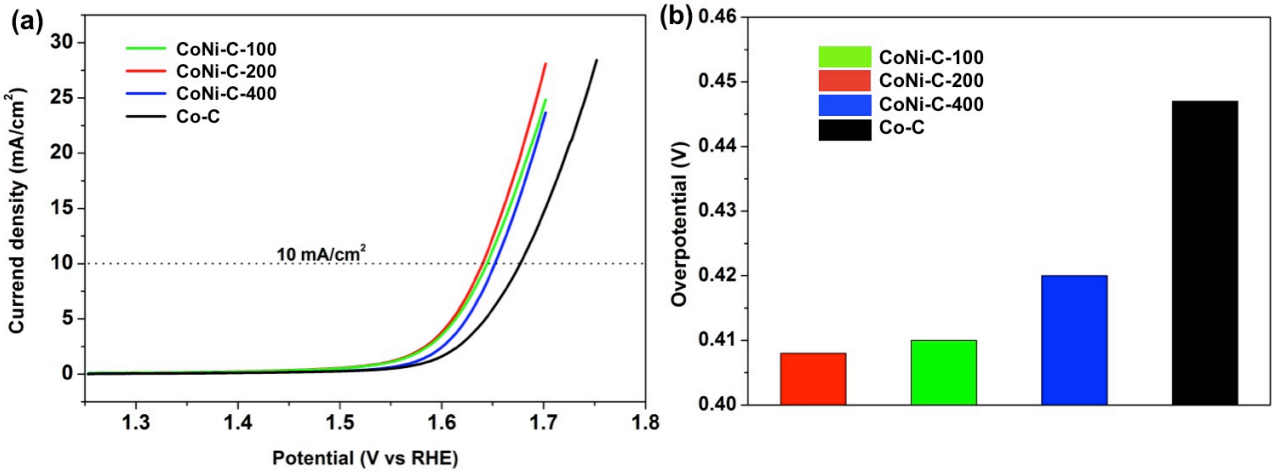

Figure 4.2.4 (a) Comparison of OER polarization curves of CoNi-C-100, CoNi-C-200, CoNi-C-400 and Co-C, measured in 1 M KOH aqueous solution at a scan rate of 5 mV/s. (b) The overpotentials needed to reach a current density of 10 mA/cm^2 for the above four catalysts.

The catalytic activities of CoNi-C-100, CoNi-C-200, CoNi-C-400 and Co-C for OER are measured using a typical three-electrode system in 1M KOH aqueous solutions. The

potentials reported in this paper are all versus reversible hydrogen electrode (RHE). Figure 4a shows the linear sweep voltammetry (LSV) curves of all the electrodes at a scan rate of 5 mV s^{-1}. The polarization curve from the CoNi-C-200 catalyst exhibits the smallest onset potential of ~ 1.638 V and highest current density. As shown in Figure 4.2.4b, the overpotential of CoNi-C-200 catalyst is 408 mV at the current density of 10 mA cm^{-2}, which is slightly lower than CoNi-C-100 (410 mV) and CoNi-C-400 (420 mV). These results indicate that the intrinsic OER activities for these three CoNi-based catalysts are similar. The difference in OER current densities could be attributed to the different number of active sites and surface area needed for electron transfer and ion transport in the catalysts. The ion transport refers to the OH^- adsorption and transfer to the active sites in the electrocatalysts. In contrast, the Co-C catalyst has much higher overpotential of 447 mV, showing the worst catalytic activity for OER. Therefore, it can be concluded that the CoNi alloy-based catalysts exhibit significantly enhanced OER activity compared to Co-C catalyst. This result can be attributed to the synergistic effects of Co and Ni in the alloy. Specifically, the incorporation of a secondary transition metal Ni results in the OH^- adsorption energies alteration via tuning the lattice and bond length of the crystal, favoring the OER catalytic activities [29,30]. Comparing our optimal sample with other previously reported electrocatalysts for OER, it is found that CoNi-C-200 demonstrates a lower overpotential than IrO_2 (450 mV) [31], $Mn_3O_4/CoSe_2$ (450 mV) [32], N-graphene/CNT (420 mV) [33]. In addition, its electrocatalytic performance is even comparable to commercial noble Ir/C (390 mV) [34]. Instead of using expensive noble metal or metal oxides as electrocatalysts, our work shows that the CoNi-C-200 holds great potential as an efficient and economical electrocatalyst for OER.

To better understand the OER electrochemical kinetics, we fit the polarization curves to the Tafel equation $\eta = b*\log(j)$, where η is the overpotential, b is the Tafel slope, j is the current density [35,36]. A smaller Tafel slope value represents a smaller increase in overpotential, corresponding to a more efficient OER activity [37,38]. The Tafel slope plots, along with the slope values, are shown in Figure 5. The Tafel slopes of CoNi-C-100, CoNi-C-200, CoNi-C-400 and Co-C are 93, 83, 94, 97 mV dec^{-1}, respectively. The CoNi-C-200 catalyst displays the smallest Tafel slope in 1M KOH aqueous solutions, indicating the best catalytic activity for OER.

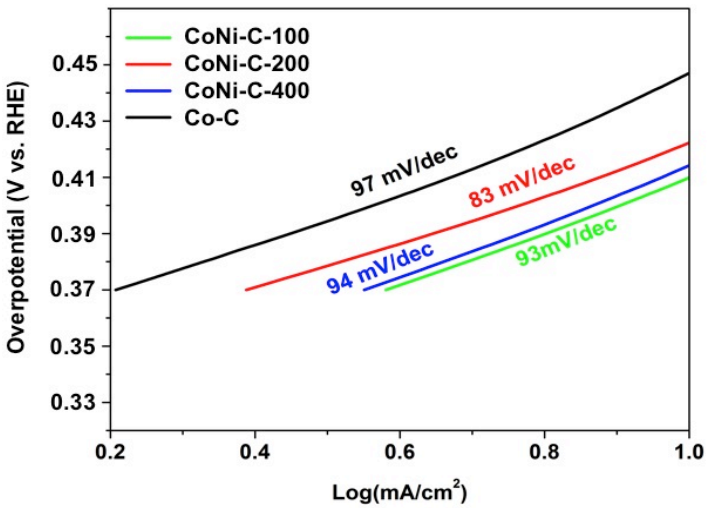

Figure 4.2.5 (a) Tafel plots of CoNi-C-100, CoNi-C-200, CoNi-C-400 and Co-C, measured in 1 M KOH aqueous solution.

In addition to high catalytic activity, durability is another critical parameter that

determines the practical application of catalysts for OER. Thus, in this study, we perform an accelerated degradation test for evaluation of OER stability. As shown in Figure 4.2.6, the polarization curves of CoNi-C-200 (the optimal sample) are recorded after 0, 100, 200, 300, 400, 500, 1000 and 5000 cyclic voltammetric sweeps at a scan rate of 100 mV s^{-1}. It is interesting to notice a current density increase and reduction of overpotential during the initial 300 cyclic voltammetric sweeps. The polarization curves of CoNi-C-200 show a negligible change from 300 to 5000 cyclic voltammetric sweeps, indicating its superior long-term stability as a robust catalyst for OER. It is worth mentioning that CoNi-C-200 exhibits a smaller overpotential of 366 mV after 5000 cyclic voltammetric sweeps.

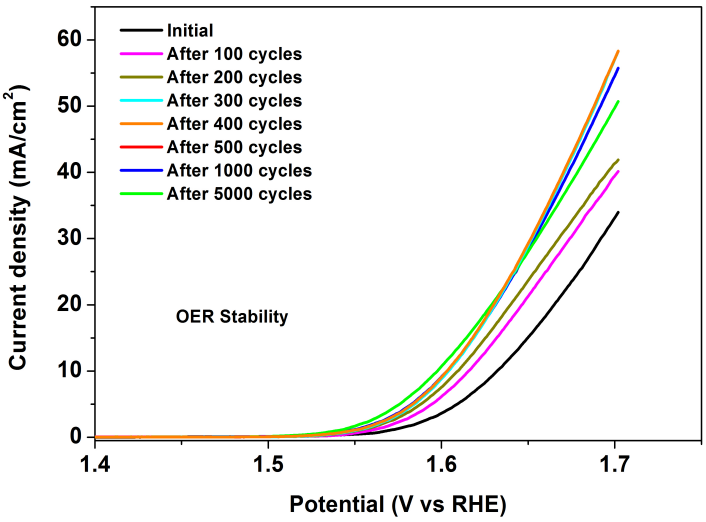

Figure 4.2.6 OER stability test (5000 cyclic voltammetric sweeps) of CoNi-C-200 (the optimal sample) in 1 M KOH aqueous solution at a scan rate of 100 mV/s.

Electrochemical impedance spectroscopy (EIS) measurements are conducted to provide further insight into the kinetics of catalytic reactions of as-prepared catalysts. Figure 4.2.7 displays typical Nyquist plots of CoNi-C-100, CoNi-C-200, CoNi-C-400 and Co-C electrodes when tested at E= 1.638 V in the 1M KOH electrolyte. As we can see that all Nyquist plots are composed of depressed semicircles corresponding to the charge-transfer process for the OER. The Nyquist plots are fitted and can be represented by one capacitive loop, cell resistance (R_Ω) and the charge-transfer resistance (R_{ct}) for the OER. The depressed semicircle corresponds to the R_{ct}. According to previous reports, smaller R_{ct} usually indicates higher catalytic activity for OER. As we can see from Figure 6 that the four catalysts exhibit similar R_Ω, however, it is clearly observed that CoNi-C-200 shows a smaller semicircle than other catalysts, indicating the best catalytic activity among all the catalysts. These results are in good accordance with the LSV observations.

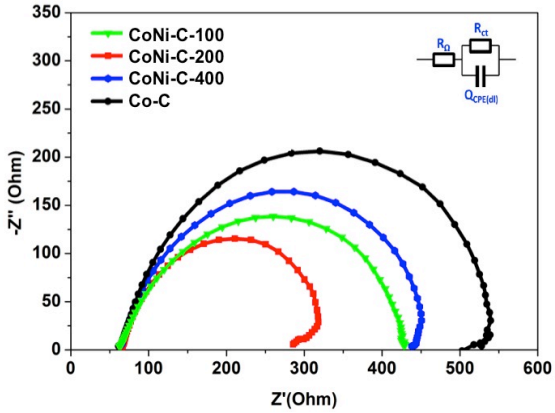

Figure 4.2.7 Nyquist plots of CoNi-C-100, CoNi-C-200, CoNi-C-400 and Co-C electrodes tested at E= 1.638 V.

All the electrochemical measurements above indicate that CoNi-C catalysts exhibit high catalytic activity and good durability for OER. For practical application in a real industrial water splitting cell, the cost of electrocatalysts is another crucial factor that has to be taken into account. Unlike the scarcity and high cost of noble metal or their metal oxides as commercial OER electrocatalysts, the elements of CoNi-C catalysts are earth abundant and less expensive. Thus, the CoNi-C catalysts can be produced at low cost on a large scale. Furthermore, the whole synthesis procedure of CoNi-C catalysts is facile and economical due to the use of cheap precursors and simple one-step annealing treatment, which offers great potential in large-scale production of catalysts for water splitting application. Considering both excellent OER performance and low cost of catalysts, we believe the CoNi-C catalysts hold great promise in water splitting applications. In the future, we plan to fabricate a massive electrode by coating the as-prepared catalysts onto a large-sized substrate and investigate its OER performance for a real industrial water splitting cell.

4.2.4 Conclusions

In summary, for the first time, we report a facile synthesis of CoNi embedded carbon nanocages by direct pyrolysis of bimetallic metal organic frameworks in inert gas atmosphere and study their electrocatalytic performance in OER. It is found that CoNi-C-200 shows a small overpotential of 408 mV at a current density of 10 mA cm^{-2} and a small Tafel slope of 83 mV dec^{-1}, demonstrating the best catalytic activity for OER compared to CoNi-C-100, CoNi-C-400 and Co-C catalysts. In addition, CoNi-C-200 exhibits a smaller overpotential of 366 mV after 5000 cyclic voltammetric sweeps, indicating a superior long-term stability. The enhancement in catalytic activity and long-term electrochemical stability can be attributed to the unique morphology and the synergistic effects of CoNi alloy and carbon component in the composite. Considering the facile synthesis of catalysts and their excellent catalytic activities in alkaline medium, the CoNi-C-200 shows great potential as an economic catalyst for OER applications. In addition, this work may open up a new route for further study of various metal organic frameworks as templates in design and development of low-cost and efficient catalysts for OER. Due to its unique structure and superior properties, the as-prepared CoNi-C-200 may also find wide applications in other fields such as dye-sensitized solar cells, photocatalysts and so forth.

4.2.5 References

[1] W. W Xu, K.N. Zhao, L. Zhang, Z. Q. Xie, Cai ZY and Wang Y, SnS_2@graphene nanosheet arrays grown on carbon cloth as freestanding binder-free flexible anodes for advanced sodium batteries, J. Alloy. Comp 2016, 654, 357-362.

[2] Z. Q. Xie, W. W. Xu, X. D. Cui and Y. Wang, Recent progress in metal-organic frameworks and their derived nanostructures for energy and environmental applications, ChemSusChem, 2017, 10, 1645-1663.

[3] S. Mao, Z. Wen, T. Huang, Y. Hou and J. Chen, High-performance bi-functional electrocatalysts of 3D crumpled graphene–cobalt oxide nanohybrids for oxygen reduction and evolution reactions, Energy Environ. Sci, 2014, 7, 609-616.

[4] I. Flis-Kabulska, J. Flis, Y. Sun and T. Zakroczymski, Hydrogen evolution on plasma carburised nickel and effect of iron deposition from the electrolyte in alkaline water electrolysis, Electrochim. Acta, 2015, 167, 61-68.

[5] J. Sato, N. Saito, Y. Yamada, K. Maeda, T. Takata, J. N. Kondo, M. Hara, H. Kobayashi, K. Domen and Y. Inoue, RuO_2-loaded β-Ge_3N_4 as a non-oxide photocatalyst for overall water splitting, J. Am. Chem. Soc, 2005, 127, 4150-4151.

[6] W. Bian, Z. Yang, P. Strasser and R. Yang, A $CoFe_2O_4$/graphene nanohybrid as an efficient bi-functional electrocatalyst for oxygen reduction and oxygen evolution, J. Power Sources, 2014, 250, 196-203.

[7] Y. Z. Su, Q. Z. Xu, Q. S. Zhong, S. T. Shi, C. J. Zhang and C. W. Xu, $NiCo_2O_4$/C prepared by one-step intermittent microwave heating method for oxygen evolution reaction in splitter, J. Alloy Compd, 2014, 617, 115-119.

[8] M. Xiao, Y. Tian, Y. Yan, K. Feng and Y. Miao, Electrodeposition of $Ni(OH)_2$/NiOOH in the presence of urea for the improved oxygen evolution, Electrochim. Acta, 2015, 164, 196-202.

[9] Y. Lee, J. Suntivich, K. J. May, E. E. Perry and Y. Shao-Horn, Synthesis and activities of rutile IrO_2 and RuO_2 nanoparticles for oxygen evolution in acid and alkaline solutions, J. Phys. Chem. Lett, 2012, 3, 399-404.

[10] Y. Qiu, L. Xin and W. Li, Electrocatalytic oxygen evolution over supported small amorphous Ni-Fe nanoparticles in alkaline electrolyte, Langmuir, 2014, 30, 7893-7901.

[11] Y. Y. Liang, Y. G. Li, H. L. Wang, J. G. Zhou, J. Wang, T. Regier and H. J. Dai, Co_3O_4 nanocrystals on graphene as a synergistic catalyst for oxygen reduction reaction, Nat. Mater. 2011, 10, 780-786.

[12] F. Song and X. Hu, Ultrathin cobalt-manganese layered double hydroxide is an efficient oxygen evolution catalyst, J. Am. Chem. Soc., 2014, 136, 16481-16484.

[13] J. Q. Tian, Q. Liu, A. M. Asiri, K. A. Alamry and X. P. Sun, Ultrathin graphitic C_3N_4 nanosheets/graphene composites: efficient organic electrocatalyst for oxygen evolution reaction, ChemSusChem, 2014, 7, 2125-2130.

[14] Q. Liu, J. T. Jin and J. Y. Zhang, $NiCo_2S_4$@graphene as a bifunctional electrocatalyst for oxygen reduction and evolution reactions, ACS Appl. Mater. Interfaces, 2013, 5, 5002-5008.

[15] D. H. Xiong, X. G. Wang, W. Li and L. F. Liu, Facile synthesis of iron phosphide nanorods for efficient and durable electrochemical oxygen evolution, Chem. Commun., 2016, 52, 8711-8714.

[16] M. R. Gao, Q. Gao, Y. F. Xu, Y. R. Zheng, J. Jiang and S. H. Yu, Nitrogen-doped graphene supported $CoSe_2$ nanobelt composite catalyst for efficient water oxidation, ACS Nano, 2014, 8, 3970-3978.

[17] S. Chen, S. S. Thind and A. C. Chen, Nanostructured materials for water splitting-state of the art and future needs: A mini-review, Electrochem. Commun., 2016, 63, 10-17.

[18] X. D. Cui, Z. Q. Xie and Y. Wang, Novel CoS_2 embedded carbon nanocages by direct sulfurizing metal–organic frameworks for dye-sensitized solar cells, Nanoscale, 2016, 8, 11984-11992.

[19] Z. Q. Xie, Z. Y. He, X. H. Feng, W. W. Xu, X. D. Cui, J. H. Zhang, C. Yan, M. A. Carreon, Z. Liu and Y. Wang, Hierarchical sandwich-like structure of ultrafine N-rich porous carbon nanospheres grown on graphene sheets as superior lithium-ion battery anodes, ACS Appl. Mater. Interfaces, 2016, 8, 10324-10333.

[20] W. Cho, Y. H. Lee, H. J. Lee and M. Oh, Systematic transformation of coordination polymer particles to hollow and non-hollow In_2O_3 with pre-defined morphology, Chem. Commun., 2009, 31, 4756-4758.

[21] W. Xia, R. Q. Zou, L. An, D. G. Xia and S. J. Guo, A metal–organic framework route to in situ encapsulation of Co@Co_3O_4@C core@bishell nanoparticles into a highly ordered porous carbon matrix for oxygen reduction, Energy Environ. Sci, 2015, 8, 568-576.

[22] Y. Hou, J. Y. Li, Z. H. Wen, S. M. Cui, C. Yuan and J. H. Chen, Co_3O_4 nanoparticles embedded in nitrogen-doped porous carbon dodecahedrons with enhanced electrochemical properties for lithium storage and water splitting, Nano Energy, 2015, 12, 1-8.

[23] L. T. Yu, J. Liu, X. J. Xu, L. G. Zhang, R. Z. Hu, J. W. Liu, L. C. Yang and M, Zhu Metal-organic framework-derived NiSb alloy embedded in carbon hollow spheres as superior lithium-ion battery anodes, ACS Appl. Mater. Interfaces, 2017, 9, 2516-2525.

[24] X. N. Li, A. I. Rykov, B. Zhang, Y. J. Zhang and J. H. Wang, Graphene encapsulated Fe_xCo_y nanocages derived from metal-organic frameworks as efficient activators for peroxymonosulfate, Catal. Sci. Technol, 2016, 6, 7486-7494.

[25] R. Banerjee, A. Phan, B. Wang, C. Knobler, H. Furukawa, M. O'keeffe and OM. Yaghi, High-throughput synthesis of zeolitic imidazolate frameworks and application to CO_2 capture, Science, 2008, 319, 939-943.

[26] W. W. Xu, Z. Q. Xie, Z. Wang, G. Dietrich and Y. Wang, Interwoven heterostructural Co_3O_4–carbon@FeOOH hollow polyhedrons with improved electrochemical performance, J. Mater. Chem. A, 2016, 4, 19011-19018.

[27] M. J. Hu, B. Lin and S. H. Yu, Magnetic field-induced solvothermal synthesis of one-dimensional assemblies of Ni-Co alloy microstructures, Nano Res., 2008, 1, 303-313.

[28] M. J. Hu, Y. Lu, S. Zhang, S. R. Guo, B. Lin, M. Zheng and S. H. Yu, High yield synthesis of bracelet-like hydrophilic Ni-Co magnetic alloy flux-closure nanorings, J. Am. Chem. Soc, 2008, 130, 11606-11607.

[29] S. Saha and A. K. Ganguli, FeCoNi alloy as noble metal-free electrocatalyst for oxygen evolution reaction (OER), ChemistrySelect, 2017, 2, 1630-1636.

[30] J. H. Wang, W. Cui, Q. Liu, Z. C. Xing, A. M. Asiri, X. P. Sun, Recent progress in cobalt-based heterogeneous catalysts for electrochemical water splitting, Adv. Mater, 2016, 28, 215-230.

[31] Y. R. Zheng, M. R. Gao, Q. Gao, H. H. Li, J. Xu, Z. Y. Wu and S. H. Yu, An efficient $CeO_2/CoSe_2$ nanobelt composite for electrochemical water oxidation, Small, 2015, 11, 182-188.

[32] M. R. Gao, Y. F. Xu, J. Jiang, Y. R. Zheng, S. H. Yu, Water oxidation electrocatalyzed by an efficient $Mn_3O_4/CoSe_2$ nanocomposite, J. Am. Chem. Soc, 2012, 134, 2930–2933.

[33] Z. H. Wen, S. Q. Ci, Y. Hou and J. H. Chen, Facile one-pot, one-step synthesis of a carbon nanoarchitecture for an advanced multifunctonal electrocatalyst, Angew. Chem. Int. Ed, 2014, 53, 6496-6500.

[34] Y. Hou, S. M. Cui, Z. H. Wen, X. R. Guo, X. L. Feng and J. H. Chen, Strongly coupled 3D hybrids of N-doped porous carbon nanosheet/CoNi alloy-encapsulated carbon nanotubes for enhanced electrocatalysis, Small, 2015, 11, 5940-5948.

[35] C. L. Zhang, B. W. Wang, X. C. Shen, J. W. Liu, X. K. Kong, S. C. Chuang, D. Yang, A. G. Dong and Z. M. Peng, A nitrogen-doped ordered mesoporous carbon/graphene framework as bifunctional electrocatalyst for oxygen reduction and evolution reactions, Nano Energy, 2016, 30, 503-510.

[36] G. Q. Han, Y. R. Liu, W. H. Hu, B. Dong, X. Li, X. Shang, Y. M. Chai, Y. Q. Liu and C. G. Liu, Crystallographic structure and morphology transformation of MnO_2 nanorods as efficient electrocatalysts for oxygen evolution reaction, J. Electrochem. Soc, 2016, 163, H67-H73.

[37] M. Li, T. T. Liu, L. Q. Fan, X. J. Bo and L. P. Guo, Three-dimensional hierarchical meso/macroporous Fe/Co-nitrogendoped carbon encapsulated FeCo alloy nanoparticles prepared without any template or surfactant: High-performance bifunctional oxygen electrodes, J. Alloy. Comp, 2016, 686, 467-478.

[38] S. Yoon, J. Y. Yun, J. H. Lim and B. Y. Yoo, Enhanced electrocatalytic properties of electrodeposited amorphous cobalt-nickel hydroxide nanosheets on nickel foam by the formation of nickel nanocones for the oxygen evolution reaction, J. Alloy. Comp, 2017, 693, 964-969.

4.3 Facile Synthesis of MOF-Derived CoNx@Co/Bamboo-Like Carbon Tubes for Efficient Electrocatalytic Water Oxidation

4.3.1 Introduction

The oxygen evolution reaction (OER) plays a crucial role in many renewable energy storage and conversion technologies such as electrocatalytic water splitting, fuel cells and metal-air batteries [1]. Due to its sluggish kinetics and high activation overpotential, tremendous efforts have been made to search for highly efficient and robust electrocatalysts. Noble metals and their oxides (RuO_2, IrO_2) are the mostly used catalysts for OER due to their high catalytic activity and good durability [2,3]. However, the scarcity and high cost impede their practical applications in the global energy system. Therefore, there is a pressing need to develop noble metal-free electrocatalysts with both desirable catalytic activities and reasonable cost for OER application. Over the past years, a variety of noble metal-free electrocatalysts, including transition metal/N-doped carbon hybrids[4], metal oxides [5], sulfides [6], nitrides [7], have been demonstrated electroactive towards the OER process. Among them, transition metal/N-doped carbon nanotube hybrids hold great promise as alternative electrocatalysts in both acidic and alkaline electrolytes due to their unique electronic, structural and mechanical properties [8,9]. Within such hybrids, the transition metal can significantly enhance the electrical conductivity and crystallinity of carbon matrix via catalytic graphitization during synthesis at high temperature, meanwhile the carbon matrix helps to protect the metals from aggregation and corrosion during long-term operation.[10] More importantly, recent studies reveal that foreign heteroatoms (e.g., N) can modify the charge distribution on the carbon surface and induce numerous reactive sites, thereby leading to the enhanced OER catalytic activities [11,12].

The N-doped carbon nanotubes (N-CNTs) have conventionally been synthesized via chemical vapor deposition (CVD) [13], or arc-discharge processes under an NH_3 atmosphere [14]. Despite great progress in their synthesis, these synthetic processes usually require expensive equipment and harsh reaction conditions such as high temperature and careful handling of small molecules (CH_4, C_2H_2, NH_3, etc.), resulting in high cost and high-energy consumption. Instead of using gaseous precursors, solid-phase precursors have recently been explored to obtain N-CNTs under mild conditions. For example, Chen et al. and co-workers reported the synthesis of CoNi/N-CNTs hybrid with a relatively low product yield of ~19 wt.% by direct carbonization of premixed metal salts and urea at 900 ^oC in inert gas [15]. Dai et al. and co-workers synthesized N-CNTs as electrocatalysts for oxygen reduction reaction (ORR) by pyrolysis of the as-prepared conjugated polycarbazoles at 900 ^oC in N_2, followed by NH_3 activation [16]. However, the solid-phase reaction either requires high temperature or complex synthetic process, which greatly hinders their large-scale applications. Overall, the previously reported synthesis strategies of N-CNTs suffer from high cost, low yield and complicated procedures, mainly due to the use of expensive equipment and precursors as well as high temperature. Furthermore, previous studies demonstrate that high-temperature synthesis can result in low N doping level in the CNTs because of the instability of N at high temperature [17,18]. In this context, it is highly desirable to develop a more facile and economical synthesis approach for the synthesis of N-CNTs with high yield, high N doping level and favorable surface structures for electrocatalytic applications.

Metal organic frameworks (MOFs) have emerged as a new precursor for the fabrication of N-CNTs for energy storage and conversion applications. For example, Xu et al. and co-workers synthesized N-doped carbon nanorods from rod-shaped MOFs at 1000 ^oC in Ar, showing superior supercapacitor performance [19]. Lou et al. and co-workers obtained Co/N-CNTs frameworks via pyrolysis of Co-based zeolitic imidazolate frameworks (ZIF-67)

at 700 ^{o}C in the presence of H_2 [20]. The resultant N-CNTs frameworks as OER electrocatalysts show an overpotential of 370 mV at a current density of 10 mA/cm^2 and a small Tafel slope of 93 mV/dec in alkaline medium. More recently, Yang et al. and co-workers reported the synthesis of Ni/N-CNTs by using Ni-based MOFs as precursors at above 700 ^{o}C, showing an overpotential of 460 mV and a Tafel slope of 106 mV/dec [21]. However, few reports of metal/N-CNTs hybrids have demonstrated excellent OER catalytic activities comparable to commercial RuO_2 or IrO_2 catalysts. Therefore, it remains a challenge to optimize MOF-derived metal/N-CNTs catalysts for OER applications. Many recent studies suggest that transition metal-N_x (e.g., CoN_x, FeN_x) species can provide a large number of active sites, and thus demonstrate significantly enhanced electrocatalytic activities towards OER [22, 23, 24]. Moreover, it is generally considered that sufficient pyridinic N and graphitic N dopants in carbon have positive impact on the OER process, mainly attributed to the altered charge density of the N-doped carbon matrices.[25,26] Despite these recent achievements, it still lacks simple but effective methodology to synthesize electrocatalysts with sufficient targeted active sites such as CoN_x species, topological defects (e.g., edge sites), pyridinic and/or graphitic N dopants.

In this project, a simple and scalable synthesis of MOF-derived CoN_x@Co/N-doped carbon tubes hybrids (denoted as CoN_x@Co/NCT hereinafter) is developed via one-step pyrolysis of ZIF-67 at a low temperature of 650 ^{o}C with the introduction of urea, which serves as both nitrogen source and promoter of carbon tube growth. The as-obtained CoN_x@Co/NCT hybrid exhibits bamboo-like tubular structure with high density of active sites originated from CoN_x species, high nitrogen doping level and topological defects, rendering excellent electrocatalytic activities towards OER in alkaline medium. As a result, the as-obtained CoN_x@Co/NCT hybrid shows significantly enhanced OER performance, which outperforms most noble metal-free electrocatalysts and even commercial IrO_2. Therefore, the integration of more active species CoN_x and increased N doping level in carbon tube is an efficient way to optimize the OER performance of MOF-derived metal/N-CNTs catalysts. We believe that this work may provide new insights into the unitization of metal-N_x species and N dopants in metal/N-CNTs hybrids and promote their potential large-scale application in energy conversion and storage.

4.3.2 Experimental

Synthesis of ZIF-67 polyhedrons

1.92 g 2-methylimidazole was dissolved in mixed solvents of methanol (20 mL) and ethanol (20 mL). Then, 1.746 g $Co(NO_3)_2{\cdot}6H_2O$ was dissolved in another mixed solvents of methanol (20 mL) and ethanol (20 ml) [27]. After stirring for 10 minutes, the above two solutions were mixed and stirred constantly for 12 hours at 25 ^{o}C. The purple products were collected by centrifugation, washed with ethanol three times, and dried at 80 ^{o}C for 12 hours in air.

Synthesis of CoN_x@Co/NCT

The as-prepared ZIF-67 polyhedrons and urea powders were put into two separate porcelain boats with urea powders at the upstream side of the furnace. Afterwards, the Co@NCT products were obtained by annealing at 650 ^{o}C for 5 h in a static Ar atmosphere, followed by post-acid washing for 12 h in 0.5 M H_2SO_4. The black products were collected by centrifugation, washed with ethanol three times, and dried at 60 ^{o}C for 12 hours in vacuum.

Materials characterizations

The crystalline structures of the as-obtained products were identified by using X-ray diffraction (XRD) technique, and the data were recorded at a constant scanning rate of 2 ^{o}/min on a Rigaku MiniFlex X-ray diffractometer (Cu Kα radiation). The microstructures and morphologies of samples were characterized by using scanning electron microscope (SEM). The SEM imaging was carried out on a FEI Quanta 3D FEG FIB/SEM, which is equipped with energy-dispersive X-ray spectroscopy (EDS).

Electrochemical measurements

To investigate the performance of the as-obtained electrocatalysts, the samples were dipped on Ni foam with a loading amount of 0.2 mg/cm^2. The electrochemical measurements were performed by using a CHI 760D electrochemical workstation (CH Instruments, Inc.). The platinum and Hg/HgO electrode were used as counter electrode and reference electrode, respectively. The measured potentials vs. Hg/HgO were converted to reversible hydrogen electrode (RHE). The oxygen evolution reaction (OER) properties of the as-prepared catalysts were studied using linear sweep voltammetry (LSV) and cyclic voltammetry (CV). The potential was swept at a scan rate of 5 mV/s in N_2-saturated 1M KOH aqueous solution. The electrochemical impedance spectroscopy (EIS) measurements were carried out in the frequency range from 10^5 Hz to 0.01 Hz using an electrochemical workstation (CHI 6504C). To study the electrochemical stability of the as-prepared electrocatalysts, the cyclic voltammetry was carried out at a scan rate of 100 mV/s.

4.3.3 Results and Discussion

The overall synthesis process of CoN_x@Co/NCT hybrid is schematically illustrated in Figure 4.3.1. First, the purple ZIF-67 polyhedrons are prepared via a precipitation method by using cobalt nitrite as metal source and 2-methylimidazole as organic linkers at room temperature. Subsequently, through one-step annealing treatment of ZIF-67 particles and urea at 650 ^{o}C in Ar, the black CoN_x@Co/NCT hybrid is obtained. It should be noted that a post-acid treatment is performed in 0.5 M H_2SO_4 for 12 h to remove any accessible Co particles within the CoN_x@Co/NCT hybrid. Urea here plays a critical role in promoting the formation of N-doped carbon tubes. During the annealing treatment, decomposition of urea releases strong reducing gas NH_3, which can reduce cobalt ions within ZIF-67 framework to metallic cobalt catalysts. Simultaneously, the organic linkers can serve as both carbon and nitrogen sources, which are catalyzed into N-doped bamboo-like carbon tubes with the assistance of cobalt catalysts. Furthermore, NH_3 resulted from decomposition of urea can not only provide additional nitrogen source to further increase the N doping level of carbon tubes but also promote the formation of CoN_x species on the surface of Co particles, which are beneficial for boosting the OER performance. It is worth mentioning that the N-doped carbon tubes can be formed at the temperature of as low as 650 ^{o}C in the presence of low-cost urea instead of gaseous reducing agents (e.g., H_2 or NH_3). Such facile synthesis method is different from all previous reports of metal/N-doped carbon hybrids obtained from direct carbonization of various MOFs under an inert atmosphere.

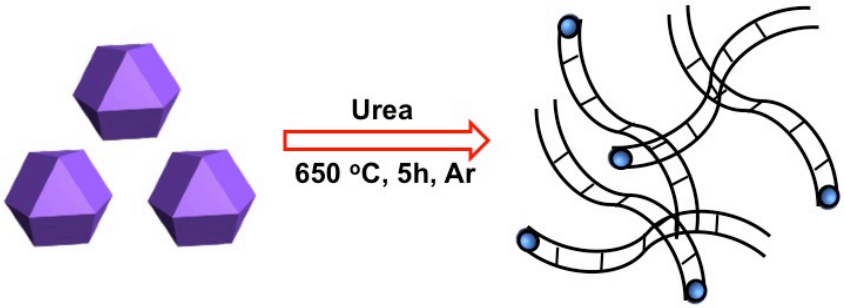

Figure 4.3.1 Schematic illustration of the synthesis of Co particles embedded in N-doped bamboo-like carbon tubes (CoN_x@Co/NCT hybrid).

The crystal structures of the as-obtained ZIF-67 polyhedrons and MOF-derived CoN_x@Co/NCT hybrid are first identified by XRD analysis. As shown in Figure 4.3.2a, the black XRD pattern of ZIF-67 shows major diffraction peaks from (001), (002), (112) and (222) planes, which are well consistent with previous reports [28] As seen from the red XRD pattern of CoN_x@Co/NCT hybrid, the relative sharp diffraction peak at about 26.3° corresponds to the C(002) plane, suggesting that carbon is crystalline in nature. The other well-defined diffraction peaks at 44.3°, 51.5° and 76.0° match well with (111), (200) and (220) planes of the face-centered cubic (fcc) metallic Co (PDF No. 15-0806), respectively. Moreover, no characteristic XRD peaks of CoN_x can be found in CoN_x@Co/NCT hybrid, which is probably due to its ultralow amount in the sample. However, the existence of CoN_x in the hybrid is revealed by XPS analysis presented further in the manuscript. Thus, the XRD results reveal that the annealing of ZIF-67 at 650 °C in the presence of urea can completely convert pure ZIF-67 particles into metallic Co/carbon hybrid.

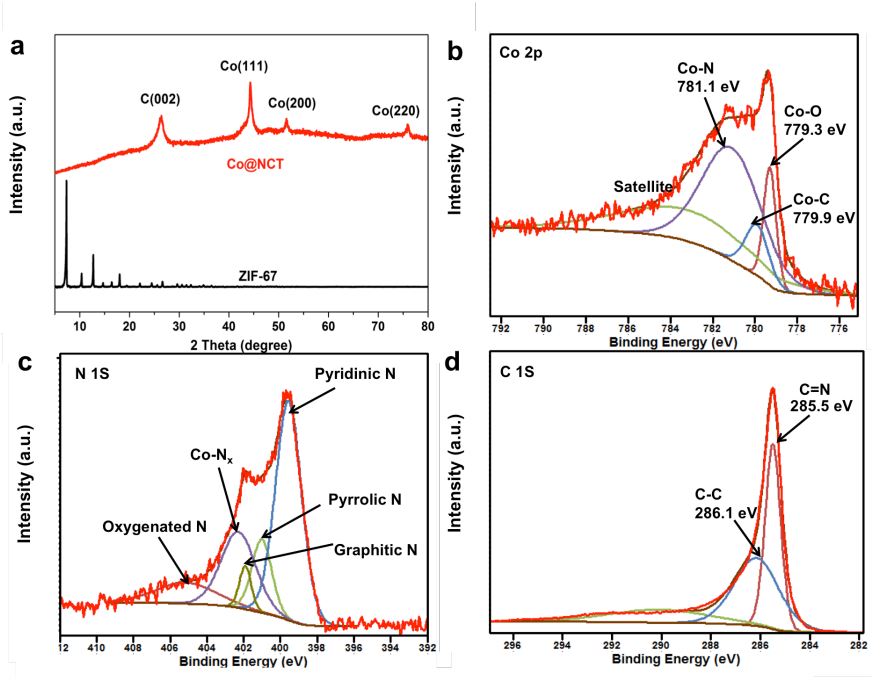

Figure 4.3.2 (a) XRD patterns of ZIF-67 polyhedrons and ZIF-67 derived CoN_x@Co/NCT hybrid, (b) high-resolution XPS spectra of (b) Co 2p, (c) N 1s, and (d) C 1s, respectively.

To study surface chemical composition of CoN_x@Co/NCT hybrid, XPS measurements are carried out for the elemental profile analysis in the region of 0-1200 eV. Figure 4.3.2b-d exhibit survey and high-resolution XPS spectra of Co 2p, N 1s, and C 1s, respectively. The XPS survey reveals the presence of C, N, Co and O elements. The existence of O element is due to the formation of CoO_x species on the surface of metallic Co particle, probably resulted from exposure of samples to air. The quantitative surface atomic percentages of C, N and Co elements in CoN_x@Co/NCT hybrid are 93.33, 5.87 and 0.80%, respectively. Figure 4.3.2b shows that high-resolution XPS spectrum of Co 2p is deconvoluted into three peaks, CoO_x (779.3 eV), CoN_x (781.1 eV) and Co-C (779.9 eV), which is consistent with previous reports [29]. By calculating the area under the fitted curve, we can conclude the atomic concentrations of CoO_x and CoN_x species are 10.9 and 49.5%, respectively. Several recent studies have demonstrated that both CoO_x and CoN_x can serve as highly active sites for electrocatalytic reactions [30-32]. The formation of CoN_x species is probably due to the reaction between NH_3 released from decomposition of urea and surface of metallic Co at 650 ^oC in Ar. The high-resolution XPS spectrum of N 1s in Figure 4.3.2c can be deconvoluted into five peaks located at 399.5, 401.0, 401.9, 402.3 and 405.1 eV, which correspond to pyridinic N, pyrrolic N, graphitic N, CoN_x and oxygenated N, respectively. The atomic concentrations of pyridinic N, graphitic N are 49.48 and 4.40%, respectively, among all N. It is expected that these pyridinic N and graphitic N in carbon can provide numerous active sites, thereby favoring the OER catalytic activities. As seen from the high-resolution XPS of C 1s in Figure 4.3.2d, the peak at 285.5 eV corresponds to the C=N bonding, further confirming successful N doping into CoN_x@Co/NCT hybrid. Furthermore, the XPS analysis reveals that the total atomic percentage of N dopant in CoN_x@Co/NCT hybrid is about 5.87%, which is much higher than that of previously reported Co/N-CNTs frameworks obtained from pyrolysis of ZIF-67 at 700 ^oC in the presence of H_2 (2.4%) [35]. Thus, our work shows that urea can serve as an ideal N source to increase the N doping level of metal/N-CNTs hybrid, which is expected to boost the catalytic activities for OER applications.

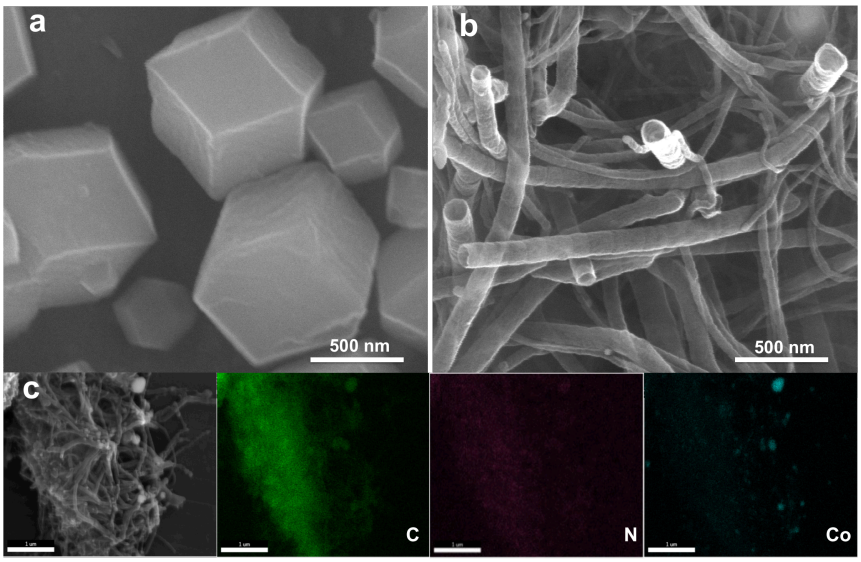

Figure 4.3.3 The SEM images of (a) ZIF-67 polyhedrons, (b) ZIF-67 derived CoN_x@Co/NCT hybrid, and (c) the corresponding EDS mapping of C, N and Co elements (scale bars = 1 μm).

To study the structure and morphology change of ZIF-67 polyhedrons and ZIF-67 derived CoN_x@Co/NCT hybrid, the SEM images are taken and displayed in Figure 4.3.3a and b. From the SEM image in Figure 4.3.3a, it is clearly observed that ZIF-67 particles possess well-defined polyhedron-like morphology and have the particle size ranging from 300~800 nm. After one-step annealing treatment at 650 ^{o}C in Ar, numerous carbon tubes are formed. The diameter of the carbon tubes is estimated to be in the range of 30 to ~150 nm with several microns in length. It is interesting to note that one end of carbon tubes is closed, but the other end is open. In Figure 4.3.3c, the SEM-EDS mapping results indicate relatively uniform distribution of C, N and Co elements in CoN_x@Co/NCT hybrid. The EDS elemental analysis shows the atomic percentages of C, N and Co are 59.0, 32.8 and 8.2%, respectively. As discussed in the XPS analysis above, the N is successfully doped in the hybrid, forming the CoN_x species and N-doped carbon tubes. Such high N content in the hybrid is mainly attributed to the following two reasons. First, the organic linkers within MOF and urea as additional N precursor can provide rich N sources for the formation of N-doped product. Second, the low-temperature synthesis (650 ^{o}C) in this work is believed to reduce the loss of N source during the formation of CoN_x@Co/NCT hybrid, and thus leads to higher N content in our product than that in the N-doped carbons reported previously. To our knowledge, this is one of the highest N doping level achieved for N-doped carbon materials compared to most of previous reports [36, 37].

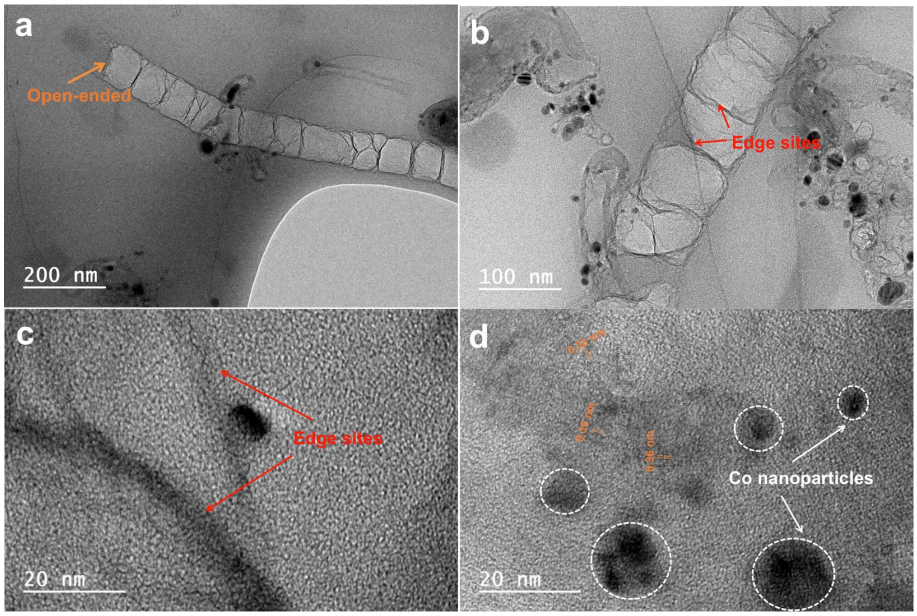

Figure 4.3.4 The TEM images of CoN_x@Co/NCT hybrid. Red arrows in (b, c) indicate the edges sites on bamboo-like carbon tubes. In (d), 0.36 nm corresponds to the lattice spacing on the C (002) plane, indicated by the gold dashed lines.

To better visualize the nanostructure of CoN_x@Co/NCT hybrid, TEM characterization is carried out. As seen from Figure 4.3.4a and b, the formation of bamboo-like carbon tubes is confirmed. The diameter of carbon tubes can be as large as above 100 nm. Some CNTs with small diameter of about 30 nm are also observed. As shown in Figure 4a, the carbon tube is open-ended, which is consistent with previous SEM observation. Furthermore, numerous rumpled ridges are formed on the surface of carbon tubes, as displayed in Figure 4.3.4b and c. Previous studies suggest that these ridge sites can provide a large number of active sites for OER [38, 39]. Moreover, such bamboo-like tubular structure with large tube diameter can enhance the mass transfer during the electrocatalytic reactions, and thus improve the reaction kinetics during electrocatalytic reactions. In Figure 4.3.4d, Co nanoparticles with a particle size of 10~20 nm are embedded within the carbon matrix. The

above XRD, XPS, SEM-EDS and TEM analyses all clearly confirm the successful formation of CoN_x@Co/NCT hybrid with targeted active sites such as CoN_x species, pyridinic and graphitic N dopants, and desirable structural properties.

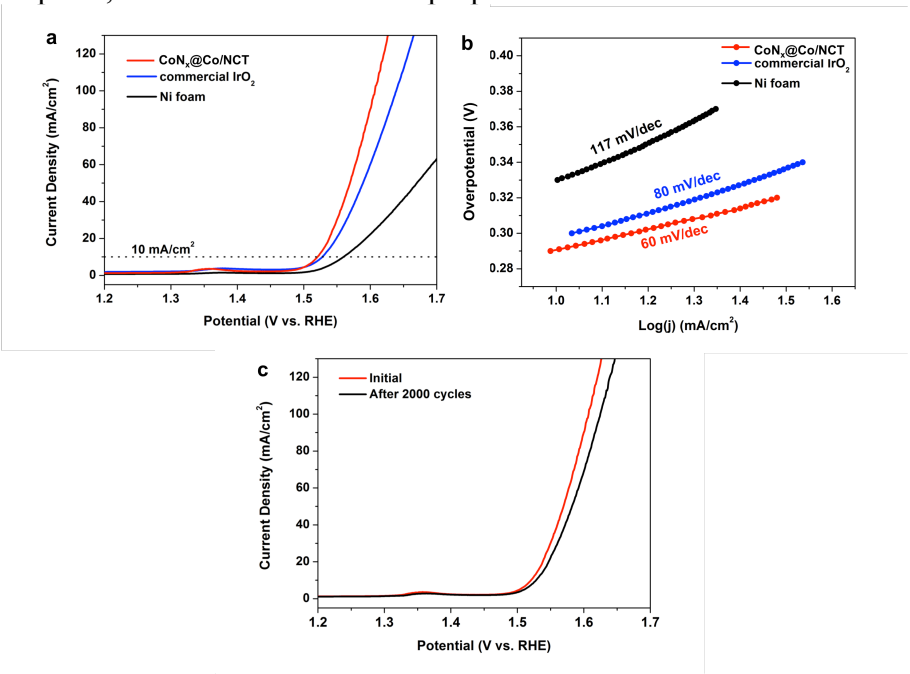

Figure 4.3.5 (a) Linear sweep voltammetry curves, (b) Tafel plots of CoN_x@Co/NCT, commercial IrO_2 and Ni foam recorded at a scanning rate of 5 mV/s in 1 M KOH solution for OER, and (c) LSV polarization curves of CoN_x@Co/NCT before and after 2000 CV cycles. The recorded data were iR-corrected using the solution resistance as measured by EIS at the open-circuit potential.

In order to evaluate the electrocatalytic activities of the as-obtained product, linear sweep voltammetry (LSV) tests are carried out in 1 M KOH electrolyte with the CoN_x@Co/NCT hybrid supported on Ni foam as the working electrode. All the measured potentials vs. Hg/HgO are converted to reversible hydrogen electrode (RHE). For comparison purpose, commercial IrO_2 catalyst and bare Ni foam are studied under the same condition. As shown in Figure 4.3.5a, the CoN_x@Co/NCT hybrid supported on Ni foam exhibits an onset potential as low as 1.47 V versus RHE, which is even lower than that of commercial IrO_2 catalyst (1.48 V) and Ni foam (1.49 V). To examine the catalytic activity, the potential at the current density of 10 mA/cm^2 is usually used as an indicator. As a result, CoN_x@Co/NCT hybrid only requires a potential of 1.52 V versus RHE to reach the current density of 10 mA/cm^2, while commercial IrO_2 catalyst requires 1.53 V and Ni foam requires 1.57 V. Based on the equation of overpotential ($\eta=E_{RHE}$-1.23), the required overpotential of CoN_x@Co/NCT hybrid is as low as 290 mV at 10 mA cm^{-2}, which is about 10 and 50 mV ahead of commercial IrO_2 (300 mV) and bare Ni foam (340 mV), respectively.

The OER kinetics of the as-obtained electrocatalysts is further investigated by the Tafel plots derived from LSV polarization curves, according to Tafel equation $\eta = b\log(j)$, where η is the overpotential, b is the Tafel slope, j is the current density (Figure 4.3.5b). The CoN_x@Co/NCT hybrid display much smaller Tafel slope of 60 mV/dec in comparison with IrO_2 (80 mV/dec) and bare Ni foam (117 mV/dec). The smallest Tafel slope of CoN_x@Co/NCT hybrid reveals a shortened charge transfer length and more facile charge transfer at the catalyst/electrolyte interface, thereby leading to fast catalytic reaction kinetics for OER. In addition to intrinsic catalytic activity, long-term durability of electrocatalysts is another critical issue for practical application in energy conversion systems. Thus,

accelerated cyclic voltammetry measurements of CoN_x@Co/NCT hybrid are conducted for up to 2000 cycles. As shown in Figure 4.3.5c, even after 2000 CV cycles, the catalyst shows a very similar LSV polarization curve with the initial one. A small potential shift of ~10 mV is observed at a current density of 40 mA/cm^2, demonstrating good stability of CoN_x@Co/NCT hybrid in an alkaline medium.

Such excellent OER performance outperforms commercial IrO_2 and most recently reported OER catalysts. The high catalytic activity and durability of CoN_x@Co/NCT hybrid can be attributed to the following reasons: (i) Highly active CoN_x species formed on the surface of Co particles can provide numerous active sites toward OER. (ii) Rich pyridinic and graphitic N dopants in carbon not only function as active sites for electrocatalytic reactions but also enhance the electrical conductivity of carbon matrices. (iii) Bamboo-like carbon tubes can reduce the mass and charge transfer resistance and the many ridges on their surface can also serve as active sites for OER. (iv) The interaction of Co nanoparticles with NCT is believed to reduce the work function at surfaces of carbon tubes, making carbon tube surface more active.

4.3.4 Conclusions

In conclusion, we demonstrate a facile strategy for scalable synthesis of MOF-derived CoN_x@Co/NCT hybrid via one-step pyrolysis of ZIF-67 at low temperature with the introduction of urea. Here urea functions as both nitrogen source and promoter of carbon tube growth. The as-obtained CoN_x@Co/NCT hybrid possesses highly active CoN_x species, rich pyridinic and graphitic N dopants, numerous ridge sites on the surface of bamboo-like carbon tubes, which can efficiently optimize the OER performance by offering a large number of active sites and enhancing the mass and charge transfer for fast reaction kinetics. With many desirable benefits in composition, morphology and structure, the resultant CoN_x@Co/NCT hybrid shows an overpotential as low as 290 mV at 10 mA cm^{-2} with a small Tafel slope of 60 mV/dec, which exceeds most noble metal-free electrocatalysts for OER. Therefore, the CoN_x@Co/NCT hybrid holds great promise for efficient electrocatalytic water oxidation applications.

4.3.5 References

[1] M. G. Walter, E. L. Warren, J. R. Mckone, S. W. Boettcher, Q. Mi, E. A. Santori and N. S. Lewis, Solar water splitting cells. Chem. Rev., 2010, 110, 6446-6473.

[2] T. R. Cook, D. K. Dogutan, S. Y. Reece, Y. Surendranath, T. S. Teets and D. G. Nocera, Solar energy supply and storage for the legacy and nonlegacy worlds. Chem. Rev., 2010, 110, 6474-6502.

[3] H. Dau, C. Limberg, T. Reier, M. Risch, S. Roggan and P. Strasser, The mechanism of water oxidation: from electrolysis via homogeneous to biological catalysis. ChemCatChem, 2010, 2, 724-761.

[4] M. Gong, Y. Li, H. Wang, Y. Liang, J. Z. Wu, J. Zhou, J. Wang, T. Regier, F. Wei and H. Dai, An advanced Ni–Fe layered double hydroxide electrocatalyst for water oxidation. J. Am. Chem. Soc., 2013, 135, 8452-8455.

[5] J. Suntivich, K. J. May, H. A. Gasteiger, J. B. Goodenough and Y. Shao-Horn, A perovskite oxide optimized for oxygen evolution catalysis from molecular orbital principles. Science, 2011, 334, 1383-1385.

[6] S. W. Lee, C. Carlton, M. Risch, Y. Surendranath, S. Chen, S. Furutsuki, A. Yamada, D. G. Nocera and Y. Shao-Horn, The nature of lithium battery materials under oxygen evolution reaction conditions. J. Am. Chem. Soc., 2012, 134, 16959-16962.

[7] W. Hu, Y. Q. Wang, X. H. Hu, Y. Q. Zhou and S. L. Chen, Three-dimensional ordered macroporous IrO_2 as electrocatalyst for oxygen evolution reaction in acidic medium. J. Mater. Chem., 2012, 22, 6010-6016.

[8] Y. Tan, C. Xu, G. Chen, X. Fang, N. Zheng and Q. Xie, Facile synthesis of manganese-oxide-containing mesoporous nitrogen-doped carbon for efficient oxygen reduction. Adv. Funct. Mater., 2012, 22, 4584-4591.

[9] C. Jin, F. Lu, X. Cao, Z. Yang and R. Yang, Facile synthesis and excellent electrochemical properties of $NiCo_2O_4$ spinel nanowire arrays as a bifunctional catalyst for the oxygen reduction and evolution reaction. J. Mater. Chem. A, 2013, 1, 12170-12177.

[10] Y. Li, P. Hasin and Y. Wu, $Ni_xCo_{3-x}O_4$ nanowire arrays for electrocatalytic oxygen evolution. Adv. Mater., 2010, 22, 1926-1929.

[11] B. S. Yeo and A. T. Bell, Enhanced activity of gold-supported cobalt oxide for the electrochemical evolution of oxygen. J. Am. Chem. Soc., 2011, 133, 5587-5593.

[12] S. R. Mellsop, A. Gardiner and A. T. Marshall, Electrocatalytic oxygen evolution on electrochemically deposited cobalt oxide films: comparison with thermally deposited films and effect of thermal treatment. Electrocatalysis, 2014, 5, 445-455.

[13] B. Cui, H. Lin, J.-B. Li, X. Li, J. Yang and J. Tao, Core–ring structured $NiCo_2O_4$ nanoplatelets: synthesis, characterization, and electrocatalytic applications. Adv. Funct. Mater., 2008, 18, 1440-1447.

[14] J. Masa, P. Weide, D. Peeters, I. Sinev, W. Xia, Z. Sun, C. Somsen, M. Muhler, W. Schuhmann, Amorphous cobalt boride (Co_2B) as a highly efficient nonprecious catalyst for electrochemical water splitting: oxygen and hydrogen evolution. Adv. Energy Mater. 2016, 6, 1502313.

[15] T. Ma, J. Cao, M. Jaroniec, S. Qiao, Interacting carbon nitride and titanium carbide nanosheets for high-performance oxygen evolution. Angew. Chem., Int. Ed. 2016, 55, 1138-1142.

[16] S. Chen, J. Duan, A. Vasileff, S. Qiao, Size Fractionation of two-dimensional sub-nanometer thin manganese dioxide crystals towards superior urea electrocatalytic conversion. Angew. Chem. 2016, 128, 3868-3872.

[17] H. X. Zhong, J. Wang, Y. W. Zhang, W. L. Xu, W. Xing, D. Xu, Y. F. Zhang, and X. B. Zhang, ZIF-8 derived graphene-based nitrogen-doped porous carbon sheets as highly

efficient and durable oxygen reduction electrocatalysts. Angew. Chem., Int. Ed. 2014, 53, 14235-14239.

[18] F. C. Zheng, Y. Yang, and Q. W. Chen, High lithium anodic performance of highly nitrogen-doped porous carbon prepared from a metal-organic framework. Nat. commun. 2014, 5, 5261.

[19] G. Chen, T. Ma, Z. Liu, N. Li, Y. Su, K. Davey, S. Qiao, Efficient and stable bifunctional electrocatalysts Ni/Ni_xM_y (M= P, S) for overall water splitting. Adv. Funct. Mater. 2016, 26, 3314-3323.

[20] M.-R. Gao, X. Cao, Q. Gao, Y.-F. Xu, Y.-R. Zheng, J. Jiang, S.-H. Yu, Nitrogen-doped graphene supported $CoSe_2$ nanobelt composite catalyst for efficient water oxidation. ACS Nano 2014, 8, 3970-3978.

[21] S. Chen, S. S. Thind, and A. Chen, Nanostructured materials for water splitting-state of the art and future needs: A mini-review. Electrochem commun. 2016, 63, 10-17.

[22] J.-L. Ma, D. Bao, M.-M. Shi, J.-M. Yan, X.-B. Zhang, Reversible nitrogen fixation based on a rechargeable lithium-nitrogen battery for energy storage. Chem. 2017, 2, 525-532.

[23] G. A. Ferrero, K. Preuss, A. Marinovic, A. B. Jorge, N. Mansor, D. J. L. Brett, A. B. Fuertes, M. Sevilla, M.-M. Titirici, Fe–N-doped carbon capsules with outstanding electrochemical performance and stability for the oxygen reduction reaction in both acid and alkaline conditions. ACS Nano 2016, 10, 5922-5932.

[24] S. Chen, J. J. Duan, A. Vasileff, S. Z. Qiao, Size, Size fractionation of two-dimensional sub-nanometer thin manganese dioxide crystals towards superior urea electrocatalytic conversion. Angew. Chem. 2016, 55, 3804-3808.

[25] M. Gong, Y. Li, H. Wang, Y. Liang, J. Z. Wu, J. Zhou, J. Wang, T. Regier, F. Wei and H. Dai, An advanced Ni–Fe layered double hydroxide electrocatalyst for water oxidation. J. Am. Chem. Soc., 2013, 135, 8452-8455.

[26] M.-R. Gao, X. Cao, Q. Gao, Y.-F. Xu, Y.-R. Zheng, J. Jiang, S.-H. Yu, Nitrogen-doped graphene supported $CoSe_2$ nanobelt composite catalyst for efficient water oxidation. ACS Nano 2014, 8, 3970-3978.

[27] D. Kong, H. Wang, Z. Lu, Y. Cui, $CoSe_2$ nanoparticles grown on carbon fiber paper: an efficient and stable electrocatalyst for hydrogen evolution reaction. J. Am. Chem. Soc. 2014, 136, 4897-4900.

[28] Z. Zhang, X. Wang, K. Wu, Y. Yue, M. Zhao, J. Cheng, J. Ming, C. Yu, X. Wei, $Co_{0.85}Se$ bundle-like nanostructure catalysts for hydrogenation of 4-nitrophenol to 4-aminophenol. New J. Chem. 2014, 38, 6147-6151.

[29] Z. Wang, Q. Sha, F. Zhang, J. Pu, W. Zhang, Synthesis of polycrystalline cobalt selenide nanotubes and their catalytic and capacitive behaviors. CrystEngComm, 2013, 15, 5928-5934.

[30] Y. Z. Chen, C. Wang, Z. Y. Wu, Y. Xiong, Q. Xu, S. H. Yu, H. L. Jiang, From

bimetallic metal-organic framework to porous carbon: high surface area and multicomponent active dopants for excellent electrocatalysis. Adv. Mater. 2015, 27, 5010-5016.

[31] H. H. Zhong, Y. Luo, S. He, P. G. Tang, D. Q. Li, N. A. Vante, and Y. J. Feng. Electrocatalytic cobalt nanoparticles interacting with nitrogen-doped carbon nanotube in situ generated from a metal–organic framework for the oxygen reduction reaction. ACS Appl. Mater. Interfaces, 2017, 9, 2541-2549

[32] S. Dou, C. L. Dong, Z. Hu, Y. C. Huang, J. I. Chen, L. Tao, D. F. Yan, D. W. Chen, S. H. Shen, S. L. Chou, S. Y. Wang. Atomic-scale CoO_x species in metal–organic frameworks for oxygen evolution reaction. Adv. Funct. Mater. 2017, 27, 1702546.

[33] H. Hu, B. Y. Guan, B. Y. Xia, X. W. Lou, Designed formation of $Co_3O_4/NiCo_2O_4$ double-shelled nanocages with enhanced pseudocapacitive and electrocatalytic properties. J. Am. Chem. Soc. 2015, 137, 5590-5595.

[34] Y. Zheng, Y. Jiao, Y. Zhu, L. H. Li, Y. Han, Y. Chen, A. J. Du, M. Jaroniec, S. Z. Qiao, Hydrogen evolution by a metal-free electrocatalyst. Nat. Commun. 2014, 5, 3783.

[35] B. Li, Y. Chen, X. Ge, J. Chai, X. Zhang, T. A. Hor, G. Du, Z. Liu, H. Zhang, Y. Zong, Mussel-inspired one-pot synthesis of transition metal and nitrogen co-doped carbon (M/N–C) as efficient oxygen catalysts for Zn-air batteries. Nanoscale 2016, 8, 5067-5075.

[36] B. S. Yeo and A. T. Bell, Enhanced activity of gold-supported cobalt oxide for the electrochemical evolution of oxygen. J. Am. Chem. Soc., 2011, 133, 5587-5593.

[37] G. A. Ferrero, K. Preuss, A. Marinovic, A. B. Jorge, N. Mansor, D. J. L. Brett, A. B. Fuertes, M. Sevilla, M.-M. Titirici, Fe–N-doped carbon capsules with outstanding electrochemical performance and stability for the oxygen reduction reaction in both acid and alkaline conditions. ACS Nano 2016, 10, 5922-5932.

[38] H.-F. Wang, C. Tang, B. Wang, B.-Q. Li, Q. Zhang, Bifunctional Transition Metal Hydroxysulfides: Room-temperature sulfurization and their applications in Zn–Air batteries. Adv. Mater. 2017, 29, 1702327.

[39] W. Liu, M. S. Song, B. Kong, Y. Cui, Flexible and stretchable energy storage: recent advances and future perspectives. Adv. Mater. 2017, 29, 1603436.

CHAPTER 5. METAL-ORGANIC FRAMEWORKS AS HIGH-PERFORMANCE ABSORBENTS FOR HEAVY METAL REMOVAL FROM WASTEWATER*

5.1 Introduction

In the above three chapters, metal-organic frameworks derived nanostructures have been developed to address the current challenges in energy-related applications including LIBs, DSSCs and electrocatalytic water splitting. With the rapid increase of industrial and human activities, disposal of industrial wastewater has become one of the most important environmental issues worldwide [1,2]. Heavy metal pollution has posed a severe threat to environment and public health since heavy metals are not biodegradable and prone to accumulate in the environment. In addition, most of heavy metal ions even with low concentrations are dangerous and extremely toxic to human health. For example, high concentration of Cu^{2+} in public drinking water systems will result in serious diseases such as cramps, diarrhea, gastrointestinal catarrh and damage of liver and kidney [3-5]. In this chapter, water-stable zeolitic imidazolate framework (ZIF-8) nanocrystals synthesized at room temperature are evaluated for highly efficient removal of copper ions from aqueous systems due to its high surface area and large porosity. The possible adsorption mechanism is explored for the first time using various characterization techniques, such as scanning electron microscopy (SEM), transmission electron microscopy (TEM), Fourier transform infrared spectroscopy (FTIR), X-ray photoelectron spectroscopy (XPS) and X-ray diffraction (XRD).

Up to date, various approaches, such as chemical precipitation [6,7], ion exchange [8], membrane filtration [9], and adsorption [10-12], have been reported for heavy metal wastewater treatment. Among them, adsorption has been considered as an economic and effective approach for heavy metal wastewater treatment benefiting from its flexibility and simplicity of design, low operation cost and good adsorption capability. Furthermore, adsorption is partially reversible, and thus adsorbents sometimes can be recovered by proper desorption process. Among the available adsorbents, activated carbon (AC) and carbon nanotubes (CNTs) have been widely reported as promising adsorbents in the removal of heavy metal ions [13-17]. However, the adsorption capacities of metal ions by AC and CNTs are very low and the whole adsorption process usually takes several hours or even longer. Furthermore, both AC and CNTs are expensive, which further hinders their practical applications in heavy metal wastewater treatment. Recently, various nanosized metal oxides (NMOs) [18-22], such as nanosized Fe_3O_4, Fe_2O_3, TiO_2 and CeO_2, have be studied as promising alternatives for removal of heavy metal ions from aqueous systems owing to their high specific surface areas and high activities resulted from the so-called size-quantization effect. Nevertheless, NMOs tend to agglomerate owing to their high surface energy; thus adsorption capacity of NMOs would be significantly decreased. Therefore, it is highly challenging but extremely desirable to develop low-cost adsorbents with both high efficiency and high adsorption capacity for practical applications in removal of heavy metals from industrial wastewater.

Metal organic frameworks (MOFs), as typical inorganic-organic hybrid crystalline solids with well-defined nanoporous structures, have been extensively applied for wide applications in gas separation [23], sensors [24], catalysis [25], and drug delivery [26], thanks to their high surface area and large porosity. In recent years, MOFs have drawn more and

* Reprinted with permission from Yujie Zhang, Zhiqiang Xie, Zhuqing Wang, Xuhui Feng, Ying Wang, and Aiguo Wu, Unveiling the adsorption mechanism of zeolitic imidazolate framework-8 with high efficiency for removal of copper ions from aqueous solutions. Dalton Trans., 2016, 45, 12653-12660. Copyright 2016 The Royal Society of Chemistry.

more attention as new adsorbents for the applications in heavy metal wastewater treatment. For example, metal-organic framework $Cu_3(BTC)_2$ with thio/thiol-functional groups have been reported for efficient removal of both mercury and lead ions [27]. Cu-based MOF $Cu_3(BTC)_2$ with sulfonic acid functional groups demonstrated high adsorption capability and selectivity of cadmium ions in water [28]. Zr-based MOFs were also reported for selective removal of Cu^{2+} over Ni^{2+} in water [29]. However, the aforementioned MOFs were mainly prepared using hydro/solvothermal, sonochemical and microwave methods, which generally require time-consuming process, expensive equipment and/or high temperature procedure. Furthermore, surface functionalization of MOFs with specific functional groups is usually needed for removal of heavy metal ions, which requires complicated, tedious processes and very careful control of reaction conditions such as concentration of the reactants and pH value in the solutions, posing big challenges for potential large-scale production of high efficient adsorbents.

In this project, water-stable zeolitic imidazolate framework (ZIF-8) nanocrystals synthesized at room temperature are tested for highly efficient removal of copper ions from aqueous systems. As a result, ZIF-8s demonstrate unexpectedly high removal efficiency and high adsorption capacities of Cu^{2+} over other heavy metal ions. The possible adsorption mechanism is explored for the first time using various characterization techniques, such as scanning electron microscopy (SEM), transmission electron microscopy (TEM), Fourier transform infrared spectroscopy (FTIR), X-ray photoelectron spectroscopy (XPS) and X-ray diffraction (XRD).

5.2 Experimental

All the analytical reagent-grade chemicals were purchased from Sinopharm Chemical Reagent Co., Ltd. (Shanghai, China) without further purification. Aqueous solution of Cu (1000 mg L^{-1}) was prepared by dissolving $Cu(NO_3)_2$ in deionized water. Other concentrations were prepared by successively diluting the initial solution. The pH of the solutions was adjusted by using NaOH or HCl. Milli-Q water (18.2 MΩ.cm)was used throughout the experiments.

Synthesis of ZIF-8 crystals

ZIF-8 crystals were prepared as follows: First, 0.81 g 2-methyimidazole was mixed with 25 mL methanol; after the solid was totally dissolved in the solvent, 0.7 g $Zn(NO_3)_2{\cdot}6H_2O$ with 25 mL methanol was added into the solution. The mixture was stirred for 5 h. The solid was collected by centrifuging the mixture at 3000 rpm for 10 min and washed with methanol for at least three times. The collected solid was then dried at 75^{o}C overnight.

Adsorption test

In a typical adsorption test, ZIF-8 was first ground into powder, and then 30 mg ZIF-8 was added into 90 mL aqueous solution containing Cu^{2+}. The mixture was treated with ultra-sonication for 2 min and stirred for 30 min, and then separated by using needle filter with pore diameter of 200 microns. The rest of heavy metals in the aqueous systems was detected and analyzed via ICP-OES. It should be noted that all the reported data for adsorption tests in this work were the average of at least three replicates for each experiment.

Characterizations

The concentration of heavy metallic ions was determined using an inductively coupled plasma optical emission spectrometer (ICP-OES, PE Optima 2100DV, Perkin-Elmer, USA). Gas sorption analyses were conducted via Quantachrome Instruments Autosorb-iQ (Boynton Beach, Florida USA) with extra-high pure nitrogen. Transmission electron microscope (TEM) images were recorded on a JEOL 2100 instrument (JEOL, Japan) with an acceleration voltage of 200 kV. For TEM analysis, the samples were prepared by drop casting the dispersions onto carbon-coated copper grids, which were air-dried subsequently. Fourier transform infrared spectroscopy (FTIR) data were collected in the wavenumber ranging from 4000 to 400 cm^{-1} on Nicolet 6700 fourier-transform infrared spectrometer using KBr pellets. X-ray photoelectron spectrometer (XPS) was carried out using an AXIS Ultra DLD instrument with Mg Kα radiation as the X-ray source and all the binding energies were referenced to C 1s peak at 284.8 eV The phase structure of ZIF-8 before and after adsorption was analyzed on an X-ray diffractometer (XRD, D8 Advance, Bruker AXS, Germany). The morphology and chemical distribution of the samples were conducted using a field emission scanning electron microscope (FESEM) (TM-1000, Hitachi, Japan). For XPS, SEM and XRD analysis, the samples were prepared by drop casting the dispersions onto silicon pellet (for XPS and SEM) and glass plate (for XRD), which were subsequently dried in a closed dryer.

5.3 Results and discussion

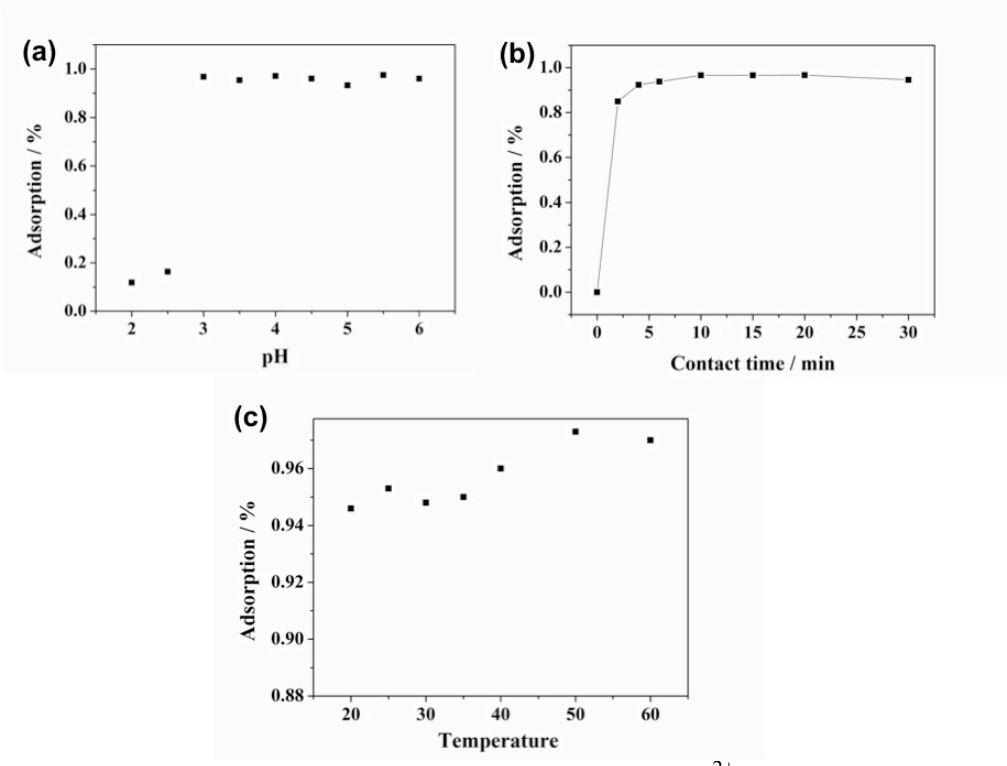

Figure 5.1 Effect of pH, contact time and temperature on Cu^{2+} adsorption by ZIF-8 (initial Cu^{2+} concentration: 120 mg L^{-1}, 120 mg L^{-1}, 150 mg L^{-1}, respectively)

Effect of pH

One of the major factors affecting the Cu^{2+} adsorption capacity and removal efficiency is the pH value of the solutions, since pH may not only change the speciation of metal ions, but also influence structural stability and surface charges of the adsorbent.

Therefore, 30 mL Cu^{2+} solution (120 mg L^{-1}) with the pH range of 2 to 6 is prepared, the adsorption time and temperature are fixed at 1 hour and 25 °C respectively. The effect of pH on the adsorption property of ZIF-8 for Cu^{2+} is investigated as shown in Figure 5.1a. The adsorption quantity increases significantly with the increase of pH value from 2.5 to 3, and remains unchanged with further increase of pH of the solution. It is found that only less than 20% Cu^{2+} is adsorbed when the pH of solutions is below 3. It might be attributed to protonation of the amino moiety of ZIF-8, which reduces the coordination ability between nitrogen atom and Cu^{2+} [30]. It might also be due to the unstability of ZIF-8 under strong acid condition. When the pH value is increased from 3 to 6, the adsorption quantity almost remains constant, indicating that pH does not affect the adsorption property of ZIF-8 under these conditions. However, when pH is higher than 6, precipitation of cupric hydroxide may be formed with higher concentration of Cu^{2+} (the Ksp of $Cu(OH)_2$ is 2.2×10^{-20}) [30]. Therefore, the adsorption experiments are not investigated when pH is higher than 6. Finally, pH is optimized from 4 to 5, and ZIF-8 remains stable within this range. Moreover, neither protonation of amine moiety nor precipitation of cupric hydroxide occurrs, which is beneficial to the adsorption of Cu^{2+}. To further study the stability of pure ZIF-8 sample in acid solutions, we tested and analyzed the concentrations of Zn^{2+} release in various aqueous solutions with different pH values using the inductively coupled plasma optical emission spectrometry (ICP-OES) technique. It is found that there is almost no Zn^{2+} release at pH 5-6, indicating that ZIF-8 is very stable in such a weak acid solution. Even in a strong acid solution at pH 3-4, only less than 10% of Zn^{2+} release occurs. However, in a stronger acid solution at pH 2, a high percentage of Zn^{2+} release (57%) is observed, suggesting that ZIF-8 would decompose in such a strong acid solution. Such results are consistent with the adsorption performances of ZIF-8 on the Cu^{2+} removal in aqueous solutions with pH values ranging from 2 to 6.

Effect of contact time

The effect of contact time on the adsorption property of ZIF-8 is investigated in a solution with pH of 4 at 25 °C. As displayed in Figure 5.1b, the rate of adsorption is very fast. The uptake of Cu^{2+} by ZIF-8 is 85% within 2 min, and reaches 95% in less than 10 min. The high adsorption rate of ZIF-8 is likely due to the high specific surface area of ZIF-8 (1340 m^2 g^{-1}) and a large number of amino moiety on the surface of ZIF-8 [31]. To the best of our knowledge, such impressive adsorption efficiency is much higher than existing adsorbents for removal of Cu^{2+} from aqueous systems [32-34]. In order to make sure the adsorption completed with higher Cu^{2+} concentration, the contact time of 30 min is chosen.

Effect of temperature

Adsorption test is carried out in a range of 20-60 ^{o}C with the pH of 4, and the adsorption time and Cu^{2+} concentration are fixed at 30 min and 150 mg L^{-1} respectively. The effect of temperature on Cu^{2+} adsorption by ZIF-8 is shown in Figure 5.1c, from which we can observe that adsorption quantity is almost the same from 20 to 35 ^{o}C and increased with the further increase of temperature from 35 to 50 ^{o}C, indicating that the adsorption process is an endothermic adsorption reaction.

Effect of initial Cu^{2+} concentration

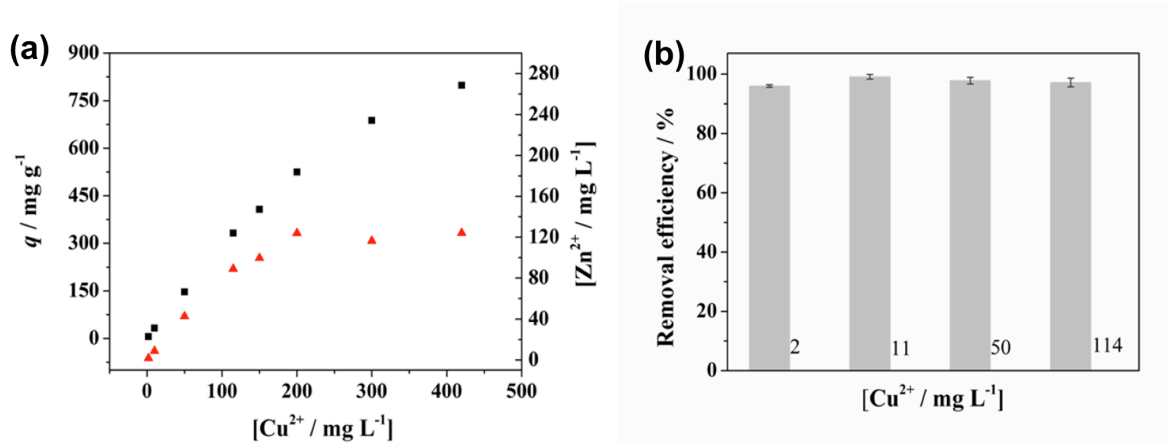

Figure 5.2 Effect of Cu^{2+} concentration on q value of ZIF-8(a, black), the release of Zn^{2+}(a, red) and removal efficiency of Cu^{2+} (b)

In order to determine the maximum adsorption capacity of ZIF-8, 10 mg ZIF-8 is equilibrated with 30 mL Cu^{2+} solutions with concentrations ranged from 2 to 420 mg L^{-1} for 30 min. The results in Figure 5.2a show that the amount of Cu^{2+} adsorbed per unit mass of ZIF-8 (q, mg g^{-1}) is increased with the increase of the initial concentration of Cu^{2+}. The obtained q value reaches approximately 800 mg g^{-1} when the initial concentration of Cu^{2+} is 420 mg L^{-1}, which is higher than most of other adsorbents [30,35,36]. In order to ascertain the reason for the unexpected high q value, the solution after adsorption is analyzed in details and release of Zn^{2+} is found. From Figure 5.2a, we can see that the release amount of Zn^{2+} increases with the increase of Cu^{2+} concentration and then remains constant until the Cu^{2+} concentration is more than 200 mg L^{-1}, which may reveal that Zn^{2+} in ZIF-8 has been completely replaced by Cu^{2+}. However, the q value of ZIF-8 increases continually as Cu^{2+} concentration increases from 200 to 420 mg L^{-1}, which is likely due to the coordination reaction between Cu^{2+} and nitrogen atom on 2-methyimidazole.[5] Under optimal experimental conditions (time = 30 min, pH = 4), when the initial concentration of Cu^{2+} is 114 mg L^{-1}, the removal efficiency of Cu^{2+} is up to 97.2% (Figure 5.2b). Moreover, when the initial concentration of Cu^{2+} is 2 mg L^{-1}, the removal efficiency is up to 96% and the rest concentration of Cu^{2+} is 0.085 mg L^{-1}, which is much lower than the maximum allowed concentration of Cu^{2+} in drinking water defined by the US EPA (1.3 mg L^{-1}). These results demonstrate that the as-prepared ZIF-8 is applied to treat wastewater with both high and low concentration, which is an important indicator for good adsorbents.

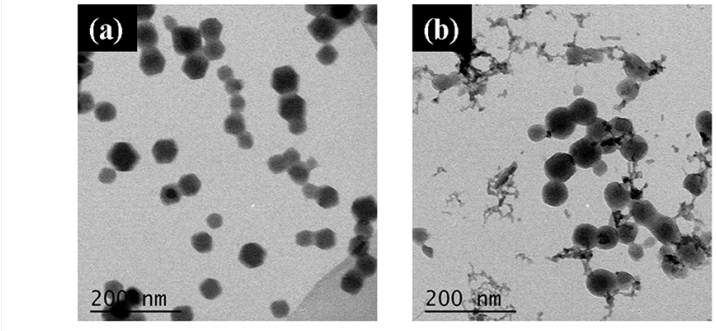

Figure 5.3 TEM images of ZIF-8 (a) before and (b) after adsorption (Cu^{2+} concentration of 150 mg L^{-1})

Investigation of mechanism of adsorption

TEM analysis

The structure of ZIF-8 before and after adsorption is characterized by TEM as shown in Figure 5.3. Before adsorption, ZIF-8 is a hexagonal structure with a particle size of 30 - 70 nm (Figure 5.3a). However, after reacting with Cu^{2+} solution, the hexagonal structure is destroyed. The edges of the adsorbent become smoother and new material with smaller size is formed. According to the adsorption data, structural change of ZIF-8 after Cu^{2+} adsorption can be presumably due to the ion exchange between Cu^{2+} and Zn^{2+}.

FTIR analysis

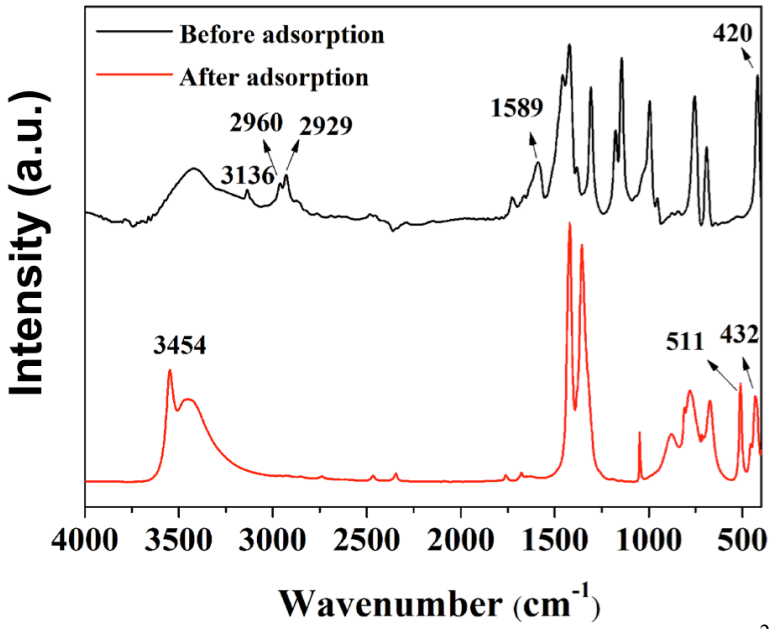

Figure 5.4 FTIR spectra of ZIF-8 (a) before and (b) after adsorption (Cu^{2+} concentration of 150 mg L^{-1})

The FTIR spectra of ZIF-8 before and after adsorption of Cu^{2+} are shown in Figure 5.4. The spectra for ZIF-8 are analyzed as follows: C-N stretching on the imidazole rings, 3136 cm^{-1}; C-H stretching of $-CH_3$, 2960 and 2929 cm^{-1}; the C=N stretching, 1589 cm^{-1}; Zn-N stretching, 420 cm^{-1}. After reacting with Cu^{2+} solutions, a new peak is observed at 511 cm^{-1}, which should be contributed to Cu-N stretching, indicating that Cu^{2+} has been connected onto ZIF-8 through ion exchange or coordination reaction.

XPS analysis

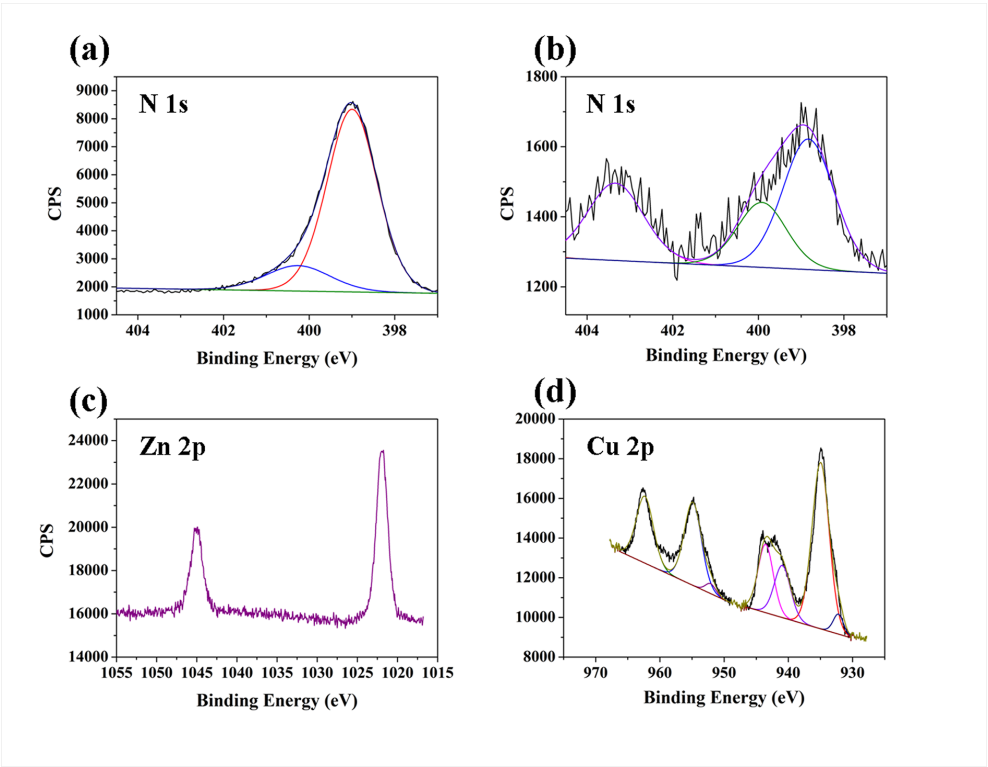

Figure 5.5 N XPS spectrum of the sample before (a) and after (b) adsorption, Zn (c) and Cu (d) XPS spectrum of the sample after adsorption (Cu^{2+} concentration of 150 mg L^{-1})

XPS analysis is also used to investigate the state change of ZIF-8 before and after adsorption of Cu^{2+} (Figure 5.5). The binding energy for N 1s in ZIF-8 is about 399 and 400.3 eV, corresponding to C-N and C=N in 2-methylimidazole, respectively. After reacting with Cu^{2+} solution, the two peaks of N 1s for 2-methylimidazole still exist, and a new peak at ~403.4 eV appears, due to the coordination reaction between nitrogen atom and Cu^{2+}. Moreover, the peaks for Zn 2p with the binding energy of 1022 and 1045 eV still exist after adsorption of Cu^{2+}, which means that the structure of ZIF-8 is partialy preserved under this condition. The peaks for Cu 2p appear after adsorption, demonstrating that Cu^{2+} has been adsorbed onto ZIF-8.

XRD analysis

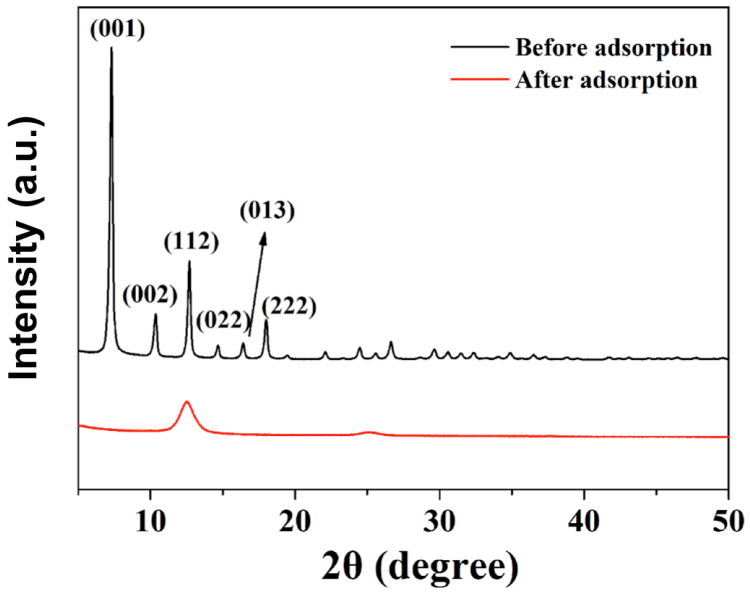

Figure 5.6 Powder X-ray diffraction patterns of ZIF-8 before and after adsorption.

In order to explore the reaction product when Zn^{2+} in ZIF-8 is replaced by Cu^{2+} completely, the Cu^{2+} concentration of 300 mg L^{-1} is used in the adsorption experiment and powder X-ray diffraction experiments are carried out to study the phase and structure of ZIF-8 before and after adsorption, as shown in Figure 5.6. The major sharp diffraction peaks are presented in the case of ZIF-8, which is similar to the data published in other articles,[31] indicating that the as-prepared ZIF-8 is a single pure phase without impurity. However, after reacting with Cu^{2+} solution, almost all of the peaks for ZIF-8 disappear, and a wide peak with 2θ at about 12.6° is presented, which means the structure of ZIF-8 has been completely changed by Cu^{2+} and new complex formed. In addition, it is found that after white ZIF-8 powders are added into the colorless aqueous solution containing Cu^{2+}, the solution turns blue, which further confirms the likely formation of copper complex.

SEM-EDS mapping analysis

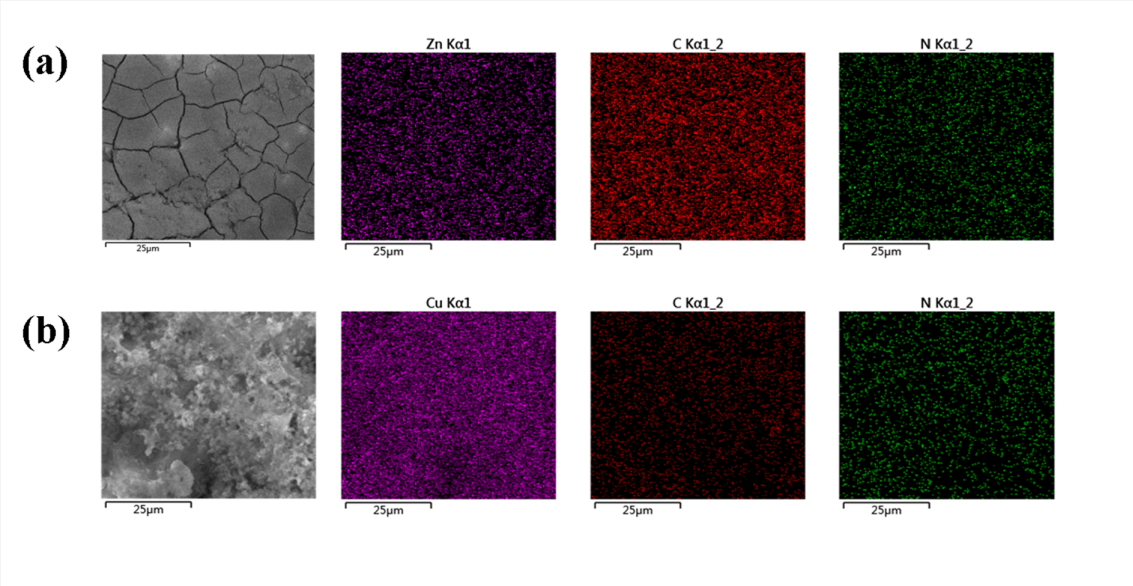

Figure 5.7 SEM-EDS mapping of ZIF-8 (a) before adsorption and (b) after adsorption.

The distribution of elements for ZIF-8 before and after adsorption is also analyzed by SEM-EDS mapping. As displayed in Figure 5.7a. we can see that ZIF-8 is made up of carbon, nitrogen and zinc, and these three kinds of elements distributed adequately in ZIF-8. However, as shown in Figure 5.7b, after reacting with Cu^{2+} solution, zinc element dissappears, and copper elements appear in the solid, indicating that Zn^{2+} is replaced by Cu^{2+} completely. And a small amount of Cl and O elements appear, possibly due to the pH regulation of the solutions and the formation of cupric hydroxide, respectively.

The adsorption mechanism

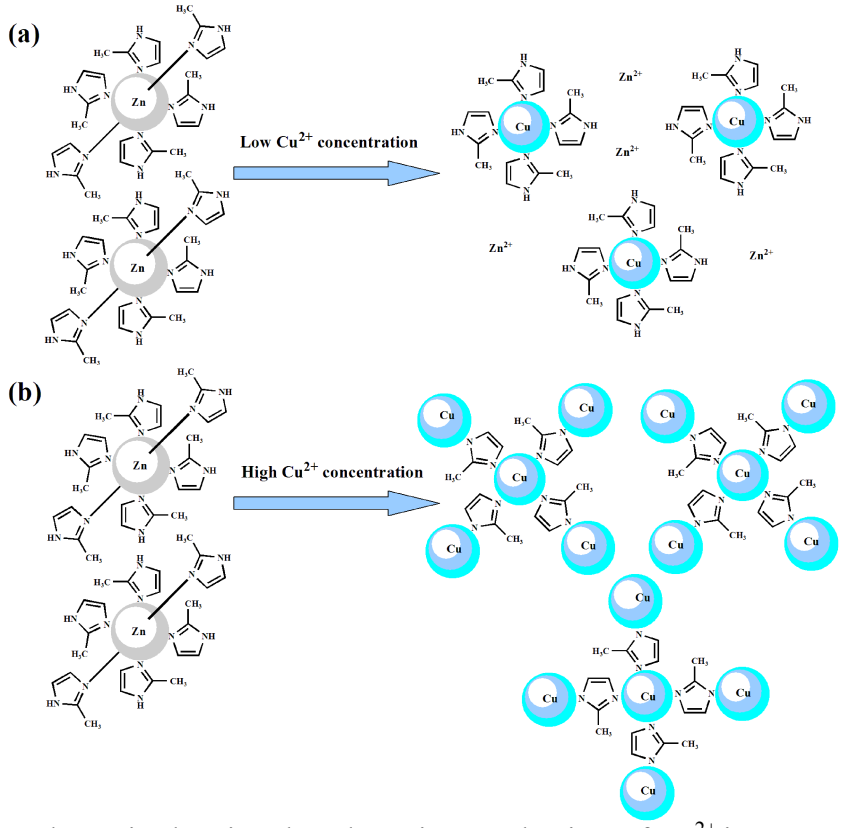

Figure 5.8 The schematic showing the adsoprtion mechanism of Cu^{2+} in aqueous solutions by ZIF-8 nanocrystals. (a) Ion exchange reaction at low concentration of Cu^{2+}; (b) Coordination reaction between Cu^{2+} and nitrogen atom on 2-methylimidazole at high concentration of Cu^{2+}.

From the adsorption data and various characterization results, we can deduce a adsorption mechanism for our work (Figure 5.8). During the adsortpion process of Cu^{2+}, Zn^{2+} in ZIF-8 is replaced by Cu^{2+} and new complex is formed. The reasons are: (1) Due to the similar atomic radius between Zn and Cu, Zn^{2+} in ZIF-8 can be easily replaced by Cu^{2+}; (2) The valence electron layer structure of Zn^{2+} is more stable than that of Cu^{2+}, thus the chemical coordination ability of Cu^{2+} is stronger than that of Zn^{2+} [37]. After Zn^{2+} is replaced by Cu^{2+} completely, as shown in Scheme1a, the adsorption amount per unit mass of ZIF-8 continuely increases due to the coordination reaction between Cu^{2+} and nitrogen atom on 2-methylimidazole, as shown in Scheme 1b. Therefore, the adsorption process of Cu^{2+} by ZIF-8 involves ion exchange when the concentration of Cu^{2+} is lower than 200 mg L^{-1} and coordination reaction when the concentration of Cu^{2+} is higher than 200 mg L^{-1}.

5.4 Conclusions

In this study, ZIF-8 nanocrystals are synthesized at room temperature and used as adsorbent for removal of Cu^{2+} from aqueous solutions. It is found that: (i) pH shows little effect on the adsorption of ZIF-8 when the pH of the solution is between 3 and 6. (ii) ZIF-8 exhibits fast kinetics for highly efficient removal Cu^{2+} with an adsorption time of less than 30 min. (iii) ZIF-8 demonstrates high adsorption capacities of Cu^{2+}, about 800 mg g^{-1}, when the initial concentration of Cu^{2+} is 420 mg L^{-1}. (iv) ZIF-8 demonstrates high removal efficiency with both high and low concentration of Cu^{2+}. (v) The adsorption mechanism contains the ion exchange process and coordination reaction.

5.5 References

[1] L. Chabaane, S. Tahiri, A. Albizane, M. El Krati, M. L. Cervera and M. de la Guardia, Immobilization of vegetable tannins on tannery chrome shavings and their use for the removal of hexavalent chromium from contaminated water. Chem. Eng. J., 2011, 174, 310-317.

[2] R. Dutta, S. S. Mohammad, S. Chakrabarti, B. Chaudhuri, S. Bhattacharjee and B. K. Dutta, Reduction of hexavalent chromium in aqueous medium with zerovalent iron. Water Environ. Res., 2010, 82, 138-146.

[3] M. Ajmal, R. A. K. Rao and M. A. Khan, Adsorption of copper from aqueous solution on Brassica cumpestris (mustard oil cake). J. Hazard. Mater., 2005, 122, 177-183.

[4] S. Larous, A. H. Meniai and M. B. Lehocine, Experimental study of the removal of copper from aqueous solutions by adsorption using sawdust. Desalination, 2005, 185, 483-490.

[5] N. Bakhtiari, S. Azizian, S. M. Alshehri, N. L. Torad, V. Malgras and Y. Study on adsorption of copper ion from aqueous solution by MOF-derived nanoporous carbon. Yamauchi, Micropor. Mesopor. MAT., 2015, 217, 173-177.

[6] Q. Y. Chen, Z. Luo, C. Hills, G. Xue and M. Tyrer, Precipitation of heavy metals from wastewater using simulated flue gas: sequent additions of fly ash, lime and carbon dioxide. Water Res., 2009, 43, 2605-2614.

[7] M. Gharabaghi, M. Irannajad and A.R. Azadmehr, Selective sulphide precipitation of heavy metals from acidic polymetallic aqueous solution by thioacetamide. Ind. Eng. Chem. Res., 2012, 51, 954-963.

[8] M. Y. Vilensky, B. Berkowitz and A. Warshawsky, In situ remediation of groundwater contaminated by heavy-and transition-metal ions by selective ion-exchange methods. Environ. Sci. Technol., 2002, 36, 1851-1855.

[9] S. M. C. Ritchie, K. E. Kissick, L. G. Bachas, S. K. Sikdar, C. Parikh and D. Bhattacharyya, Polycysteine and other polyamino acid functionalized microfiltration membranes for heavy metal capture. Environ. Sci. Technol., 2001, 35, 3252-3258.

[10] R. Celis, M. C. Hermosin and J. Cornejo, Heavy metal adsorption by functionalized clays. Environ. Sci. Technol., 2000, 34, 4593-4599.

[11] U. Wingenfelder, C. Hansen, G. Furrer and R. Schulin, Removal of heavy metals from mine waters by natural zeolites, Environ. Sci. Technol., 2005, 39, 4606-4613.

[12] G. Yuvaraja, M. V. Subbaiah and A. Krishnaiah, Caesalpinia bonducella Leaf Powder as Biosorbent for Cu(II) Removal from Aqueous Environment: Kinetics and Isotherms. Ind. Eng. Chem. Res., 2012, 51, 11218-11225.

[13] M. Kobya, E. Demirbas, E. Senturk and M. Ince, Adsorption of heavy metal ions from aqueous solutions by activated carbon prepared from apricot stone. Bioresource Technol., 2005, 96, 1518-1521.

[14] K. Kadirvelu, C. Faur-Brasquet and P. Le Cloirec, Removal of Cu (II), Pb (II), and Ni (II) by adsorption onto activated carbon cloths. Langmuir, 2000,16, 8404-8409.

[15] C. Y. Lu, and H. S. Chiu, Adsorption of zinc (II) from water with purified carbon nanotubes. Chem. Eng. Sci., 2006, 61, 1138-1145.

[16] C.S. Lu, H. Chiu and C. T. Liu, Removal of zinc (II) from aqueous solution by purified carbon nanotubes: kinetics and equilibrium studies. Ind. Eng. Chem. Res., 2006, 45, 2850-2855.

[17] Y. H. Li, S. G. Wang, Z. K. Luan, J. Ding, C. L. Xu and D. H. Wu, Adsorption of cadmium (II) from aqueous solution by surface oxidized carbon nanotubes. Carbon, 2003, 41, 1057-1062.

[18] L. S. Zhong, J. S. Hu, H. P. Liang, A. M. Cao, W. G. Song and L. J. Wan, Self-Assembled 3D flowerlike iron oxide nanostructures and their application in water treatment. Adv. Mater., 2006, 18, 2426-2431.

[19] T. Phuengprasop, J. Sittiwong and F. Unob, Removal of heavy metal ions by iron oxide coated sewage sludge. J. Hazard. Mater., 2011, 186, 502-507.

[20] Z. X. Jin, H. Y. Gao and L. H. Hu, Removal of Pb (II) by nano-titanium oxide investigated by batch, XPS and model techniques. RSC Adv., 2015, 5, 88520-88528.

[21] L. S. Zhong, J. S. Hu, A. M. Cao, Q. Liu, W. G. Song and L. J. Wan, 3D flowerlike ceria micro/nanocomposite structure and its application for water treatment and CO removal. Chem. Mater., 2007, 19, 1648-1655.

[22] L. S. Zhong, J. S. Hu, L. J. Wan and W. G. Song, Facile synthesis of nanoporous anatase spheres and their environmental applications. Chem. Commun., 2008, 10, 1184-1186.

[23] M. P. Suh, H. J. Park, T. K. Prasad and D. W. Lim, Hydrogen storage in metal–organic frameworks. Chem. Rev., 2012, 112, 782-835.

[24] L. E. Kreno, K. Leong, O. K. Farha, M. Allendorf, R. P. Van Duyne and J. T. Hupp, Metal–organic framework materials as chemical sensors. Chem. Rev., 2012, 112, 1105-1125.

[25] A. M. Shultz, O. K. Farha, J. T. Hupp and S. T. Nguyen, A catalytically active, permanently microporous MOF with metalloporphyrin struts. J. Am. Chem. Soc., 2009, 131, 4204-4205.

[26] P. Horcajada, R. Gref, T. Baati, P. K. Allan, G. Maurin, P. Couvreur, G. Ferey, R. E. Morris, C. Serre, Metal–organic frameworks in biomedicine. Chem. Rev., 2012, 112, 1232-1268.

[27] F. Ke, L. G. Qiu, Y. P, Yuan, F. M, Peng, X, Jiang, A. J, Xie, Y. H, Shen, and J. F, Zhu, Thiol-functionalization of metal-organic framework by a facile coordination-based postsynthetic strategy and enhanced removal of Hg^{2+} from water. J. Hazard Mater., 2011, 196, 36-43.

[28] Y. Wang, G. Q. Ye, H. H. Chen, X. Y. Hu, Z. Niu and S. Q. Ma, Functionalized metal–organic framework as a new platform for efficient and selective removal of cadmium (II) from aqueous solution. J. Mater. Chem ., 2015, 3, 15292-15298.

[29] Y. Zhang, X, Zhao, H, Huang, Z. Li, D, Liu, and C, Zhong, Selective removal of transition metal ions from aqueous solution by metal–organic frameworks. RSC Adv, 2015. 5, 72107-72112.

[30] Z. Q. Wang, M. Wang, G. H. Wu, D. Y. Wu and A. G. Wu, Colorimetric detection of copper and efficient removal of heavy metal ions from water by diamine-functionalized SBA-15. Dalton T., 2014, 43, 8461-8468.

[31] L. Zhang, G. Qian, Z. J. Liu, Q. Cui, H. Y. Wang, H. Q. Yao, Sep. Adsorption and separation properties of n-pentane/isopentane on ZIF-8. Purif. Technol., 2015, 156, 472-479.

[32] C. G. Lee, J. W Jeon, M. J. Hwang, K. H. Ahn, C. Park, J. W. Choi and S. H. Lee, Lead and copper removal from aqueous solutions using carbon foam derived from phenol resin. Chemosphere, 2015, 130, 59-65.

[33] L. Trakal, R. Sigut, H. Sillerova, D. Faturikova and M. Komarek, Arab. Copper removal from aqueous solution using biochar: effect of chemical activation. J. Chem., 2014, 7, 43-52.

[34] M. R. Awual, A novel facial composite adsorbent for enhanced copper (II) detection and removal from wastewater. Chem. Eng. J., 2015, 266, 368-375.

[35] S. T. Yang, Y. L Chang, H. F. Wang, G. B. Liu, S. Chen, Y. W. Wang, Y. F. Liu and A. N. Cao, Folding/aggregation of graphene oxide and its application in Cu^{2+} removal. J. Colloid Interf. Sci., 2010, 351, 122-127.

[36] M. A. Tofighy and T. Mohammadi, Adsorption of divalent heavy metal ions from water using carbon nanotube sheets. J. Hazard. Mater., 2011, 185, 140-147.

[37] V. S. Mummidivarapu, S. Bandaru, D. S. Yarramala, K. Samanta, D. S. Mhatre, and C. P. Rao, Binding and Ratiometric Dual Ion Recognition of Zn^{2+} and Cu^{2+} by 1,3,5-Tris-amidoquinoline Conjugate of Calixarene by Spectroscopy and Its Supramolecular Features by Microscopy. Anal. Chem., 2015, 87, 4988-4995.

CHAPTER 6. CONCLUSIONS

This dissertation presents six research projects on exploration of metal-organic frameworks derived nanomaterials with desirable structures, morphologies and compositions for energy and environmental applications. In brief, the first two projects are focused on synthesis of ZIF-8 derived N-doped porous carbon and ZIF-67 derived ultrafine Co_3O_4 nanoparticles/carbon nanotubes as high-performance anode materials for Li-ion batteries. The third project is to synthesize CoNi alloy embedded carbon nanocages by using bimetallic organic frameworks as precursors/templates for dye-sensitized solar cells (DSSCs). In addition, MOFs-derived CoNi and CoNx@Co/N-doped carbon tubes as low-cost electrocatalysts are synthesized and evaluated for efficient oxygen evolution reaction (OER). The last project is to study ZIF-8 as an efficient absorbent for removal of Cu ions from water. The conclusions from these projects are as follows:

A sandwich-like, graphene-based porous nitrogen-doped carbon (PNCs@Gr) has been prepared through facile pyrolysis of zeolitic imidazolate framework nanoparticles in situ grown on graphene oxide (GO) (ZIF-8@GO). Such sandwichlike nanostructure can be used as anode material in lithium ion batteries, exhibiting remarkable capacities, outstanding rate capability, and cycling performances that are some of the best results among carbonaceous electrode materials and exceed most metal oxide-based anode materials derived from metal orgainc frameworks (MOFs). Apart from a high initial capacity of 1378 mAh g^{-1} at 100 mA g^{-1}, this PNCs@Gr electrode can be cycled at high specific currents of 500 and 1000 mA g^{-1} with very stable reversible capacities of 1070 and 948 mAh g^{-1} to 100 and 200 cycles, respectively. At a higher specific current of 5000 mA g^{-1}, the electrode still delivers a reversible capacity of over 530 mAh g^{-1} after 400 cycles, showing a capacity retention of as high as 84.4%. Such an impressive electrochemical performance is ascribed to the ideal combination of hierarchically porous structure, a highly conductive graphene platform, and high-level nitrogen doping in the sandwich-like PNCs@Gr electrode obtained via in situ synthesis.

Cobalt oxides are attractive high-capacity anode materials in lithium ion batteries yet suffer from fast capacity fading and low rate capability. To overcome these challenges, well-dispersed ZIF-67 derived cobalt oxide nanoparticles encapsulated within a flexible single-walled carbon nanotubes matrix (marked as Co_3O_4 NPs@SWCNT) has been syntheized, for the first time, through a facile evaporation-induced self-assembly (EISA) of singlewalled carbon nanotubides (SWCNTDs). By varying the loading amount of Co_3O_4 content in the composite, the optimal Co_3O_4 NPs@SWCNT exhibits a high capacity of 1286 mAh g^{-1} after 140 cycles at 100 mA g^{-1}. Such impressive electrochemical properties are mainly ascribed to the synergic effect of Co_3O_4 nanoparticles and SWCNTs in the heterostructure, in which the robust SWCNTs not only offer excellent strain accommodation of the encapsulated Co_3O_4 upon long-term cycling, but also significantly enhance overall electric conductivity and mechanical stability of the electrodes.

The commercialization of dye-sensitized solar cells (DSSCs) has been severely hindered by high cost and scarcity of Pt as counter electrode (CE) materials. To synthesize low-cost Pt-free CE materials with ideal combination of high electrical conductivity, excellent catalytic activity, as well as satisfactory long-term electrochemical stability, a new synthesis approach has been developed to prepare CoNi@carbon nanotubes embedded carbon nanocages (CoNi@CNTs-C) as a low-cost CE in DSSCs for the first time, by applying Co/Ni bimetallic metal organic framework (MOF) as the template. It is found that the DSSC efficiency can be maximized by simply optimizing the ratio of Ni^{2+}/Co^{2+} precursor concentration during the synthesis. As a result, the DSSC based on the CE of CoNi@CNTs-C-200 with a Co/Ni atomic ratio of 9:1 exhibits optimal performance with a remarkable

power conversion efficiency (PCE) of 9.04%, showing ~15% overall PCE enhancement compared to Pt CE (7.88%). Notably, the CoNi@CNTs-C-200 CE also demonstrates excellent long-term electrochemical stability over 300 cyclic voltammetry cycles, which is even superior to that of conventional Pt CE.

The major challenge of electrocatalytic water splitting for hydrogen production is the sluggish kinetics of oxygen evolution reaction (OER). A facile synthesis has been developed to obtain CoNi alloy embedded carbon nanocages through one-step annealing treatment of bimetallic organic frameworks as the precursors for application as efficient and economical electrocatalysts for OER. As a result, the optimized CoNi-C-200 sample with a Co/Ni atomic ratio of 9:1 exhibits a low overpotential of 408 mV at a current density of 10 mA cm^{-2}. Moreover, it shows an excellent long-term stability during 5000 CV sweeps. Such improved performance can be attributed to the unique morphology and the synergistic effects of CoNi alloy nanoparticles and conductive carbon matrix in the composite.

In addition to CoNi alloy embedded carbon nanocages, a simple and scalable synthesis has been developed to obtain CoN_x@Co/N-doped carbon tubes hybrid. The resultant CoN_x@Co/NCT hybrid exhibits bamboo-like structure with high density of active sites originated from abundant CoN_x species, high nitrogen doping level and topological defects, rendering excellent electrocatalytic activities towards OER in alkaline medium. As a result, the as-obtained CoN_x@Co/NCT hybrid shows an overpotential of as low as 290 mV at a current density of 10 mA cm^{-2} with a small Tafel slope of 60 mV/dec, which outperforms most noble metal-free electrocatalysts and even commercial IrO_2.

Without any surface functionalization or pretreatment, water-stable zeolitic imidazolate framework (ZIF-8) synthesized at room temperature are directly used as a highly efficient adsorbent for removal of copper ions from aqueous solutions. To experimentally unveil the adsorption mechanism of Cu^{2+} by ZIF-8, we explore various effects from a series of important factors, such as pH value, contact time, temperature and initial Cu^{2+} concentration. As a result, ZIF-8 nanocrystals demonstrate unexpected high adsorption capacity of Cu^{2+} and high removal efficiency for both high and low concentration of Cu^{2+} from water. Moreover, ZIF-8 nanocrystals possess fast kinetics for removing Cu^{2+} with the adsorption time of less than 30 min. In addition, the pH of solution ranging from 3 to 6 shows little effect on the adsorption of Cu^{2+} by ZIF-8. The adsorption mechanism is proposed for the first time and systematically verified by various characterization techniques, such as TEM, FTIR, XPS, XRD and SEM.

APPENDIX: PERMISSION TO USE COPYRIGHTED MATERIALS

1. Permission of Using Published Materials from Wiley (ChemSusChem):

JOHN WILEY AND SONS LICENSE TERMS AND CONDITIONS

Apr 04, 2018

This Agreement between Zhiqiang Xie ("You") and John Wiley and Sons ("John Wiley and Sons") consists of your license details and the terms and conditions provided by John Wiley and Sons and Copyright Clearance Center.

License Number	4322060045214
License date	Apr 04, 2018
Licensed Content Publisher	John Wiley and Sons
Licensed Content Publication	ChemSusChem
Licensed Content Title	Recent Progress in Metal–Organic Frameworks and Their Derived Nanostructures for Energy and Environmental Applications
Licensed Content Author	Zhiqiang Xie, Wangwang Xu, Xiaodan Cui, et al
Licensed Content Date	Mar 9, 2017
Licensed Content Volume	10
Licensed Content Issue	8
Licensed Content Pages	19
Type of use	Dissertation/Thesis
Requestor type	Author of this Wiley article
Format	Print and electronic
Portion	Text extract
Number of Pages	5
Will you be translating?	No
Title of your thesis / dissertation	NOVEL NANOSTRUCTURED MATERIALS DERIVED FROM METAL-ORGANIC FRAMEWORKS FOR ENERGY AND ENVIRONMENTAL APPLICATIONS
Expected completion date	May 2018
Expected size (number of pages)	1
Requestor Location	Zhiqiang Xie 1350 Bob Pettit Blvd Baton Rouge, LA BATON ROUGE, LA 70820 United States Attn: Zhiqiang Xie
Publisher Tax ID	EU826007151
Total	0.00 USD
Terms and Conditions	

2. Permission of Using Published Materials from American Chemical Society (ACS Applied Materials & Interfaces):

4/2/2018 Rightslink® by Copyright Clearance Center

Copyright Clearance Center RightsLink® Home Account Info Help

ACS Publications Most Trusted. Most Cited. Most Read.

Title: Hierarchical Sandwich-Like Structure of Ultrafine N-Rich Porous Carbon Nanospheres Grown on Graphene Sheets as Superior Lithium-Ion Battery Anodes

Author: Zhiqiang Xie, Ziyang He, Xuhui Feng, et al

Publication: Applied Materials

Publisher: American Chemical Society

Date: Apr 1, 2016

Copyright © 2016, American Chemical Society

Logged in as: Zhiqiang Xie Account #: 3001130159 LOGOUT

PERMISSION/LICENSE IS GRANTED FOR YOUR ORDER AT NO CHARGE

This type of permission/license, instead of the standard Terms & Conditions, is sent to you because no fee is being charged for your order. Please note the following:

- Permission is granted for your request in both print and electronic formats, and translations.
- If figures and/or tables were requested, they may be adapted or used in part.
- Please print this page for your records and send a copy of it to your publisher/graduate school.
- Appropriate credit for the requested material should be given as follows: "Reprinted (adapted) with permission from (COMPLETE REFERENCE CITATION). Copyright (YEAR) American Chemical Society." Insert appropriate information in place of the capitalized words.
- One-time permission is granted only for the use specified in your request. No additional uses are granted (such as derivative works or other editions). For any other uses, please submit a new request.

BACK CLOSE WINDOW

Copyright © 2018 Copyright Clearance Center, Inc. All Rights Reserved. Privacy statement. Terms and Conditions. Comments? We would like to hear from you. E-mail us at customercare@copyright.com

3. Permission of Using Published Materials from Elsevier (Electrochimica Acta):

Copyright Clearance Center RightsLink®

Home | Account Info | Help

Title: Facile Self-Assembly Route to Co3O4 Nanoparticles Confined into Single-Walled Carbon Nanotube Matrix for Highly Reversible Lithium Storage

Author: Zhiqiang Xie,Chengmin Jiang,Wangwang Xu,Xiaodan Cui,Carlos de los Reyes,Angel A. Martí,Ying Wang

Publication: Electrochimica Acta

Publisher: Elsevier

Date: 1 May 2017

Logged in as:
Zhiqiang Xie
Account #:
3001130159

LOGOUT

Please note that, as the author of this Elsevier article, you retain the right to include it in a thesis or dissertation, provided it is not published commercially. Permission is not required, but please ensure that you reference the journal as the original source. For more information on this and on your other retained rights, please visit: https://www.elsevier.com/about/our-business/policies/copyright#Author-rights

BACK CLOSE WINDOW

4. Permission of Using Published Materials from Elsevier (Electrochimica Acta):

5. Permission of Using Published Materials from Springer Nature (Ionics):

SPRINGER NATURE LICENSE
TERMS AND CONDITIONS

Apr 04, 2018

This Agreement between Zhiqiang Xie ("You") and Springer Nature ("Springer Nature") consists of your license details and the terms and conditions provided by Springer Nature and Copyright Clearance Center.

License Number	4322080045728
License date	Apr 04, 2018
Licensed Content Publisher	Springer Nature
Licensed Content Publication	Ionics
Licensed Content Title	Metal-organic framework-derived CoNi-embedded carbon nanocages as efficient electrocatalysts for oxygen evolution reaction
Licensed Content Author	Zhiqiang Xie, Ying Wang
Licensed Content Date	Jan 1, 2017
Type of Use	Thesis/Dissertation
Requestor type	non-commercial (non-profit)
Format	print and electronic
Portion	full article/chapter
Will you be translating?	no
Circulation/distribution	<501
Author of this Springer Nature content	yes
Title	NOVEL NANOSTRUCTURED MATERIALS DERIVED FROM METAL-ORGANIC FRAMEWORKS FOR ENERGY AND ENVIRONMENTAL APPLICATIONS
Instructor name	Prof. Ying Wang
Institution name	Louisiana State University
Expected presentation date	May 2018
Requestor Location	Zhiqiang Xie

6. Permission of Using Published Materials from Royal Society of Chemistry (Dalton Transactions):

Reproduced by permission of The Royal Society of Chemistry (RSC) for the following paper:
Y. J. Zhang, Z. Q. Xie, Z. Q. Wang, X. H. Feng, Y. Wang and A. G. Wu, " Unveiling the Adsorption Mechanism of Zeolitic Imidazolate Framework-8 with High Efficiency for Removal of Copper Ions from Aqueous Solutions", Dalton Trans., 2016, 45, 12653-12660. (Joint first author)
http://pubs.rsc.org/en/content/articlelanding/2016/dt/c6dt01827k#!divAbstract

CONTACTS-COPYRIGHT (Contracts-Copyright@rsc.org)
To Zhiqiang Xie (zxie5@lsu.edu)

Dear Zhiqiang Xie,

The Royal Society of Chemistry (RSC) hereby grants permission for the use of your paper(s) specified below in the printed and microfilm version of your thesis. You may also make available the PDF version of your paper(s) that the RSC sent to the corresponding author(s) of your paper(s) upon publication of the paper(s) in the following ways: in your thesis via any website that your university may have for the deposition of theses, via your university's Intranet or via your own personal website. We are however unable to grant you permission to include the PDF version of the paper(s) on its own in your institutional repository. The Royal Society of Chemistry is a signatory to the STM Guidelines on Permissions (available on request).

Please note that if the material specified below or any part of it appears with credit or acknowledgement to a third party then you must also secure permission from that third party before reproducing that material.

Please ensure that the thesis states the following:

Reproduced by permission of The Royal Society of Chemistry

and include a link to the paper on the Royal Society of Chemistry's website.

Please ensure that your co-authors are aware that you are including the paper in your thesis.

Best wishes,

Chloe Szebrat
Contracts and Copyright Executive
Royal Society of Chemistry
Thomas Graham House
Science Park, Milton Road
Cambridge, CB4 0WF, UK
Tel: +44 (0) 1223 438329
www.rsc.org

ZX

Zhiqiang Xie

Wed 4/4/2018 2:53 PM

To: contracts-copyright@rsc.org <Contracts-Copyright@rsc.org>

Reply all

To Whom it May Concern,

This is Zhiqiang Xie, a PhD student from Mechanical Engineering Department at Louisiana State University, and also the joint first author of the following paper published in *Dalton Transaction.*

Y. J. Zhang, Z. Q. Xie, Z. Q. Wang, X. H. Feng, Y. Wang and A. G. Wu, " Unveiling the Adsorption Mechansim of Zeolitic Imidazolate Framework-8 with High Efficiency for Removal of Copper Ions from Aqueous Solutions", Dalton Trans, 45, 12653-12660 (2016).

I would like to include the full article described above into my PhD dissertation as Chapter 5.

I would really appreciate it if I could receive the copyright permission before April 6, 2018. If you have any question or need any further information, please let me know soon.

Sincerely,

Zhiqiang (Andrew) Xie

VITA

Zhiqiang Xie was born and grew up in Yuncheng, Shanxi, China. He received his Bachelor's degree in materials science and engineering from Kunming University of Science and Technology in China in 2011 and Master's degree in materials engineering from the University of Dayton in 2013. He joined in the doctoral program in the Department of Mechanical and Industrial Engineering at Louisiana State University in 2014. His doctoral research focuses on the synthesis of various nanostructured electrode materials for rechargeable lithium-ion batteries, solar cells, and environmental cleaning.

Zhiqiang Xie's professional publications at LSU are listed as follows:

1. Z. Q. Xie, W. W. Xu, X. D. Cui and Y. Wang,"Recent Progress in Metal-Organic Frameworks and Their Derived Nanostructures for Energy and Environmental Applications", ChemSusChem, 2017, 10, 1645-1663.
2. Z. Q. Xie, Y. Wang, "Metal-Organic Framework-Derived CoNi Embedded Carbon Nanocages as Efficient Electrocatalysts for Oxygen Evolution Reation", Ionics, 2017, 1-8.
3. Z. Q. Xie, X. D. Cui, W. W. Xu and Y. Wang, "Metal Organic Framework-derived CoNi@CNTs Embedded Carbon Nanocages as Counter Electrode for Efficient Dye-Sensitized Solar Cells", Electrochim. Acta, 2017, 229, 361-370.
4. Z. Q. Xie, C. M. Jiang, W. W. Xu, X. D. Cui, C. de los Reyes, A. A. Martí, Y. Wang, "Facile Self-Assembly Route to Co_3O_4 Nanoparticles Uniformly Confined into SWCNT Sheet for Highly Reversible Lithium Storage" Electrochim. Acta, 2017, 235, 613-622.
5. Z. Q. Xie, Z. Y. He, X. H. Feng, W. W. Xu, X. D. Cui, J. H. Zhang, C. Yan, M. A. Carreon, Z. Liu, Y. Wang, "Hierarchical Sandwich-like Structure of Ultrafine N-Rich Porous Carbon Nanospheres Grown on Graphene Sheets as Superior Lithium Ion Battery Anodes", ACS Appl. Mater. & Interfaces, 2016, 8, 10324-10333.
6. Z. Q. Xie, J. Q. Zhao, S. C. Ellis, W. W. Xu, D. Dye, Y. Wang, "A Novel Preparation of Core-shell Electrode Materials via Evaporation-Induced Self-Assembly of Nanoparticles for Advanced Li-Ion Batteries", Chem. Commun., 2015, 51, 15000-15003.
7. Z. Q. Xie, H. Eikhuemelo, J. Q. Zhao, C. Cain, W. W. Xu, Y. Wang, "Ni and Fe Dual-Doped Li4Mn5O12 Spinels as Cathode Materials for High-Voltage Li-Ion Batteries", J. Electrochem. Soc., 2015, 162, A1523- A1529.
8. Z. Q. Xie, J. Q. Zhao, Y. Wang, "One-Step Solvothermal Synthesis of Sn Nanoparticles Dispersed in Ternary Manganese-Nickel-Cobalt Carbonate as Superior Anode Materials for Lithium Ion Batteries", Electrochim. Acta, 2015, 174, 1023-1029.
9. Y. J. Zhang, Z. Q. Xie,1 Z. Q. Wang, X. H. Feng, A. G. Wu and Y. Wang, "Unveiling the adsorption mechanism of zeolitic imidazolate framework-8 with high removal efficiency on copper ions from aqueous solutions", Dalton Trans., 2016, 45, 12653-12660. (Joint first author, highlighted in Back Cover).